

ABSTRACT

LI, CHENGJUN. Development of Microelectromechanical Systems for Advanced Nanomechanical Characterization. (Under the direction of Dr. Yong Zhu).

In the past decades, a lot of nanomaterials, such as nanowires and nanotubes, have been synthesized. These nanomaterials are important building blocks of nanotechnology and have been used in different kinds of applications, such as flexible and stretchable electronics, energy harvesting and storage, nanoelectromechanical systems (NEMS), etc. Mechanical properties of these nanomaterials need to be characterized and examined accurately since they are directly related to the reliability of these applications. Different methods have been used to conduct the mechanical characterization of nanomaterials, among which characterization using devices based on microelectromechanical systems (MEMS) have been proved to be a reliable way. Different kinds of MEMS-based devices have been designed, fabricated and calibrated which are able to measure a broad spectrum of mechanical properties of nanomaterial. However, there is still a plenty of room for improvement of MEMS-based devices or platforms. In this thesis, we make several improvements by designing new MEMS-based devices for advanced nanomaterial characterization.

The thesis starts with a review of background. In this review, the concept of MEMS and its development and prospects are briefly going through. Several classic MEMS fabrication processes are then introduced. The main focus of the review is the recent development of nanomechanical characterization of nanomaterials using MEMS where a series of MEMS-based devices and platforms are introduced, their design, function, performance and characterization results are explained with details.

With these current devices and platforms being introduced, several necessary improvements to achieve advanced nanomechanical characterization are identified. In the

following chapter, we make an improvement by fabricating a MEMS-based device which can be used to carry out displacement and force controlled nanomechanical tensile experiments. The device working principle is explained, actuator and sensors are calibrated. With the implementation of a PID controller, a feedback loop was constructed, and both force and displacement control are achieved.

The high strain rate testing capability of this device was also investigated. Frequency response and dynamic behavior of the device under ramping actuation was experimentally studied which has a good agreement with analytical analysis. It was identified that device itself can achieve very high strain rate up to 200 s^{-1} , but the low response speed of the displacement sensor's capacitive readout limits its high strain rate testing capability. However, with the current readout, we are still able to push forward the maximum strain rate for nanomechanical testing to 10 s^{-1} .

To compensate the relative low sensing speed of the capacitive sensor, we designed and fabricated a piezoresistive displacement sensor. Attributes to the piezoresistive sensing mechanism, the sensor have a fast response time which is able to measure strain rate up to 750 s^{-1} . A weak point of this sensor is the displacement resolution is low comparing with capacitive sensor. The resolution can be potentially improved by reducing the noise of the system.

© Copyright 2019 by Chengjun Li

All Rights Reserved

Development of Microelectromechanical Systems for Advanced Nanomechanical
Characterization

by
Chengjun Li

A dissertation submitted to the Graduate Faculty of
North Carolina State University
in partial fulfillment of the
requirements for the degree of
Doctor of Philosophy

Mechanical Engineering

Raleigh, North Carolina
2019

APPROVED BY:

Dr. Yong Zhu
Committee Chair

Dr. Xiaoning Jiang

Dr. Fen Wu

Dr. Jingyan Dong

DEDICATION

To my mom, for all her effort to bring me up.

BIOGRAPHY

Chengjun Li was born in Shenyang, a city in the northeast of China. He received his B.S. degree in Chemical Engineering in 2013 from Tianjin University, China. In August 2013, he joined North Carolina State University and has been working under Dr. Yong Zhu's advisory since then.

ACKNOWLEDGMENTS

I would like to sincerely thank my advisor Dr. Yong Zhu, not only for his insightful guidance on my research work and the financial support he gives me, but also for the words he said to me in his office when I was about to give up, for the patience he shows on me and for the lessons of life I learnt from him. Responsibility, calm down and find a solution when meet with difficulties, be a reasonable person, these lessons will help me to be a better person stepping into next stage of my life.

I also want to thank all the members in Dr. Zhu's group, Tao, Guangming, Qijin, Alper, Shanshan, Jimi, Jianxun, Zheng, Felipe, Qingquan, Weixin, Hongyu, Shuang, Yuxuan, and all the visitors Prof. Zhang, Prof. Yang, Prof. Shao, the time we spent together will be a precious memory in my life.

Finally, I want to thank Prof. Xiaoning Jiang, Prof. Fen Wu and Prof. Jingyan Dong for kindly serving as my committee members and for your valuable comments and suggestions.

TABLE OF CONTENTS

LIST OF FIGURES	vii
Chapter 1: Introduction	1
1.1. Microelectromechanical systems	1
1.2. MEMS fabrication	3
1.2.1. Bulk micromachining	4
1.2.2. Surface micromachining	7
1.2.3. LIGA	9
1.3. MEMS devices for nanomechanical characterization.....	10
1.3.1. Actuators	11
1.3.2. Sensors	15
1.3.3. Integrated tensile testing platforms	19
1.4. Recent results from nanomechanical testing.....	28
Chapter 2: A MEMS-based platform for displacement and force controlled nanomechanical tensile testing	31
2.1. Introduction.....	31
2.2. Device overview	33
2.2.1. Comb-drive actuator	34
2.2.2. Displacement sensor	35
2.2.3. Load cell.....	36
2.3. Results and discussion	37
2.3.1. Calibration of actuator	37
2.3.2. Calibration of displacement sensor	38
2.3.3. Implementation of feedback control	41
2.3.4. Mechanical demonstration	44
2.4. Conclusions and future developments	48
Chapter 3: An on-chip nanomechanical testing device: dynamic response and application for high strain-rate testing	50
3.1. Introduction.....	50
3.2. Device description	51
3.3. Modeling.....	52
3.3.1. Frequency response: vacuum and air.....	53
3.3.2. Dynamic response under ramping actuation force: vacuum and air.....	56
3.4. Experiment.....	58
3.4.1. Displacement measurements.....	58
3.4.2. Frequency response.....	61
3.4.3. Dynamic response under ramping actuation force: vacuum and air.....	63
3.5. Discussion	67
3.5.1. Damping coefficients	67
3.5.2. Strain rate	68
3.5.3. Force measurement	70
3.6. High strain rate testing of gold nanowires	71
3.7. Conclusions.....	73

Chapter 4: A piezoresistive displacement sensor for high frequency sensing in nanomechanical tensile testing applications	74
4.1. Introduction	74
4.2. Device description	75
4.3. Displacement sensor characterization	77
4.3.1. Static calibration	77
4.3.2. Dynamic characterization	81
4.3.3. Sensor resolution	84
4.4. Conclusion	91
References	92

LIST OF FIGURES

<i>Figure 1.1</i>	(a) The legs of a spider mite standing on gears from a micro-engine. (b) A torsional ratcheting actuator.....	2
<i>Figure 1.2</i>	Widespread fields of MEMS applications.....	3
<i>Figure 1.3</i>	Illustration of possible bulk-micromachined structures. (a) and (b) Rounded, isotropically etched pits in a silicon substrate with and without agitation. (c) and (d) Pyramidal pits etched into (100) and (110) silicon using anisotropic wet etchants bounded by (111) crystal planes	5
<i>Figure 1.4</i>	Bosch process: (a) sidewall passivation using C_4F_8 gas, (b) silicon isotropic etching using SF_6 gas, (c) SEM image of the deep trench etched by DRIE, (d) magnified SEM image of the sidewall with nanoscallops of the silicon microstructure	7
<i>Figure 1.5</i>	Two-mask fabrication process of polysilicon cantilevers	8
<i>Figure 1.6</i>	SEM image of (a) V-shaped electrothermal actuator (b) Z-shaped electrothermal actuator.....	12
<i>Figure 1.7</i>	Electrostatic actuators - (a) parallel plate; (b) comb drive. Indicated are the direction of displacement (x) and the capacitive spacing (h)	14
<i>Figure 1.8</i>	Inchworm schematic with signals applied to achieve motion to the right. The plate electrode is segmented by grounded standoffs that prevent electrical shorting of the plate to the plate electrode and establish amplitude A	15
<i>Figure 1.9</i>	(a) Schematic diagram of the thermal position sensor. (b) Illustration of our thermal displacement sensing concept. (c) Optical micrograph of free-standing thermal position sensors.....	18
<i>Figure 1.10</i>	(a) SEM micrograph of the PTP device, with a higher magnification image (b) of the reusable gap across which different fibers can be mounted ⁵³ . (c) PTP device developed by Lu.....	20
<i>Figure 1.11</i>	(a) Application of the test platform for nanofiber testing. (b) DIC contour plots of rigid body displacements monitored during tension. Each region has a solid color due to its rigid body motion.....	21
<i>Figure 1.12</i>	(a) SEM micrograph of the micromechanical device, the scale bar is 300 μm . (b) Jig used to apply displacement loads on the tensile testing device chip	22
<i>Figure 1.13</i>	(a) In situ tensile testing device including thermal actuator, load sensor, and specimen (b) device including comb drive actuator, load sensor, and specimen	23

<i>Figure 1.14</i> (a) SEM image of the developed on-chip tensile testing systems.55 (b) SEM image of a MEMS wirebonded device which can electronically measure force and displacement independently	24
<i>Figure 1.15</i> (a) SEM micrograph of the fabricated device. Scale bar 200 μm (b) Schematic of the closed-loop scheme implemented in the device for feedback control of the displacement sensor. Signals are in italics	25
<i>Figure 1.16</i> SEM images of the micromachined nanopositioner.....	26
<i>Figure 1.17</i> (a) SEM of thermomechanical testing platform developed by Chang. (b) Overall view of the SiC stage. (c) Experimental setup for in situ uniaxial tests. (d)(e) A sample before and after assembly with the stage.....	27
<i>Figure 1.18</i> (a) SEM image showing an overview of the device. Scale bar: 200 μm . The dashed square is detailed in (b). (c) Top-view schematic of the device operation for four-point measurements. (d) Cross-section of the device.....	28
<i>Figure 2.1</i> (a) SEM micrograph of the fabricated device. (b) Schematic of MEMS device configuration. (c) Device lumped mechanical model	33
<i>Figure 2.2</i> (a) Schematic of one unit of differential capacitive sensor. (b). Estimation of linear region of the capacitive sensor.....	36
<i>Figure 2.3</i> (a) Dimensions in a o-shaped load cell. (b) Deformed load cell under tension	37
<i>Figure 2.4</i> Comb-drive actuator calibration results. (a) Specimen gap when actuation voltage is 0V. (b) Specimen gap when actuation voltage is 14V. Scale bar is 1 μm . (c) Analytical and experimental relationship between actuation voltage and displacement.....	38
<i>Figure 2.5</i> (a) Functional block diagram of capacitive readout AT1006 and its connection with MEMS device. (b) Image of the MEMS device and capacitive readout	40
<i>Figure 2.6</i> Comparison of theoretical and experimental relationship between capacitance change and displacement for both displacement sensors.....	41
<i>Figure 2.7</i> Closed-loop block diagram for achieve (a) displacement control. (b) force control	42
<i>Figure 2.8</i> Step response of the feedback close-loop scheme.....	43
<i>Figure 2.9</i> Steps for mounting a nanowire on device (a) choose a nanowire from substrate (b) pick up the nanowire with a manipulator. (c) mount the nanowire on device with Pt-deposition (d) Displacement setpoint (line) versus measured displacement (dots)	44

<i>Figure 2.10</i> Stress relaxation of penta-twinned Ag nanowire. (a) Stress vs Strain. (b) Strain vs Time. (c) Stress vs Time	45
<i>Figure 2.11</i> Displacement-controlled stretching an Au nanowire until fracture. (a) Stress-strain curve. Insert is fracture surface, scale bar is 150nm. (b) Strain vs Time. (c) Stress vs Time	46
<i>Figure 2.12</i> Creep of penta-twinned Ag nanowire. (a) Stress vs Strain. (b) Strain vs Time. (c) Stress vs Time.....	48
<i>Figure 3.1</i> Schematic of lumped mechanical model of the device under dynamic testing.....	52
<i>Figure 3.2</i> Bode magnitude plot of the device obtained from Eq. (3-6).....	55
<i>Figure 3.3</i> The mode shapes for the first two in-plane resonance	55
<i>Figure 3.4</i> Illustration of Sensor B displacement when device is actuated by a ramping force (a) in vacuum, (b) in air. For both cases, Sensor B displacement is the superposition of an ideal linear displacement (constant velocity and correspondingly constant strain rate) and deviation. Horizontal dashed line marks zero deviation.....	57
<i>Figure 3.5</i> Experiment setup (high speed camera and optical microscope) to measure the dynamic displacement of the device	58
<i>Figure 3.6</i> (a) One frame of high-speed image taken under microscope. Scale bar 30 μm . (b) 1D line intensity profile of the periodic patterns in region of interest before and after translation. (c) DFT of the line intensity profile before and after translation, upper is magnitude plot, lower is phase plot. Fundamental frequency corresponding to spatial frequency of periodic patterns is circled out. Phase shift of fundamental frequency is used to retrieve translational displacement.....	60
<i>Figure 3.7</i> (a) Optically measured displacement with frequency 2002 Hz, the frame rate used is 100 fps. (b) Relationship between actuation force frequency and normalized displacement amplitude measured using optical image processing method. The optical measurement result was fitted and damping coefficients in air were obtained.....	62
<i>Figure 3.8</i> Voltage applied to device to achieve ramping actuation force, loading time is 1s ..	63
<i>Figure 3.9</i> Comparison of displacement measured from AT1006 and model in vacuum when loading time is (a)1s, (b)5ms and (c) 1ms. Comparison of displacement from dynamic model and optically measured displacement in air when loading	

time is (d) 1 s, (e) 1 ms and (f) 0.1 ms. The frame rates are 50 fps, 16,000 fps, 95,000 fps, respectively. Insets are the corresponding images which were taken under same microscope magnification. Scale bars are 100 μm , 50 μm and 10 μm respectively. Higher frame rate is associated with low field of view 66

Figure 3.10 (a) Relationship of maximum strain rate the device can attain versus deviation ratio and travel range in vacuum. (b) Relationship of maximum strain rate vs deviation ratio and travel range in air 70

Figure 3.11 Stress-strain curves for two Au nanowires tested at different strain-rates 72

Figure 3.12 SEM images of the tested Au nanowires before and after testing. (a) 10/s. (b) 1×10^{-5} /s. Scale bar: 300 nm..... 73

Figure 4.1 (a) Optical image of the piezoresistive sensor and comb-drive actuator. (b) Electrical schematic of the wheatstone bridge constructed of the piezoresistor and three reference resistors 77

Figure 4.2 Calibrated relationship between (a) displacement vs actuation voltage (b) displacement vs actuation voltage square (c) output voltage vs actuation voltage (d) displacement vs output voltage 79

Figure 4.3 (a) Applied voltage to a single Z-shaped resistor and its resistance. (b) Relationship between output voltage V_G and resistance change ΔR calculated based on Eq. (4-1)..... 81

Figure 4.4 (a) Measured output voltage with frequency 100 Hz. (b) Relationship between normalized output voltage amplitude versus frequency, i.e. frequency response ... 83

Figure 4.5 Signal conditioning circuit to measure noise spectrum density of Wheatstone bridge..... 86

Figure 4.6 (a) Measure noise power spectrum density within range 0 to 2500 Hz. (b) Noise PSD from 0 to 100 Hz from which 1/f noise and Johnson noise can be clearly identified 88

Figure 4.7 (a) The relationship between actuation voltage and amplified output voltage of wheatstone bridge with different excitation voltages. (b) Calibrated relationship between displacement and amplified output voltage when the excitation voltage is 3V 89

Figure 4.8 (a) Sensor output under a ramping input with 0.1 ms loading time. (b) A closer look of output during the loading period 90

CHAPTER 1:

Introduction

1.1. Microelectromechanical Systems

Microelectromechanical Systems, abbreviated as MEMS, is the integration of microelectronics and micromachines, specifically it means micromachines with characterized dimension within the range from several microns to several millimeters that designed and fabricated on the basis of microelectronics technology. Hence MEMS technology can be seen as the extension and development of semiconductor integrated circuit technology. The types of MEMS devices can vary from relatively simple structures having no moving elements, to extremely complex electromechanical systems with integration of microactuators, microsensors, signal processing, interface circuits, control circuits, communication systems and powers, etc. In general, MEMS is an interdisciplinary technology which involves both technical disciplines such as microelectronics, machines, micromachining, system and control and fundamental disciplines such as physics, chemistry, material, mechanics and biology.

Comparing with traditional electrical and mechanical systems, MEMS has several distinct advantages. In the first place, MEMS devices are typically small, light-weight, and consume low power. Figure 1.1 presents two devices fabricated by Sandia National Laboratory showing the small size of these devices. Secondly, MEMS with its mass fabrication techniques enable hundreds or thousands of micro electromechanical devices can be fabricated simultaneously on a single silicon wafer by silicon micromachining process, which can greatly reduce the cost. Thirdly, multiple sensors or actuators with different sensitive directions and different functions can be

integrated on one chip forming micro-sensor arrays and micro-actuator arrays. Also, devices with different functions can be integrated to form a complex microsystem.

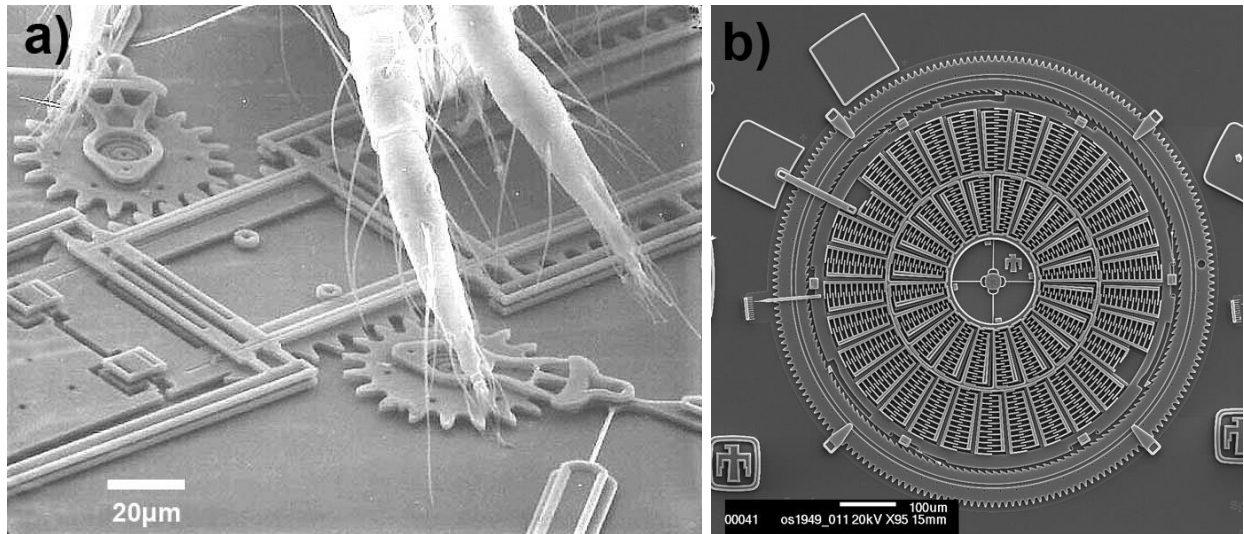


Figure 1.1. (a) The legs of a spider mite standing on gears from a micro-engine. (b) A torsional ratcheting actuator. [Courtesy Sandia National Laboratories, SUMMiT™ Technologies, www.sandia.gov/mstc]

It is these advantages that make MEMS an attractive research area since it was introduced. After several decades' development, MEMS has gradually made its way into everyday products. During which, several breakthrough progresses have been made. In the 1970s, micromechanical pressure sensor came out. In the late 1980s, electrostatic silicon micromotor was developed. In the late 1990s, inkjet print heads, hard disk read/write heads, and silicon accelerometers were successively produced in large scale. In the past 5 to 10 years, due to the promotion of smart phones, MEMS has been widely applied and rapidly developed. Figure 1.2 shows applications of MEMS in different fields today.

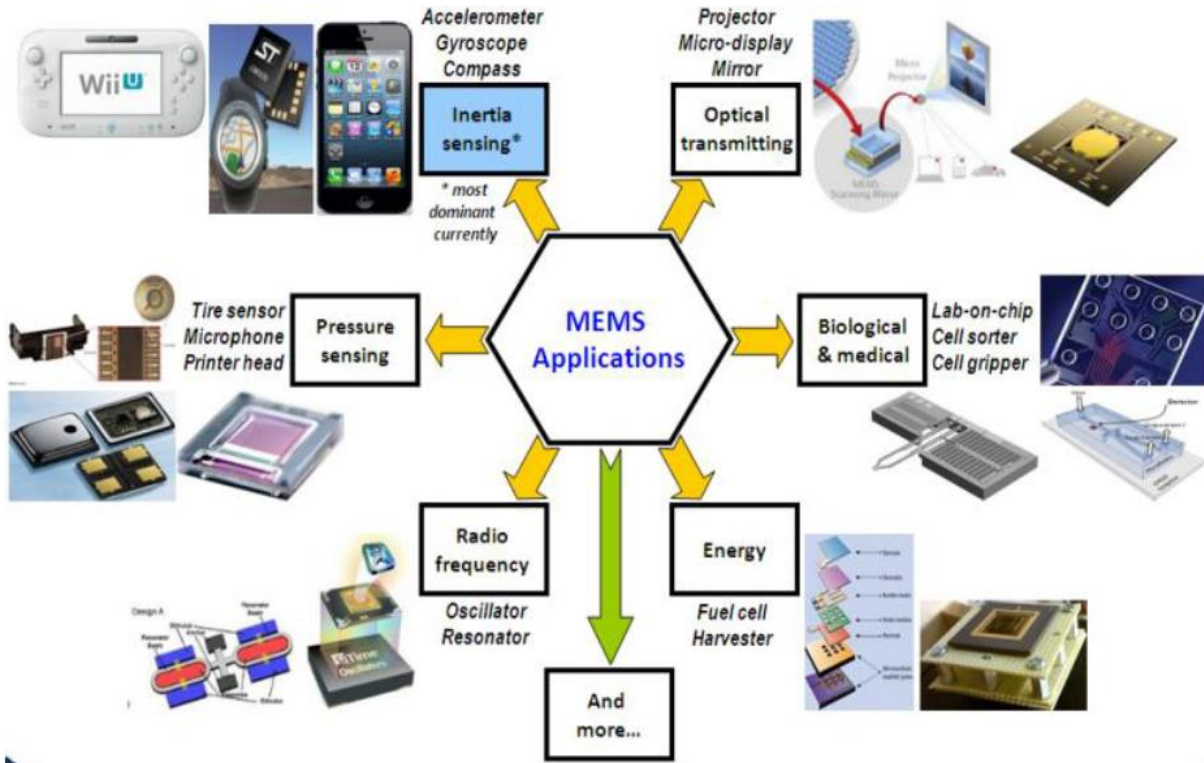


Figure 1.2. Widespread fields of MEMS applications¹.

Nowadays, MEMS has fully bloomed which stimulates the emergence of more and more MEMS-related researches spreading over a broad range of areas. Among them one important area is utilizing MEMS-based device to characterize mechanical properties of nanomaterials which is also the subject of this thesis. This research area involves three topics, i.e. fabrication of MEMS-based device, design of MEMS-based devices with capabilities of conducting different nanomechanical characterizations, nanomechanical characterization results. A brief review of these topics will be presented in the following sections in this chapter.

1.2. MEMS fabrication

Miniaturization is a prominent feature of MEMS devices. With the development of MEMS technology, some MEMS devices can be fabricated with characteristic dimensions within the sub-

micron range. Conventional machining techniques are not able to fabricate such tiny size devices which led to the development of a range of new fabrication techniques, namely micromachining techniques. Currently there are three micromachining techniques commonly used for MEMS fabrication in industry, i.e. bulk micromachining, surface micromachining and LIGA, each of which has its own advantages and limitations.

The main material used to in MEMS fabrication is silicon, including single crystal silicon and polysilicon. In addition to that, silicon dioxide, silicon nitride, silicon carbide, Germanium-based materials and some polymer materials can also be used as the material for MEMS. With the development of MEMS technology, more and more of these materials are being used for fabrication of devices with different functions.

1.2.1. Bulk micromachining

Bulk micromachining is the oldest micromachining technique. This technique involves selectively removing the substrate material to achieve miniaturization of the structures or patterns. Bulk micromachining can be achieved using chemical or physical means, where chemical means are widely used in the MEMS industry.

Chemical wet etching is a bulk micromachining technique widely used, it works by immersing a substrate in the solution of the reactive chemicals which etches the exposed regions with certain speed. Chemical wet etching can be either isotropic or anisotropic. Isotropic etching happens when an etchant has no selectivity of crystal planes or has the same etching rate for all the different crystal planes of the material. For example, for silicon, a mixture of hydrofluoric acid, nitric acid, and acetic acid (HNA) is the most common isotropic etchant solvent. Silicon nitride and Au can be used as the passivation layer in this case as HNA almost has no etching effect on

these materials. Thermally grown silicon dioxide can also be used as the passivation layer since HNA has a very slow etching rate against it comparing with silicon. Anisotropic etching happens when different crystal planes have different etching rate when in contact with an etchant. For silicon, commonly used anisotropic wet etching agents include alkaline solutions such as potassium hydroxide (KOH), and ethylenediamine pyrocatechol (EDP) and tetramethylammonium hydroxide (TMAH). The etching rate ratio of KOH on different crystal planes of silicon is $[110]:[100]:[111] = 600:400:1$, hence etching a (100) silicon wafer using KOH would result in a pyramid shaped etch pit as shown in Figure 1.3(c). The etched wall will be flat and angled. The angle to the surface of the wafer is 54.7° . Figure 1.3 shows the illustration of possible bulk-micromachined structures.

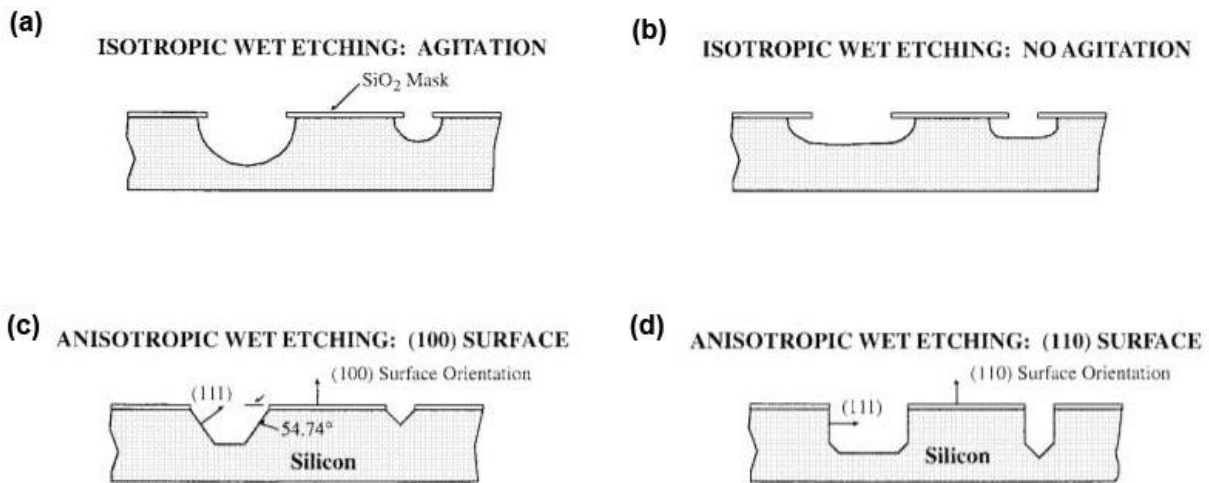


Figure 1.3. Illustration of possible bulk-micromachined structures. (a) and (b) Rounded, isotropically etched pits in a silicon substrate with and without agitation. (c) and (d) Pyramidal pits etched into (100) and (110) silicon using anisotropic wet etchants, bounded by (111) crystal planes².

Since chemical wet etching bulk micromachining offers very high etching speed and selectivity, and etching speed and selectivity can be changed by means like changing the reactive chemical, adjusting temperature of etching liquid, it has been used a lot in MEMS fabrication.

However, this kind of method has the disadvantage that it can't yield deep trenches with vertical profile. If directionality is very important for high-resolution pattern transfer, chemical wet etching is normally not used. Dry etching, in this case, can be used as a substitution.

In dry etching, particles instead of solution are used to remove the substrate material. Dry etching can be achieved through physical means or chemical means. Physical dry etching is realized with high kinetic energy particles beams (ion, electron, or photon) to bombard the substrate material knocking out the its atoms. When the high energy particles knock out the atoms from the substrate surface, the material evaporates after leaving the substrate. There is no chemical reaction taking place and therefore only the material that is unmasked will be removed. Chemical dry etching can also be used to selectively remove substrate material. Without using liquid chemicals or etchants, this method uses vaper phase etchant instead. The etching process relies on a chemical reaction between etchant gases to attack the material surface. For silicon, some of the ions that are used in chemical dry etching is tetrafluoromethane (CH_4), sulfur hexafluoride (SF_6), nitrogen trifluoride (NF_3), chlorine gas (Cl_2), or fluorine (F_2).

Another dry etching method is reactive ion etching (RIE) which uses both physical and chemical mechanisms to achieve high levels of resolution. In the RIE-process, positive ions are produced from reactive gases which are accelerated with high energy to the substrate and chemically react with the substrate. Since the process combines both physical and chemical interactions, the process is much faster. The typical RIE gasses for silicon are CF_4 , SF_6 and $\text{BCl}_2 + \text{Cl}_2$. The process is one of the most diverse and most widely used processes both in industry and research.

Deep Reactive Ion Etching (DRIE) is an improved RIE Deep which is used to etch deep cavities (or trenches) in substrates with relatively high aspect ratios (the ratio of a cavity's depth to

its width). These cavities can be hundreds of micrometers deep while only a few micrometers wide. Aspect ratios as high as 50:1 can be achieved with DRIE. Most systems utilize the so-called "Bosch process" or "switched etching process", in which a polymer is used to passivate the etching of the sidewalls. This passivation protects the sidewalls from being etched further but not the horizontal surfaces. During the entire etching process, the gas mixture switches back and forth between etchant gases and passivation gases. This results in a deep, narrow etch. Figure 1.4 (a) and (b) illustrate the Bosch process and SEM images of fabricated structure are shown in (c) and (d).

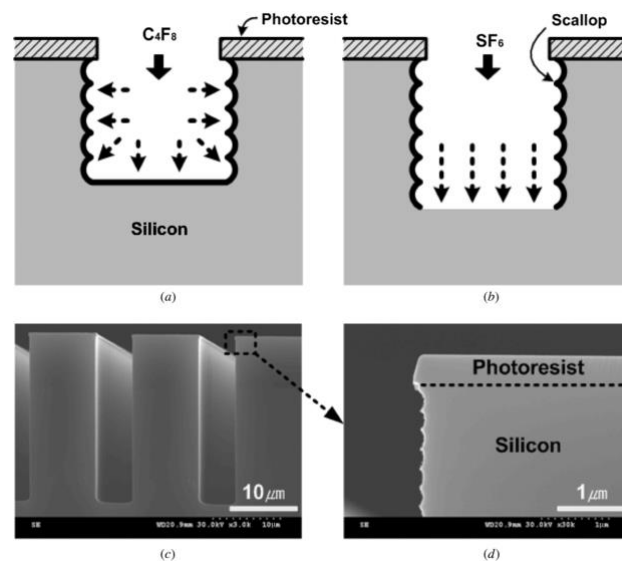


Figure 1.4. Bosch process: (a) sidewall passivation using C_4F_8 gas, (b) silicon isotropic etching using SF_6 gas, (c) SEM image of the deep trench etched by DRIE, (d) magnified SEM image of the sidewall with nanoscallops of the silicon microstructure³.

1.2.2. Surface micromachining

Surface micromachining is another commonly used technology for the fabrication of MEMS devices. Different from bulk micromachining which etches the substrate, surface micromachining etches away layers deposited on top of the silicon substrate, the silicon substrate is mainly used as a foundation on which to build. The process usually involves a sequence of steps:

Step 1: Deposition of some thin-film material as sacrificial layer.

Step 2: Patterning the sacrificial layer.

Step 3: Deposit and patterning another thin-film layer as structural layer.

Step 4: Liquid phase removal of sacrificial layer.

Step 5: Removal of liquid or drying.

A typical surface micromachined cantilever beam is shown in Figure 1.5. Here, a silicon dioxide layer is deposited and patterned. This oxide layer is temporary and is commonly referred to as the sacrificial layer. Subsequently, a thin film layer of polysilicon is deposited and patterned and this layer is the structural mechanical layer. Lastly, the temporary sacrificial layer is removed and the polysilicon layer is now free to move as a cantilever. Surface micromachining is useful for creating cantilever beams, bridges and sealed cavities. More complex structures, such as turbines, gear trains and micromotors can be formed by repeating this process, using multiple layers of polysilicon.

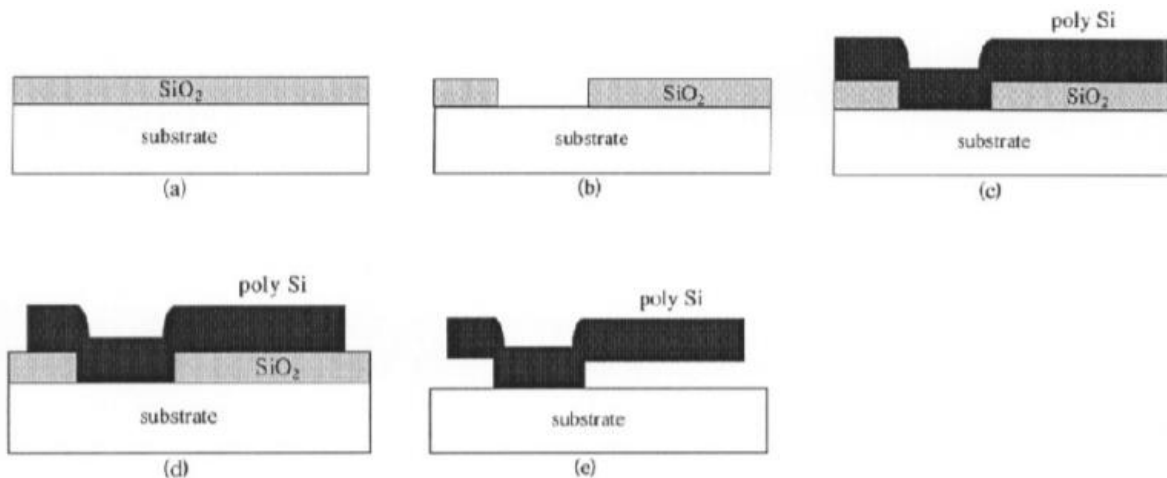


Figure 1.5. Two-mask fabrication process of polysilicon cantilevers⁴.

Surface micromachining, compared with bulk micromachining, has several advantages. For example, the vertical dimension of a structure fabricated with this process is more precisely

controlled. This is because the thickness of sacrificial layer and structural layer are accurately controlled since they are defined by thin film deposition. And this process is cost effective on the way that the expensive silicon wafer can be replaced with cheaper substrate such as glass and plastic. More importantly, using this process, monolithic microsystems in which the electronic and the mechanical components can be built in on the same substrate. The disadvantage of this process is that residual stress will usually remain in the structural layer and the released structure has the tendency to bend upward or downward. High temperature annealing is needed to reduce residual stress in the structural layer. Besides, stiction can be a problem for successfully fabricating MEMS device using this process. Stiction refers to the sticking of structural elements either to the substrate or the adjacent elements. Capillary forces from rinsing liquids, as well as electrostatic and van der Waals forces can be the sources of stiction force which produce permanent adhesion.

1.2.3. LIGA

Another important micromachining technique is LIGA, which is a German acronym for Lithographie (Lithography), Galvanoformung (Electroplating), Abformung (Molding). This technique was developed in Germany in the early 1980s and is dedicated for fabrication of high-aspect-ratio structures. The process starts with casting an x-ray radiation sensitive PMMA onto a suitable substrate. Then PMMA is selectively exposed to x-ray through a lithographic mask. The exposed areas are chemically dissolved, since the x-ray can penetrate quite deep into the PMMA, up to 1mm, this step can generate a high-aspect-ratio cavity pit with smooth and nearly perfect sidewalls. The pit or the open area of the PMMA is then filled with metal using electroplate. The rest PMMA is removed afterward leaving the finely defined high-aspect-ratio microstructure.

LIGA has the advantages that it can fabricate microstructures with arbitrary cross sections with a wide range of sizes and high-aspect-ratio, it allows material other than silicon to be used, it has better precision and low surface roughness, etc. The main disadvantage of LIGA is that the cost of this process is relatively expensive due to the demand of special masks and the x-ray synchrotron radiation source.

1.3. MEMS devices for nanomechanical characterization

As the development of nanotechnology, more and more nanomaterials have been used in different kinds of applications, such as flexible and stretchable electronics⁵⁻⁸, energy harvesting and storage^{9, 10}, nanoelectromechanical systems (NEMS)^{11, 12} etc. Mechanical properties of these nanomaterials need to be characterized and examined accurately since they can be used to evaluate reliability of these applications. Different kinds of methods have been used to carry out the mechanical characterization of nanomaterials, for example, vibration and resonance are commonly used to measure the Young' s modulus of one dimensional nanomaterials¹³⁻¹⁶, atomic force microscopes (AFM) have been used to bend the nanomaterials from which a spectrum of mechanical properties can be obtained^{17, 18} or contact the nanomaterials from which mechanical properties like indentation modulus and radial elastic modulus can be obtained^{19, 20}. nanomanipulators have been used to conduct tensile test²¹⁻²⁴ and buckling test^{23, 25}. Indentation tests have been carried out using nanoindenters^{26, 27}. Among all these methods, nanomechanical characterization using MEMS-based devices shows some advantages. For example, MEMS-based device can integrate actuator and sensor together excluding the usage of external actuator or sensor which provides more possibility for nanomechanical characterization. Different kinds of MEMS actuators can be used to provide force suitable for different applications. MEMS sensors can

achieve nanometer or even sub-nanometer displacement resolution and nanonewton force resolution. Besides, the size of MEMS chips is usually very small so that these chips can be placed inside SEM or TEM to carry out in-situ nanomechanical testing which offers the capability of studying the relationship between mechanical properties and microstructures of nanomaterials.

In this section, we will summarize a few classic and recent designs of MEMS-based devices used for nanomechanical testing. We will start with introduction of MEMS actuators and then MEMS sensors, in the end we will talk about integrated MEMS-based tensile testing platforms.

1.3.1. Actuators

Actuators for nanomechanical testing can be internal (on-chip) or external. External actuators have many different working mechanisms, the widely used one in MEMS tensile testing is piezoelectric actuator. For on-chip actuators, two most commonly used are electrothermal actuator and electrostatic actuator.

Electrothermal actuator works based on the thermal expansion of beams caused by Joule heating. A typical configuration of this kind of actuator is shown in Figure 1.6(a), it consists of a shuttle in the middle, symmetrical parallel inclined beams are connected to the shuttle. The far ends of the beams are anchored. When a potential difference is applied across the anchors, current passes through the beams generating heat and causing expansion of the beams which actuates the shuttle to move towards the inclined direction. The force generated depends on several factors, such as the voltage applied, the number of beams, the inclined angle, etc. Corigliano²⁸ has done a parametric studies using both analytical computation and multi-physics simulation to optimize the device response in terms of these factors. In general, the V-shape thermal actuator can transmit large loads on the order of tens or hundreds of millinewtons to the specimen under a relatively

small actuation voltage. However, the displacement transmitted by thermal actuator is relatively small, up to several microns, this is due to the large stiffness of the inclined beams. With this into consideration, a z-shaped thermal actuator was developed²⁹ as shown in Figure 1.6(b), which has smaller stiffness and can produce larger displacement. Another method to increase the travel range of thermal actuator is to use a cascaded structure which is able to provide tens of microns displacement³⁰.

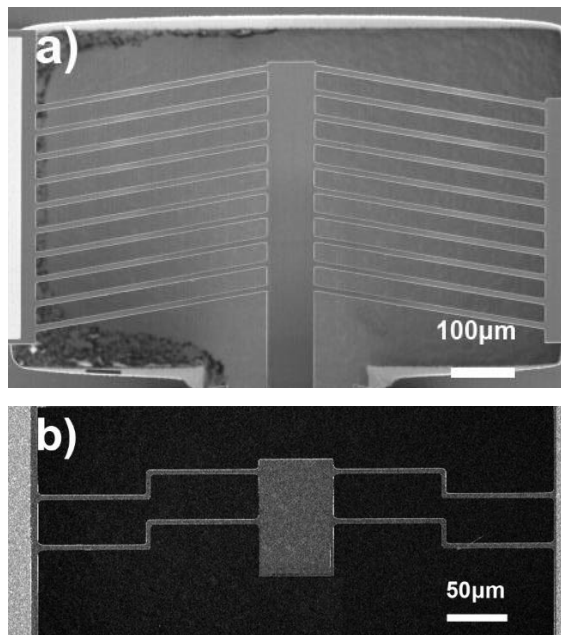


Figure 1.6. SEM image of (a) V-shaped electrothermal actuator (b) Z-shaped electrothermal actuator.

A critical problem with electrothermal actuator is heat generated by the actuator will transfer to specimen area heating up the specimen, which prevents its application on testing nanomaterials whose properties are sensitive to temperature such as silicon. This heating issue is unavoidable for electrothermal actuators, however it can be minimized to an acceptable range. A heat sink structure can be introduced to dissipate heat and hence decrease the temperature rise at the specimen region to below 5 °C³¹. Qin³² experimentally verified the effect of heat sink through

comparison of electrothermal actuator with and without heat sink in air. The more heat sink beams used the less temperature increase at the specimen area. However, increasing number of heat sink beams means increasing the stiffness of the actuator, hence it is a trade-off between reducing temperature and reducing stiffness.

Electrostatic actuator is another commonly used MEMS actuator. The actuation force comes from the electrostatic attraction force between two parallel plates when they are oppositely charged. Parallel plates actuator and comb-drive actuator are two kinds of electrostatic actuator where the latter is widely used. Figure 1.7 illustrate the configurations of these two actuators. Different from parallel plates actuator where the gap between moving and fixed plates decreases when the actuator works, the gap between moving and fixed combs doesn't change for comb-drive actuator since the actuator moves along the axis of comb-drives. Comparing with thermal actuator, electrostatic comb-drive actuator has the advantage that it has larger travel range (up to tens of microns), besides there is no heating effect to be worried. In addition, the generated force has a linear relationship with square of actuation voltage regardless of travel range which is feature good for calibration of the actuator. The disadvantage of electrostatic actuator is that the force generated by one pair of comb-drive is small, hence in order to provide large force (up to several millinewtons), thousands of comb-drives and a large actuation voltage are used which unavoidably increases the size of the actuator. One potential issue for electrostatic actuator is the pull-in phenomenon which happens when the actuator voltage is too large, hence electrostatic actuator must be operated within a safety actuation voltage range.

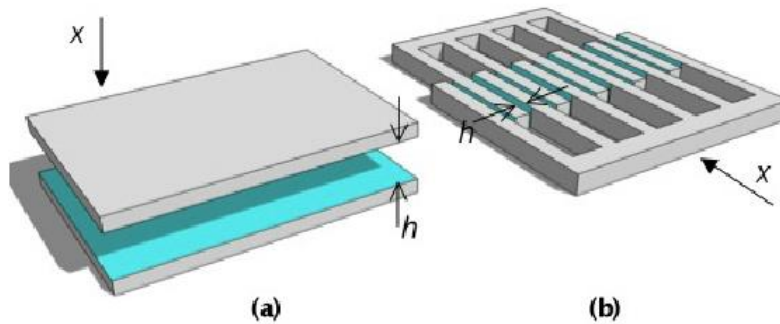


Figure 1.7. Electrostatic actuators - (a) parallel plate; (b) comb drive. Indicated are the direction of displacement (x) and the capacitive spacing (h).

Another kind of actuator is inchworm actuator which utilizes the out-of-plane electrostatic force between parallel plates and converts it to in-plane motion. An illustration of the actuator's configuration and working principle is shown in Figure 1.8. The device makes one step to the right through the following sequence: (a) the leading clamp is pulled electrostatically toward the substrate and held in place, (b) the plate electrode is actuated and bent downwards to pull the trailing clamp to the right, (c) the trailing electrode is actuated electrostatically and kept stationary, (d) the plate electrode and leading clamp are released. Unloading of the electrode pushes the clamp forward (to the right). The advantage of this kind of actuator is it can provide a large displacement without undermining the force provided.

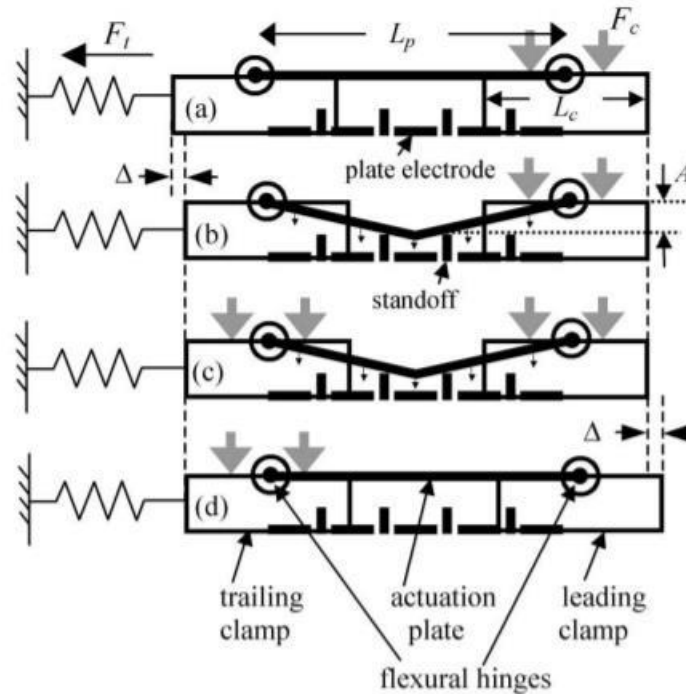


Figure 1.8. Inchworm schematic with signals applied to achieve motion to the right. The plate electrode is segmented by grounded standoffs that prevent electrical shorting of the plate to the plate electrode and establish amplitude A ³³.

1.3.2. sensors

Both force and displacement sensors are needed for mechanical characterization of nanomaterials. For macro mechanical tensile testing, usually an external pre-calibrated load cell is placed in the force “train” which can convert the force in the specimen into electrical signal that can be detected through different mechanisms. However, this is not practical for microscale mechanical tensile testing. Hence for characterization of nanomaterials, load sensor is usually fabricated on chip together with the whole test platform.

The most common mechanism for load detection of on chip MEMS load sensor is calculating load force based on the deformation of a compliant structure (usually some supporting

beams). The compliant structure is connected to the specimen forming a series force “train” thus they sustain the same amount of force. If the stiffness of the compliant structure is known, the force can be obtained by measuring the deformation or displacement of the compliant structure. From this perspective, the load sensor essentially is a displacement sensor. The stiffness of the compliant structure can be calibrated using AFM³⁴, nanoindentation³⁵, microfabricated calibrators³⁶, Lorentz force³⁷, or by a weighing scale³⁸.

Displacement sensing mechanisms commonly used in nanomechanical characterization include extracting displacement from high-resolution images, capacitive sensing, thermal sensing, piezoresistive sensing.

Due to the extremely small size of specimen, nanomechanical tests are normally performed under inside scanning electron microscope (SEM) or transmission electron microscope (TEM) or under a high-magnification optical microscope. For in situ SEM or TEM testing, displacement can be directly measured from high resolution SEM or TEM images focusing on the sample area or a specialized gauge area taken during the experiment³⁹⁻⁴¹. For optical images, some image processing algorithms can be used to assist the analysis of displacement. The most commonly used one is digital image correlation (DIC)^{34, 42, 43}.

Capacitive sensors are widely used in MEMS industry along with commercially available chips for data acquisition. These sensors convert displacement induced capacitance change into voltage signals, their advantages include high sensitivity, low temperature drift, low power dissipation and process compatibility with other functional structures. Beside they can continuously monitor displacement in real time comparing with the imaging method. Usually a differential scheme is used for capacitance measurement⁴⁴⁻⁴⁶, because on one side it can improve the linearity and sensitivity of the sensor, on the other side, due to the existence of parasitic

capacitances and stray capacitances, the measured absolute capacitance will not reflect the real displacement. MEMS differential capacitive sensor has been proved to be a reliable and mature sensor based on which Analog Device developed an accelerometer and introduced it into the market in 1994⁴⁷. These differential capacitive sensors need specialized readout to acquire the signal. A commercially available sensing module (MS3110, MicroSensors) is commonly used in academic research^{48, 49}. The MEMS package is suggested to be placed as close as possible to the sensing module in order to diminish stray capacitance and electromagnetic interference.

Thermal sensing is another kind of sensing mechanism which can be used to measure displacement. This sensing mechanism relies on the resistance change caused by temperature change. An example of such a sensor is shown in Figure 1.9. The sensing element is a resistive heater made from moderately doped silicon and supported by legs made from highly doped silicon that act as electrical leads. Application of a voltage across the legs of the device results in a current flowing through the heater and a subsequent increase in the device temperature as shown in Figure 1.9(a). To use this device as a displacement sensor, it needs to be positioned directly above an edge or step on the object of interest, as shown in Figure 1.9 (b), when the object is moving to left, the overlap area between the heated resistor and object is enlarged which results in more heat dissipation through air to the object, hence the sensor's resistance changes which can be measured to induce the displacement change. Usually a differential configuration is utilized to increase the linearity as shown in Figure 1.9(c).

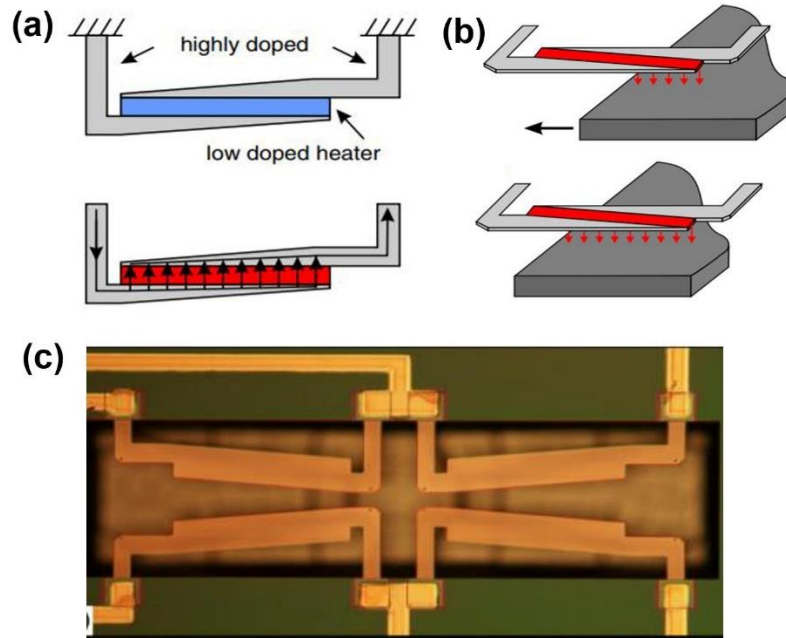


Figure 1.9. (a) Schematic diagram of the thermal position sensor. (b) Illustration of our thermal displacement sensing concept. (c) Optical micrograph of free-standing thermal position sensors⁵⁰.

Piezoresistive sensors are designed based on the piezoresistive effect where electrical resistivity changes when mechanical strain is applied. This effect was first found to happen in metal material. Later silicon was found to have a large piezoresistive effect with high piezoresistive coefficient (the ratio between relative resistance change and strain). MEMS-based piezoresistive sensors have commonly been used to serve as pressure sensor or tactile sensor or force sensor with a cantilever scheme, but not too much as displacement sensor that can be used in nanomechanical tensile testing. Z-shaped thermal actuator has been used to serve as a piezoresistive sensor at the same time⁵¹.

1.3.3. Integrated MEMS tensile testing platform

In this section, we will present the current development of MEMS-based platform that can be used to carry out tensile testing of nanomaterials. Several representative configurations will be introduced.

Push-to-pull (PTP) devices have been used to serve as a tensile testing platform for nanoscale material. This kind of device is purely a microfabricated structure which can convert a compressive force (push) to a tensile force (pull) on a specimen. Figure 1.10 (a) shows a commercially available PTP device developed by Hysitron^{52, 53}. An external conductive diamond flat punch indenter is used to provide the compressive force from top. Displacement or elongation of a specimen is measured from the capacitive displacement sensor embedded in the external indenter. The raw force measured from the load sensor in the indenter is taken to be the force applied to the combination of the sample and the PTP device. On the premise of known stiffness and measured displacement of PTP device, force applied to the sample can be determined by subtracting the contribution of the PTP device from the raw force data. Several different configurations have been designed to achieve the same push-to-pull function. Figure 1.10(c) shows a PTP device developed by Lu⁵⁴ where the downward compressive force is converted to the horizontal tensile force.

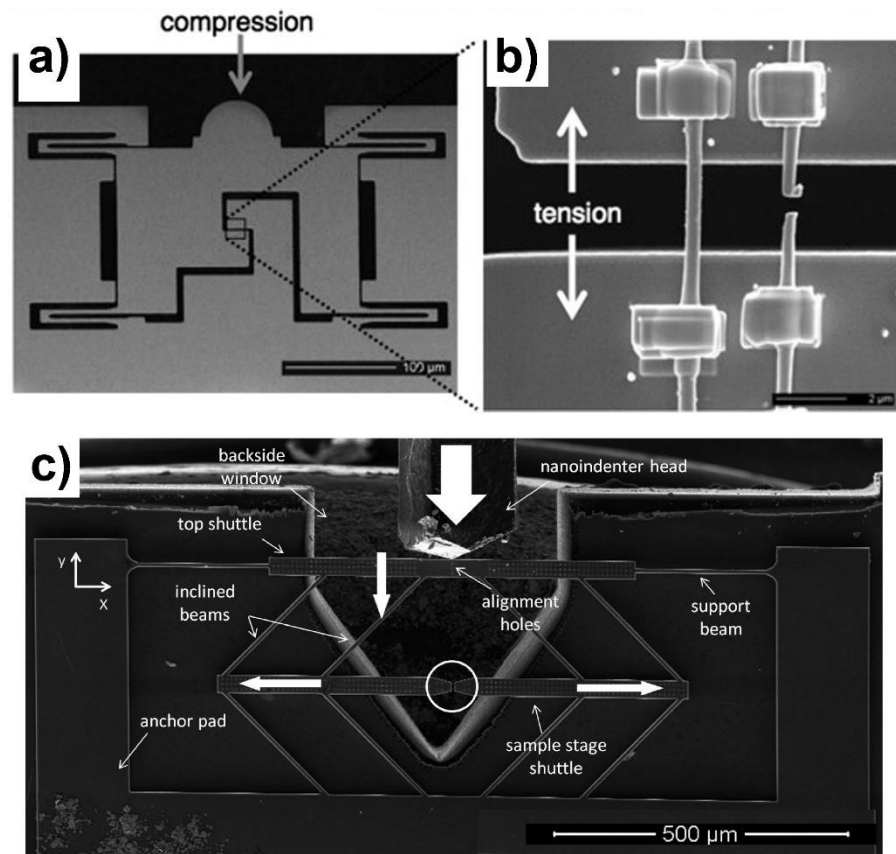


Figure 1.10. (a) SEM micrograph of the PTP device, with a higher magnification image (b) of the reusable gap across which different fibers can be mounted⁵³. (c) PTP device developed by Lu⁵².

Another kind of testing platform, which is similar to PTP device in terms of using an external actuator, includes an on-chip load cell. The platform is developed by Naraghi³⁴ as shown in Figure.1.11. Nanomaterial is placed between a load cell and a stationary grip. The on-chip load cell is a pair of simple compliant beams whose stiffness can be tuned by adjusting the position of deposited Pt blocks. The stationary grip is glued to a tipless AFM cantilever which holds still during experiment. An external piezoelectric actuator is used to move the device substrate to apply tensile force to the specimen. DIC is used to measure the elongation of the specimen and deformation of the load sensor as shown in Figure xx where rigid body motions of three parts of

the device were monitored (region 1 is the substrate, region 2 is the freestanding load sensor and region 3 is the stationary grip).

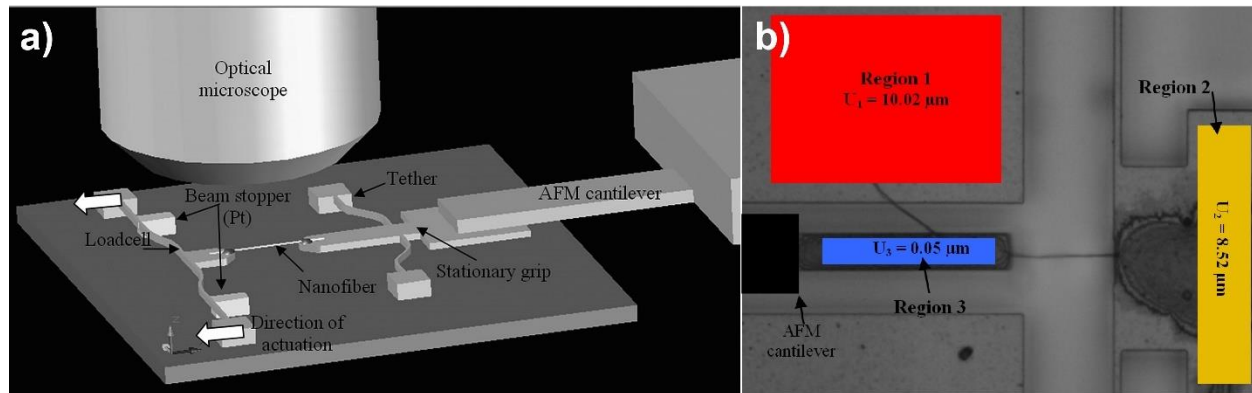


Figure 1.11. (a) Application of the test platform for nanofiber testing. (b) DIC contour plots of rigid body displacements monitored during tension. Each region has a solid color due to its rigid body motion.³⁴

Samuel⁴¹ made several improvements to the above design to achieve in situ nanomechanical testing. His design is shown in Figure 1.12. Specimen gap D is placed between structure A which is a pushing head and structure C which is a load cell. A is to be connected to an external actuator and structure B is used to constrain the movement to be in the horizontal direction. Microfabricated gaps E (between A and substrate) and F (between C and substrate) can be used to measure the displacement of A and C from high resolution SEM images. The whole experimental setup is shown in Figure xx which consists of the piezoactuator F, tungsten probe E, positioning stage A, B and C, and the MEMS platform D. Due to the small size of the setup, it can be placed inside the chamber of SEM allowing in situ testing.

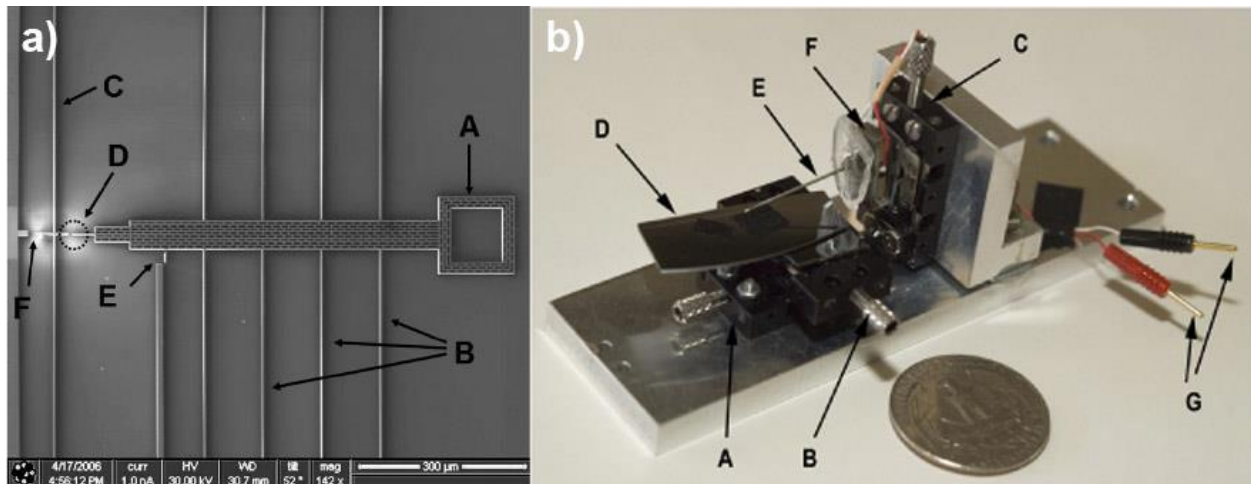


Figure 1.12. (a) SEM micrograph of the micromechanical device, the scale bar is 300 μm . (b) Jig used to apply displacement loads on the tensile testing device chip.⁴¹

Another kind of device is an integrated one which consists of both on chip actuator and sensor. Zhu³⁹ first developed such an integrated MEMS platform as shown in Figure 1.13. The actuator is either a comb-drive actuator or an electrothermal actuator, load sensor is made of four folded supporting beams whose displacement can be measured electronically through a differential capacitive sensor. Specimen is placed between actuator and load sensor. Elongation of a specimen is measured from SEM or TEM images. The resolution for force measurement can be 35nN and 3nm for displacement measurement.

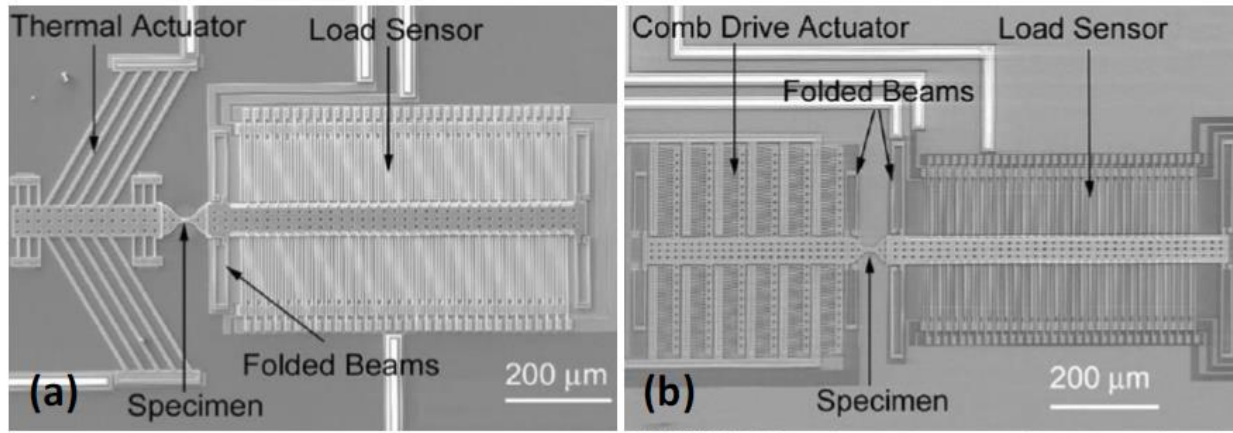


Figure 1.13. (a) In situ tensile testing device including thermal actuator, load sensor, and specimen (b) device including comb drive actuator, load sensor, and specimen.³⁹

Ever since this kind of configuration (i.e. on-chip actuator and on-chip sensor with specimen in the middle) was first introduced, a lot of similar devices with certain improvement have been developed. For example, Figure 1.14(a) shows a device developed by Zhang⁵⁵ which introduced a three-beam structure fabricated near the specimen gap, as shown in inset of Figure 1.14. Beams A, B and C are mechanically connected to a fixed part of the device, the actuator and the force sensor, respectively. During tensile tests, the movement of the three-beam structure is recorded in a video file, from which the sensor displacement (i.e. the distance change between A and C) and the specimen elongation (i.e. the distance change between B and C) are measured synchronously in each frame.

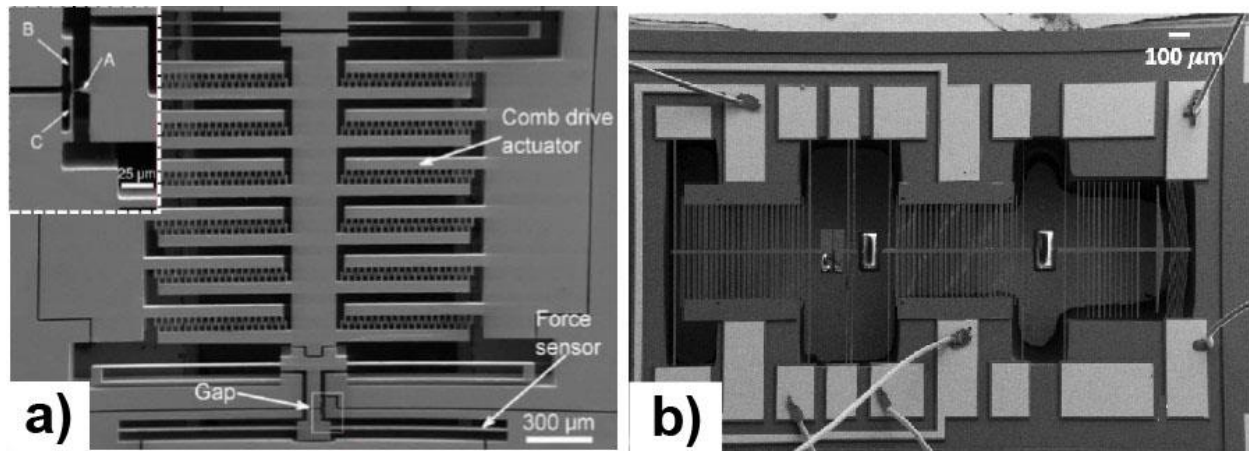


Figure 1.14. (a) SEM image of the developed on-chip tensile testing systems.⁵⁵ (b) SEM image of a MEMS wirebonded device which can electronically measure force and displacement independently.⁵⁶

Figure 1.14(b) shows a device developed by Gupta⁵⁶ which added an extra capacitive sensor placed in the middle of the specimen and actuator, with this two sensors scheme, not only the force can be measured electronically in real time from the far end displacement sensor, but also the elongation of the specimen can be measured electronically, since elongation of specimen is just the displacement difference of the two sensors. Rigid epoxy bridges are used to provide electrical isolation between the thermal actuator and capacitive sensors, which is necessary for proper functioning of the device. Figure 1.15(a) shows a device developed by Pantano⁵⁷, in which an extra parallel plate actuator is added to the far end of the load sensor, the purpose of this extra actuator is to achieve displacement controlled tensile testing. Since the specimen is placed between the actuator and a compliant load sensor, during testing both actuator and load sensor move leaving the displacement or elongation of the specimen uncontrolled. This added actuator is used to keep the load sensor still through a feedback loop as schematically shown in Figure 1.15(b), so that the elongation of the specimen is just the displacement of the actuator which can be mapped to applied voltage from the calibration data of the actuator because the actuator stiffness is two orders larger

than the specimen. In this case, the load sensor is unable to measure the force, instead force is measured from the actuation voltage applied to the added actuator.

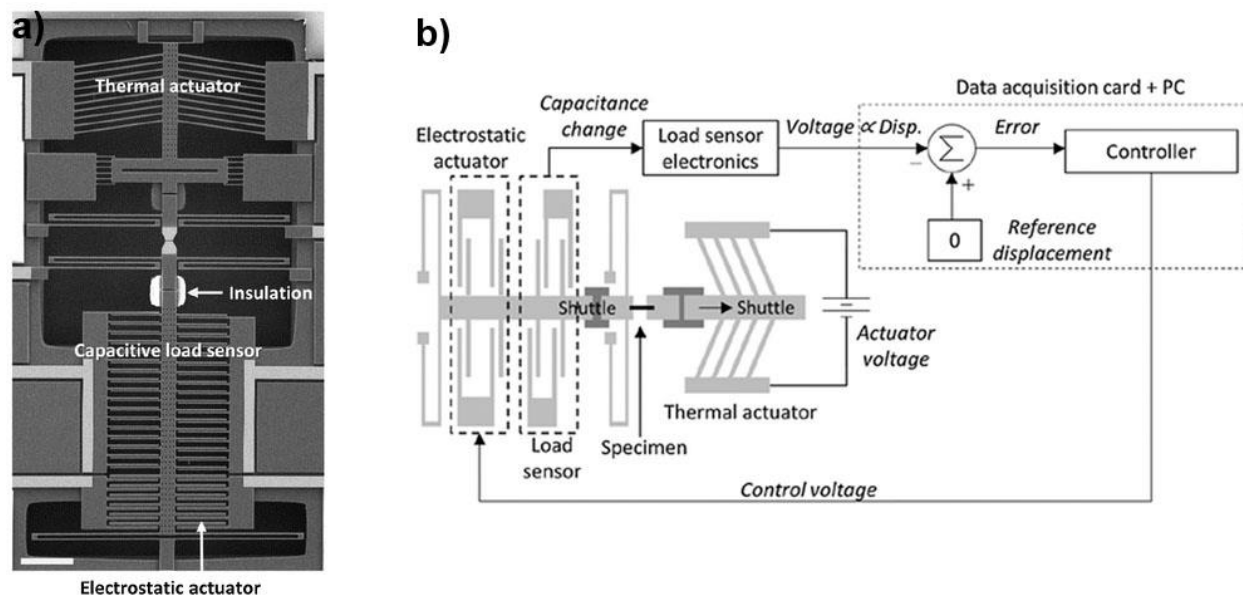


Figure 1.15. (a) SEM micrograph of the fabricated device. Scale bar 200 μm (b) Schematic of the closed-loop scheme implemented in the device for feedback control of the displacement sensor. Signals are in italics.⁵⁷

Figure 1.16 shows a platform developed by Ali⁵⁸ which is working as a nanopositioner but has the potential to be used in nanomechanical testing. It consists of an electro-thermal actuator which is connected to a thermal displacement sensor. The sensing mechanism works based on measuring the difference between the electrical resistances of two electrically biased identical silicon beams. The difference increases with displacement, as the heat conductance of the sensor beams varies oppositely with position, resulting in different beam temperatures and resistances. The sensor pair is operated in differential mode to reduce low-frequency drift.

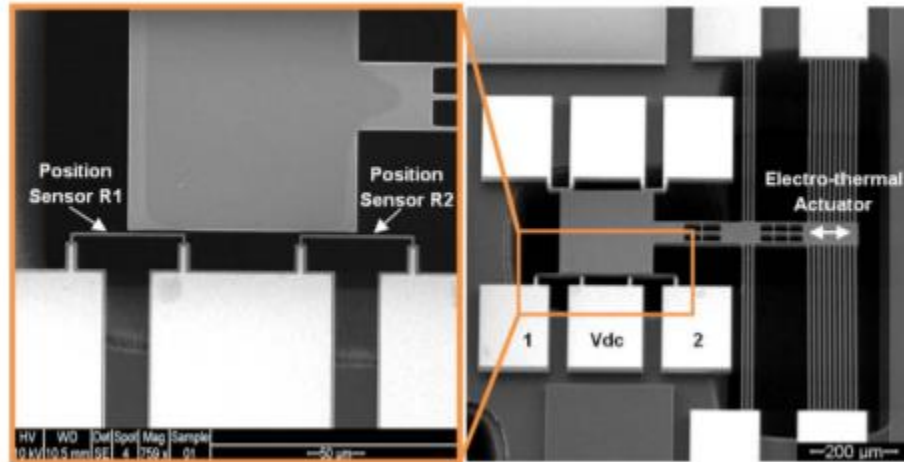


Figure 1.16. SEM images of the micromachined nanopositioner⁵⁸.

In addition of pure mechanical tensile testing, some additional functions can be incorporated into the tensile testing platform. Figure 1.17(a) shows the device developed by Chang⁵⁹ which is able to achieve high temperature nanomechanical tensile testing. A heater which consists of doped silicon beams are placed near the specimen region, when voltage is applied across the beams, temperature increases due to Joule heating. To make the specimen has a uniform temperature, the configuration is designed symmetric about the specimen. This device is able to heat up the specimen to 600 K under 8 V heating voltage in vacuum. Raman spectroscopy is used to calibrate the temperature-heating voltage relationship in air. Another MEMS device capable of conducting thermomechanical testing is developed by Kang⁶⁰, Figure 1.17(b) shows the schematic of this device. The high temperature testing capability attributes to the material used to fabricate the device, SiC which has a high melting temperature (2830 °C) and shows small variation in elastic modulus with variation of temperature. Different from the above design where temperature increases locally around the specimen area, during experiment, this whole SiC scheme is heated up resistively by applying voltage between the copper wires which are electrically connected to SiC through two metal pillars as shown in Figure 1.17(c). The temperature is measured from the

co-fabricated bi-metal type temperature sensor as shown in the inset of Figure 1.17(b). The sensor consists of two different materials with a mismatch in the coefficient of thermal expansion hence can convert a temperature variation into transverse deformation of the sensor. This device is able to sustain temperature up to 400°C. The device uses two grooves which serve as grips for a dog bone-shaped sample, as shown in Figure 1.17(d) and (e).

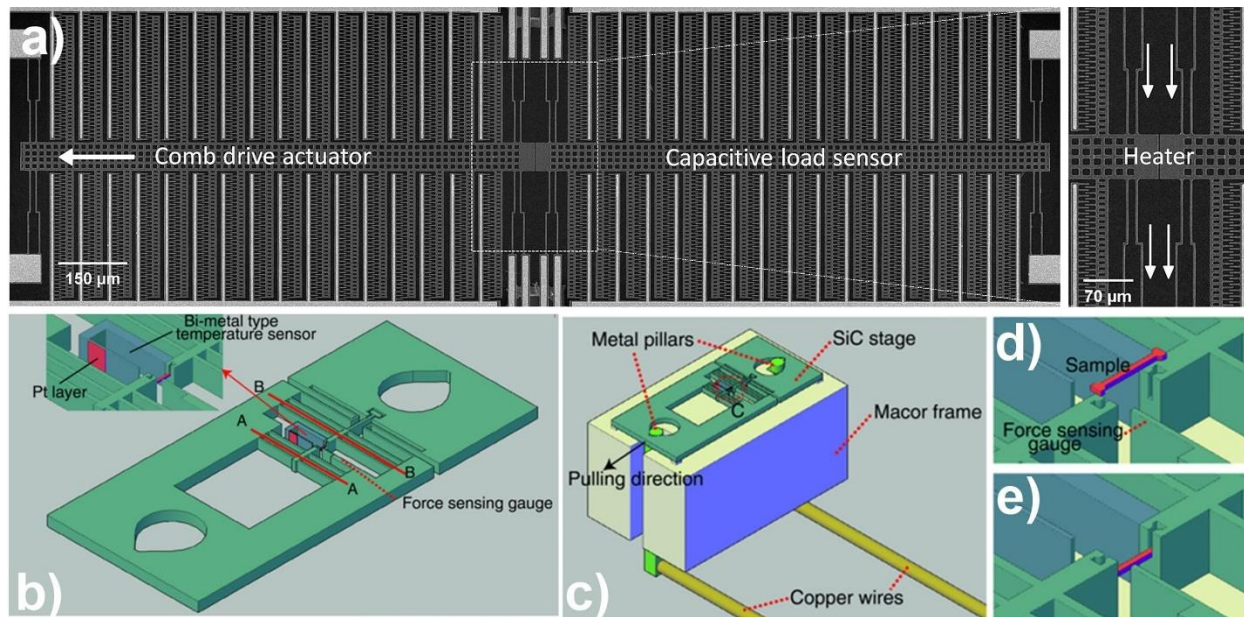


Figure 1.17. (a) SEM of thermomechanical testing platform developed by Chang.⁵⁹ (b) Overall view of the SiC stage. (c) Experimental setup for in situ uniaxial tests. (d)(e) A sample before and after assembly with the stage.

Other than thermomechanical testing, electromechanical characterization of nanomaterials is also of interested. Figure 1.18 shows a platform developed by Bernal⁶¹ which is able to carry out four point measurement of resistance of nanomaterial in addition to tensile testing. Inheriting from a previous proven design for the mechanical characterization, this design makes an improvement by incorporating an insulating silicon nitride grip (Figure 1.18(a)) to hold the specimen. Four polysilicon interconnects are positioned on top of the grip around the specimen region connecting to the outside electronics (Figure 1.18(b)). Platinum deposition is used to pattern

connections from the poly-silicon interconnects to the nanomaterial as schematically shown in Figure 1.18(c). With all that set up, four-point measurement of resistance of nanomaterial can be done.

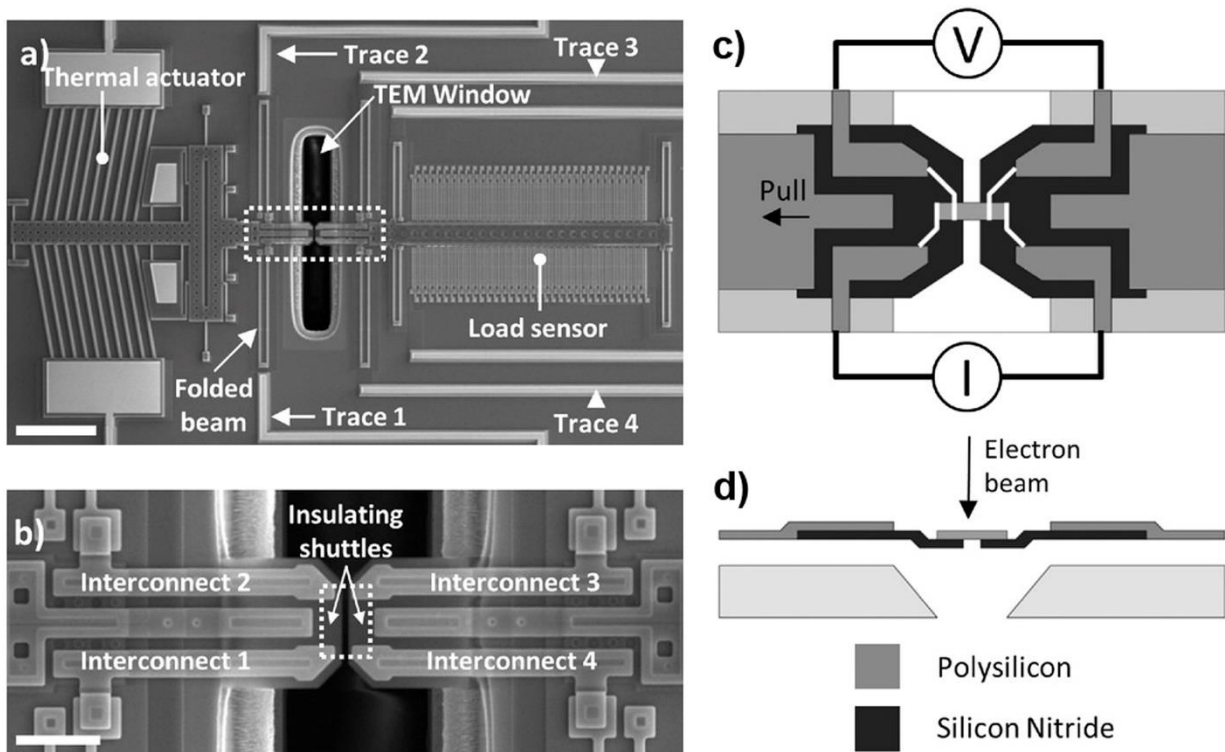


Figure 1.18. (a) SEM image showing an overview of the device. Scale bar: 200 μm . The dashed square is detailed in (b). (c) Top-view schematic of the device operation for four-point measurements. (d) Cross-section of the device.⁶¹

1.4. Recent results from nanomechanical testing

With the development of all these nanomechanical testing devices, many interesting properties of nanomaterials are revealed. Here in this section, we briefly introduce some of the recent results.

Size dependent mechanical behavior has received extensive attentions. Different mechanical properties of different nanomaterials have been investigated using MEMS-based

device. In general, they are all consistent with the “smaller is stronger” trend. For example, Young’s modulus, radial indentation modulus and tangential shear modulus of [0001] ZnO nanowire have been found to increase pronouncedly when the diameter is reduced which can be explained by a core–shell model that accounts for a bulk-like core and an elastically stiffer surface layer^{19,24}. Pent-twinned silver nanowire shows a strong size effect, a full spectrum of mechanical properties, like Young’s modulus, yield strength, and ultimate tensile strength, are all increase with decreasing diameter²¹. Size dependence of fractured strength of SiC nanowire was studied, and it was found that fracture strength increases with decreasing nanowire diameter due to the small diameter nanowire has less initial defect density⁶².

Time dependent mechanical behavior, such as relaxation and creep, is also of interest of researchers. Hosseinian et al.⁶³ experimentally studied the stress relaxation of nanocrystalline Au films with average grain size 75nm and found that plastic strain rate decreases by more than an order of magnitude during the first 30 mins of relaxation and continues to decrease in the next several hours. This relaxation was found to be due to the dislocation motion happened intergranularly and transgranularly. After several hours, the dislocation activities slowed down probably due to exhausted dislocation source or reduced applied stress. Qin et al.⁶⁴ found an interesting time-dependent deformation behavior of penta-twinned silver nanowire, where stress relaxes during loading and strain recovers during unloading. Through in situ TEM and MD simulation, it was revealed that stress relaxation is due to dislocation nucleation facilitated by the presence of vacancy and intrinsic stress field around twinning boundary supports the retraction of partial dislocation and strain recovery after unloading.

Strain rate dependent mechanical response has also been studied. Naraghi et al.⁶⁵ have studied the mechanical behavior of PAN nanofibers in situ under an optical microscope. It was

found that at fast strain rate $2.5 \times 10^{-2} \text{ s}^{-1}$, the nanofibers exhibited relatively large ductility, originated in the formation of a cascade of ripples along the length direction, while at slow strain rate $2.5 \times 10^{-4} \text{ s}^{-1}$, the nanofibers deformed homogeneously allowing for the largest engineering strengths and extension ratios. Ramachandramoorthy et al⁶⁶ experimentally studied the strain rate effect of bicrystalline silver nanowires with strain rate up to 2 s^{-1} . A brittle-to-ductile failure mode transition was observed when the strain rate exceeded 0.2 s^{-1} . TEM revealed that along the nanowire, dislocation density and spatial distribution of plastic regions increase with increasing strain rate. MD simulations show that deformation mechanisms such as grain boundary migration and dislocation interactions are responsible for such ductility.

Temperature dependent mechanical properties have also been revealed. Chang⁵⁹ carried out a study on temperature dependent brittle to ductile transition of Si. At room temperature, a single-crystalline Si NW of 60 nm shows a linear elastic stress-strain behavior while at 399K, 0.5% plastic strain was measured when the same nanowire was totally unloaded, which indicates the transition from brittle material to ductile material.

Other than mechanical properties, some physical properties have also been investigated. For example, piezoresistive coefficient along $\langle 111 \rangle$ direction increases with decreasing diameter for p-type silicon nanowires⁶⁷.

CHAPTER 2

A MEMS-based platform for displacement and force controlled nanomechanical tensile testing

2.1. Introduction

In the past decades, many kinds of nanomaterials, such as nanoparticles, nanowires, nanotubes and graphene, have been synthesized and found to exhibit extraordinary mechanical, electrical and optical properties⁶⁸⁻⁷¹. They are envisioned as the building blocks of nanotechnology and have been used in a wide range of applications. For example, carbon nanotube, due to its high electrical conductivity and ultra-high strength, has been used in field emission devices^{72, 73}, nanometer-sized electronic devices⁷⁴⁻⁷⁶, probes and nanotweezers^{77, 78}. Silver nanowires, due to its highest electrical conductivity among metals and can be stretchable when embedded in elastomeric materials, have been used in different kinds of flexible and stretchable sensors⁷⁹⁻⁸¹. For all these applications, nanomaterial involved will endure certain force or deformation, hence accurate examination of the mechanical properties of nanomaterials is necessary in order to ensure proper reliability of these applications.

As introduced in the previous chapter, over past decades, different testing methods have been used to characterize mechanical properties of nanomaterials among which MEMS-based nanomechanical testing has played an important role. Many different MEMS platforms have been developed which can measure stress and strain of a specimen, however displacement controlled mechanical testing is rarely reported. Displacement controlled testing is necessary since it is able to capture stress drop which might be caused by necking or phase transitions providing more information about material's behavior during testing. Also it is very useful for monitoring crack growth or stiffness decrease in fatigue by not fail the specimen destructively. The reason for rare

displacement controlled tensile testing is that most of these MEMS platforms measure displacement or elongation of a specimen through postprocessing optical or SEM or TEM images taken during experiments which is not compatible with a real-time feedback close loop. Although in some MEMS platforms, capacitive displacement sensors are used to measure displacement in real-time, due to the typical configuration where specimen is placed between actuator and sensor, both actuator and sensor move during testing, hence the sensor measured displacement is not equal to the specimen elongation. The two capacitive sensors scheme developed by Gupta⁵⁶ is able to measure elongation of a specimen in real time and based on that a feedback loop should be able to be implemented to achieve displacement control, but none relevant result came out until now. The platform developed by Pantano⁵⁷ is able to achieve displacement controlled testing through a feedback loop, but the working principle is quite complicated and the effect of displacement control not only depends on the performance of the feedback loop but also depends on the accuracy of the calibration of the thermal actuator.

Here in this chapter we report a MEMS-based testing platform which can achieve both displacement-controlled and force-controlled tensile testing with the implementation of a simple PID controller. Both elongation and force of a specimen can be obtained through voltage signals in real time. We will introduce the device and calibration, then the implementation of feedback loop, in the end we demonstrate the device's capability with several tensile testing experiments of different metal nanowires.

2.2. Device overview

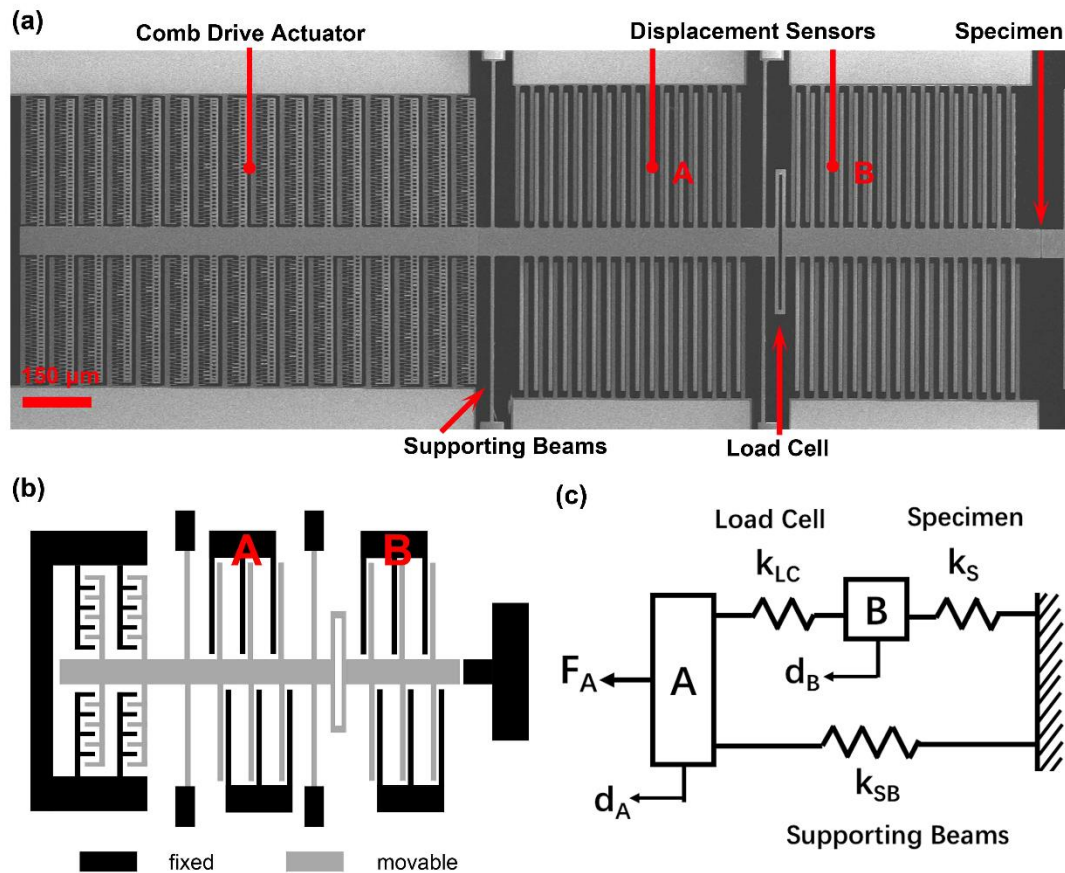


Figure 2.1. (a) SEM micrograph of the fabricated device. (b) Schematic of MEMS device configuration. (c) Device lumped mechanical model.

The MEMS platform or device was fabricated at MEMSCAP (Durham, NC) using the Silicon-on- Insulator Multi-User MEMS Process. Figure 2.1 shows a SEM image, schematic and lumped mechanical model of the MEMS device. The device consists of a comb-drive actuator, two displacement sensors (A and B) and a folded beam load cell (sensor). The central shuttle of the device is supported by four straight beams. A specimen is to be placed across the gap between Sensor B and the fixed anchor. Elongation of the specimen is simply determined by the displacement of Sensor B. The force in the specimen is equal to elongation of the load cell (displacement difference between Sensors A and B) multiplied by the stiffness of the load cell

because forces in the specimen and the load cell are equal (two springs connected in series). Stress and strain of the specimen can further be calculated given the specimen's gauge length and cross-sectional area.

A capacitive readout AT1006 is connected to the two sensors, it converts displacement induced capacitance change into voltage which will be described in detail in section 3.2. With this readout, both force and elongation of a specimen can be measured electronically in real time which enables the implementation of feedback control loop to achieve displacement and force controlled tensile testing. In addition, compared with devices described in last chapter where displacement is measured from images hence experiment is either conducted inside SEM(TEM) or under optical microscope, this readout enables the device to be used for ex-situ and time-consuming tests, such as fatigue test which may last hours or days in different environments.

2.2.1. Comb-drive actuator

The actuator used in this work is an electrostatic comb-drive actuator. As mentioned in last chapter, comb-drive actuator can provide a constant force under a constant actuation voltage regardless of the travel distance and with no heating effect. The actuation force is proportional to the actuation voltage square as given by⁸²

$$F_A = N_A \varepsilon \left(\frac{t}{g} \right) V^2 \quad (2-1)$$

where N_A is the number of pairs of comb fingers, ε is the permittivity, t (nominal value 25 μm) is the thickness of the MEMS structure, g (nominal value 2 μm) is the lateral gap between comb fingers, and V is the actuation voltage. For the configuration reported in this paper, we have $N = 1056$ pairs of fingers, providing actuation force of 105 μN under applied DC voltage $V=30$ volt.

2.2.2. Displacement sensor

Both sensors (A and B) are differential capacitive sensors consists of parallel plates⁸³, schematic of one unit of which is shown in Figure 2.2(a). The expression of differential capacitance between movable electrode and two fixed electrodes is as follows where fringing field is neglected due to the high aspect ratio,

$$\Delta C = 2N_s \varepsilon A d \left(\frac{1}{g_1^2 - d^2} - \frac{1}{g_2^2 - d^2} \right) \quad (2-2)$$

where N_s is the number of pairs of parallel plates, A is the overlapping area of two adjacent plates, and g_1 and g_2 are the initial gaps between the fixed plate and movable plates. If g_1 is designed much smaller than g_2 and d is small compared to g_1 , this differential scheme can provide a quasi-linear relationship^{39, 57} between displacement d and capacitance difference ΔC ,

$$\Delta C \approx 2N \varepsilon A \frac{d}{g_1^2} \quad (2-3)$$

Figure 2.2(b) estimates the linear region for the device by plotting the relationship between ΔC and d using both Eq. (2-2) and Eq. (2-3), the dimensions used in the calculation are measured from SEM images. As can be seen, when the displacement is less than 350 nm, the differential capacitance is almost linear with displacement, and theoretical sensitivity for both sensors within 350 nm range which is large enough to break a series of nanowires can be estimated to be 0.4fF/nm.

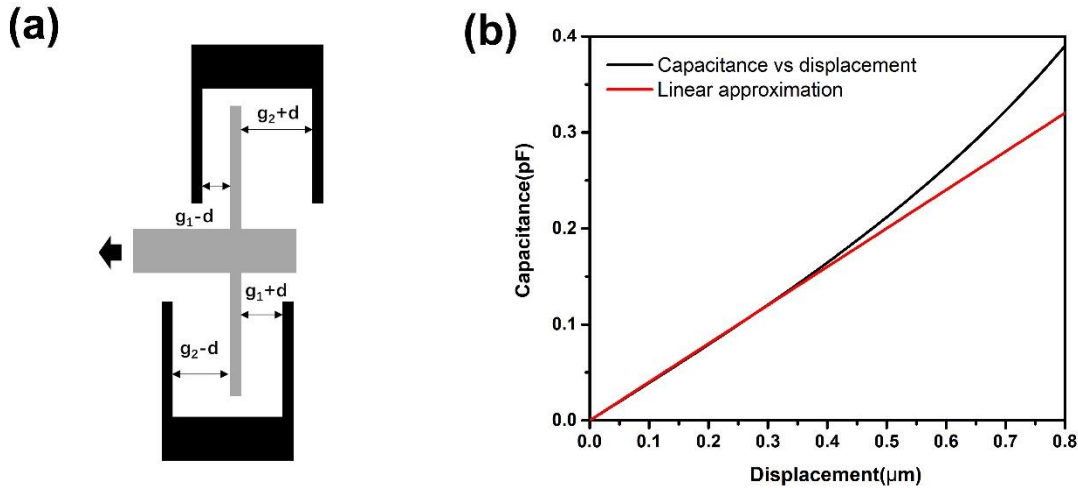


Figure 2.2 (a) Schematic of one unit of differential capacitive sensor. (b). Estimation of linear region of the capacitive sensor.

2.2.3. Load cell

Just like most MEMS platforms, a compliant structure is used as the load cell. The load cell use here is a o-shaped structure as shown in Figure 2.3(a) which is consist of four clamped-guided beams whose stiffness can be estimated using simple beam theory as

$$k_{LC} = \frac{Ew^3t}{L^3} \quad (2-4)$$

where E is the Young's modulus of Si, t is the thickness of the structure, w and L are the width and length of the clamped-guided beam. Figure 2.3(b) shows the deformed shape of the load cell under tension. Two factors are considered when design load cell stiffness. On one side, load cell stiffness is related to the force resolution, the smaller the stiffness the higher the resolution. On the other side, smaller stiffness means larger travel range, and for comb-drive actuator, lateral pull-in might happen destroying the device when the moving combs of actuator travels too much. Hence a series of o-shaped load cell with different stiffnesses were designed aiming to test nanomaterials with different strength. Finite element analysis (FEA) software Ansys was used to obtain the accurate

stiffness of a load cell after precisely measuring the dimensions from high resolution SEM images.

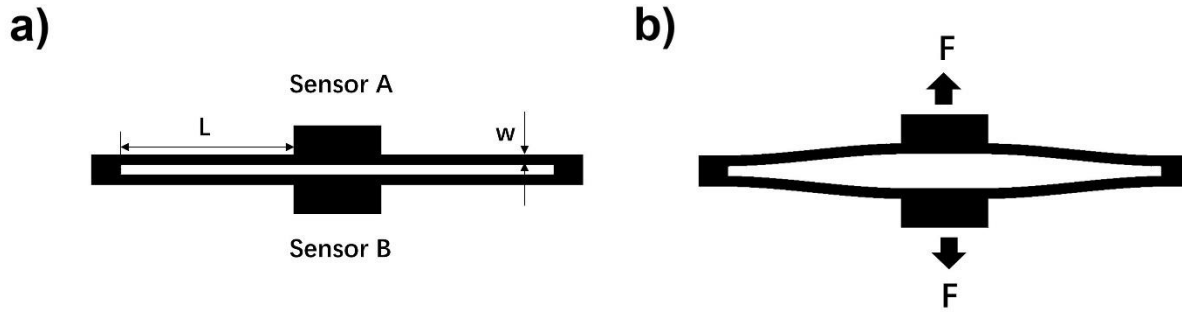


Figure 2.3. (a) Dimensions in a o-shaped load cell. (b) Deformed load cell under tension.

2.3. Results and discussion

2.3.1. Calibration of actuator

To calibrate the actuator, a DC voltage was applied to the stationary electrode of the actuator while the moving electrode of the actuator (i.e. the shuttle) and other electrodes were grounded. The DC voltage increased gradually with a 2V step. Corresponding displacement was extracted from SEM images focusing on the specimen gap area (Figure 2.4(a)(b)). Displacement was plotted against the actuation voltage showing a quadratic relationship which is consistent with the actuation mechanism (Figure 2.4(c)). The experimentally measured displacement-voltage relationship is compared with analytical calculation. Because the shuttle is in equilibrium under each voltage level, generated electrostatic force equals the deflection force of supporting beams when no specimen is mounted, the theoretical displacement of shuttle can be calculated using the following equation:

$$d = \frac{F_A}{k_{SB}} = \frac{N_A \epsilon t V^2}{g^2 k_{SB}} \quad (2-5)$$

where F_A is the actuation force calculated using Eq. (2-1), k_{SB} is the stiffness of the four supporting beams. Such analytical results are in good agreement with experiment results, as shown in Figure

2.4(c).

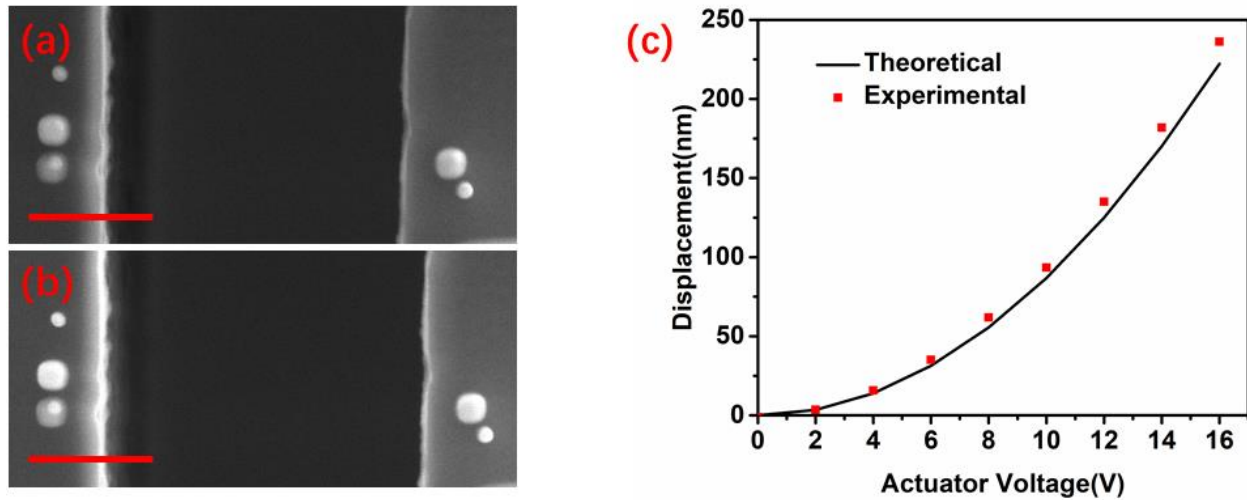


Figure 2.4. Comb-drive actuator calibration results. (a) Specimen gap when actuation voltage is 0V. (b) Specimen gap when actuation voltage is 14V. Scale bar is 1 μ m. (c) Analytical and experimental relationship between actuation voltage and displacement.

2.3.2. Calibration of displacement sensor

A commercially available differential capacitive readout (AT1006, ACT-LSI)⁸⁴ was used to convert capacitance difference (ΔC) of opposing two capacitors into an output voltage. Figure 2.5(a) shows the function blocks of AT1006 and its connection to the MEMS chip. The readout is designed as the signal conditioning circuit for capacitive three-axis acceleration sensors, hence it can be connected to up to three capacitive sensors and converts the differential capacitance of the three sensors into three channels' output voltage. For our research only two channels (X and Y) are used which are connected to Sensors A and B, respectively. The core of AT1006 is a capacitance to voltage (C/V) conversion circuit (i.e. an op amp integrator with periodically on-off switch across the feedback capacitor C_{FB}), three channels share to use this circuit in a time division manner which is achieved by applying shifted periodic modulated pulses to the sensors. The

converted voltage is held in a sample and hold circuit in synchronization with the applied pulse for each channel. The gain (or sensitivity, maximum is 150V/pF) and offset can be trimmed through registers inside and data can be stored in an on-chip EEPROM. Figure 2.5(b) shows an image of the MEMS chip integrated with the readout. The MEMS chip was wirebonded to a 28-pin-dual-in-line package (DIP) which sits on a 28 pin ZIF socket. The pins of socket corresponding to the electrodes of sensors are connected to the evaluation board of AT1006 through copper wires (underneath the board not shown in the image).

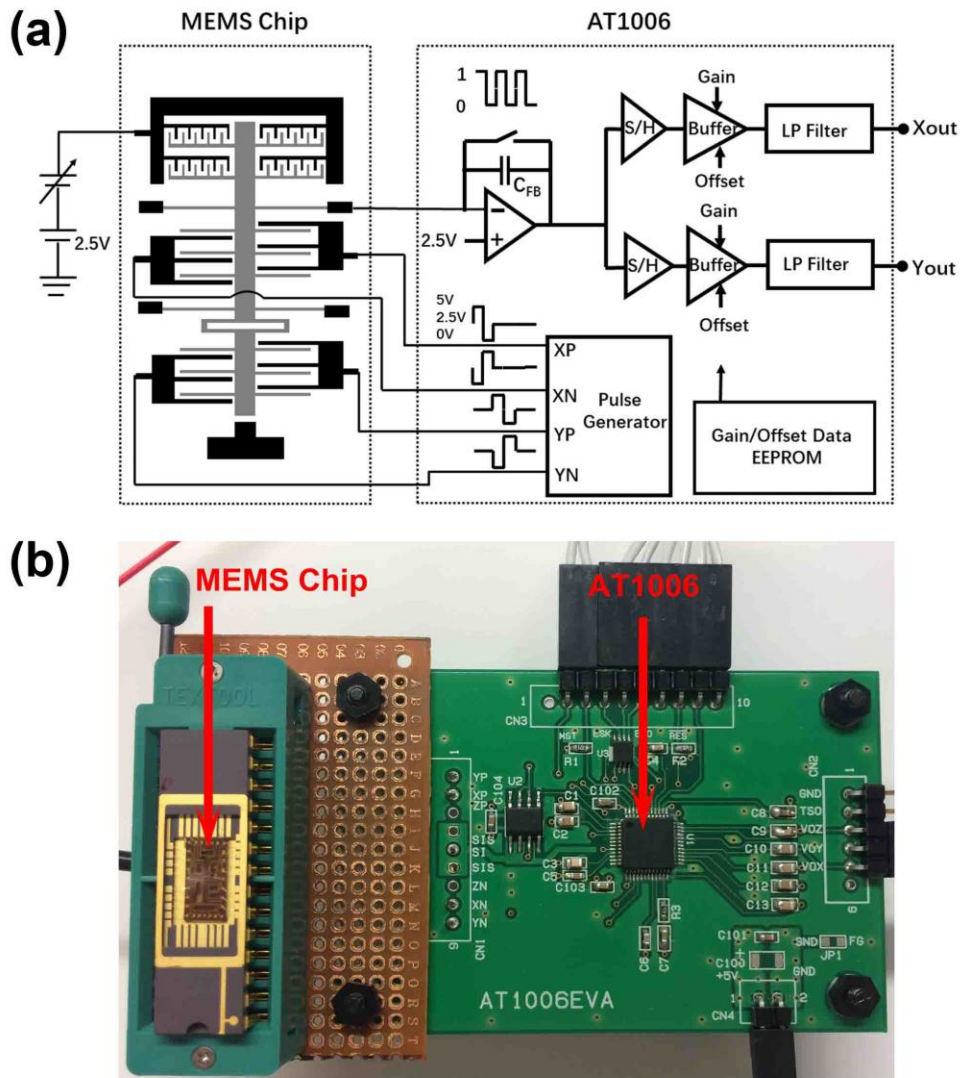


Figure 2.5. (a) Functional block diagram of capacitive readout AT1006 and its connection with MEMS device. (b) Image of the MEMS device and capacitive readout.

Before the readout can be used to measure displacement, calibration of the relationship between displacement and AT1006 output voltages change was conducted. To calibrate the displacement sensor, actuation voltage was increased with a 2V step again, at each voltage level the output voltage for both channels were acquired for a short period of time and then averaged to eliminate the noise. Capacitance change was then calculated for each voltage level and then plotted

against displacement, the calibration result is linear as shown in Figure 2.6, in good agreement with Eq. (2-3).

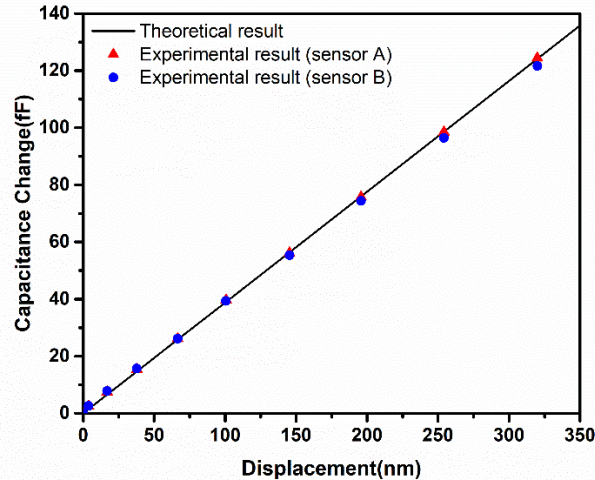


Figure 2.6. Comparison of theoretical and experimental relationship between capacitance change and displacement for both displacement sensors.

2.3.3. Implementation of feedback control

After calibration, both sensors' displacement can be obtained in real-time from the output voltage of the readout. Since Sensor B's displacement is the elongation of a specimen, in order to achieve displacement controlled (elongation controlled) testing, this monitored displacement can be used as the process variable, which is fed into a simple PID controller in a feedback loop. Figure 2.7(a) shows the schematic of such a feedback loop we built to control the elongation of a specimen. The operation of the system is as follows. Y-channel output of readout AT1006 is first sampled by a digital acquisition card (DAQ, NI USB 6211), the sampled voltage is then transferred to a Labview program, this program first converts the voltage into displacement of sensor B based on the calibration result, this measured displacement is then compared with the expected displacement

of Sensor B (setpoint), the error between them is fed to a PID controller, and the digital output signal of the controller is transferred to the analog output port of the DAQ, in the end the output voltage from DAQ is amplified and serves as the actuation voltage of the device.

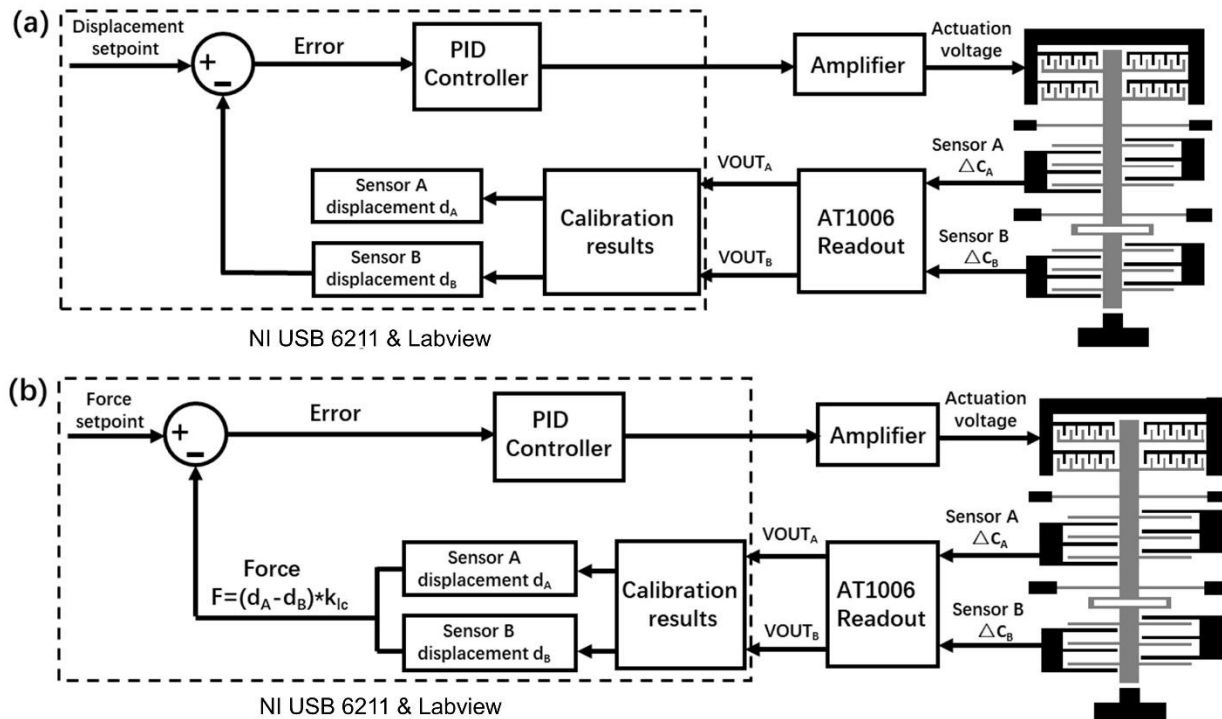


Figure 2.7. Closed-loop block diagram for achieve (a) displacement control. (b) force control.

Other than controlling displacement, the current device configuration is also very suitable for force control. The schematic of a feedback loop for controlling force is shown in Figure 2.7(b), it is similar to the one for displacement control, the only difference is an extra step (i.e. force calculation using the equation shown in image) is added after getting the displacements of both the two sensors.

The performance of feedback displacement control was examined in terms of speed and accuracy. To evaluate control speed, step response for 50nm input was studied. The parameters of the PID controller were tuned to achieve a fast response with no overshoot and no steady-state

error. Figure 2.8 shows the system response to step input after tuning, the rise time (the time required for the response to rise from 10% to 90% of its final value) is about 18 ms.

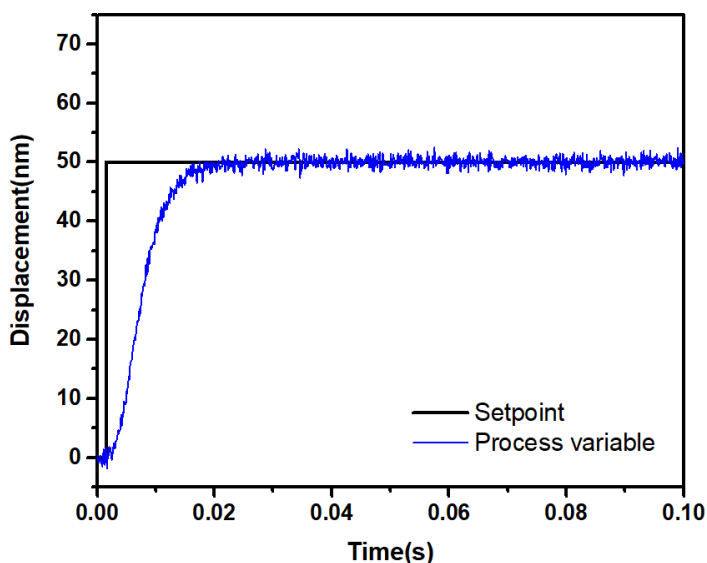


Figure 2.8. Step response of the feedback close-loop scheme.

To study control accuracy in actual tensile testing, a pentatwinned Ag nanowire was mounted on the device inside FIB (FEI Quanta 3D FEG), the nanowire was picked up from substrate using a nanomanipulator (Klocke Nanotechnik, Germany) and clamped on the device by e-beam induced Pt deposition as shown in Figure 2.9(a) to (c). After mounting the nanowire, the displacement setpoint was hold at 0nm, 20nm,40 and 60nm for about 3 mins during which period about 20 optical images were taken from which displacement was extracted. Figure 2.9(d) shows the profile of displacement setpoint together with the measured actual displacement at the holding periods. A statistical analysis of the data reveals that the mean value of measured displacement is within the ± 0.26 nm of the setting point and the standard deviation is less than 0.6 nm.

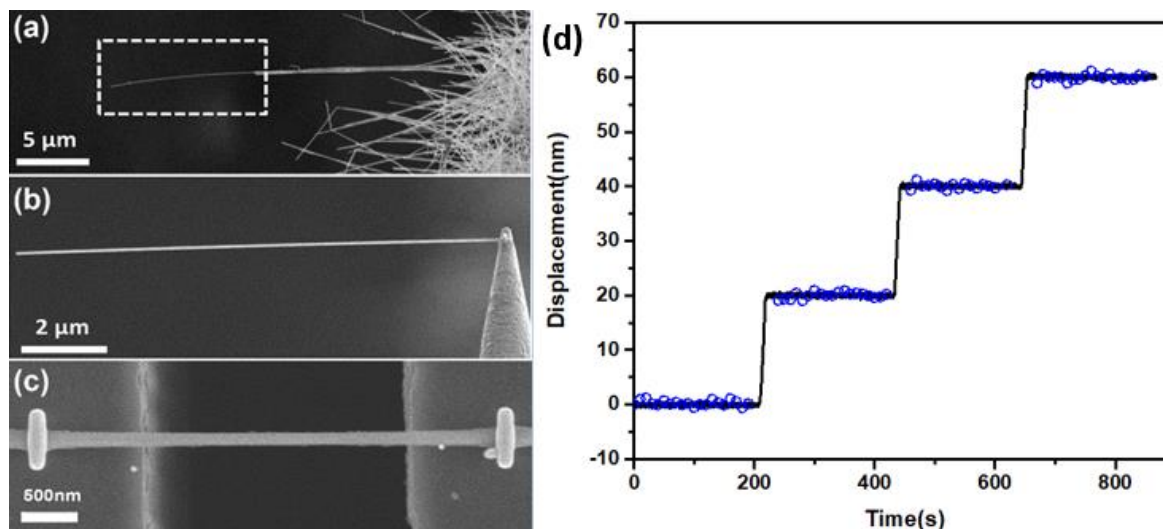


Figure 2.9. Steps for mounting a nanowire on device (a) choose a nanowire from substrate (b) pick up the nanowire with a manipulator. (c) mount the nanowire on device with Pt-deposition. (d) Displacement setpoint (line) versus measured displacement (dots).

2.3.4. Mechanical demonstration

In order to demonstrate the device's capabilities, tensile testing was carried out when metal nanowires were mounted on the device. Three representative test results are shown below. Force and elongation of a specimen were obtained from readout's output voltage with method aforementioned. Given the diameter and gauge length of a specimen (measured from SEM image before testing), stress and strain were calculated assuming the cross-section is of circular shape.

To verify the device's function of controlling displacement, penta-twinned Ag nanowire would be a good choice as specimen. As mentioned in chapter 1, penta-twinned Ag nanowire shows a stress relaxation behavior when it is stretched to certain strain level and held there. The reason is due to vacancy diffusion assisted nucleation of leading partial dislocation which has been verified from both experiment and MD simulation⁶⁴. The previous experiment was done using a MEMS-based device which is not able to control displacement. Same kind of experiment was

conducted here with this new MEMS-based testing platform. After mounting the Ag nanowire with gauge length 2750 nm, displacement setpoint for the feedback loop was increased gradually to 40nm and then kept at that value for about ten minutes. Figure 2.10(a) shows the stress-strain curve of the specimen, corresponding strain versus time and stress versus time relationships are shown in Figure 2.10(b)(c). As can be seen, an obvious stress relaxation was recorded during the holding period while strain was kept unchanged which indicates this MEMS device is able to control displacement.

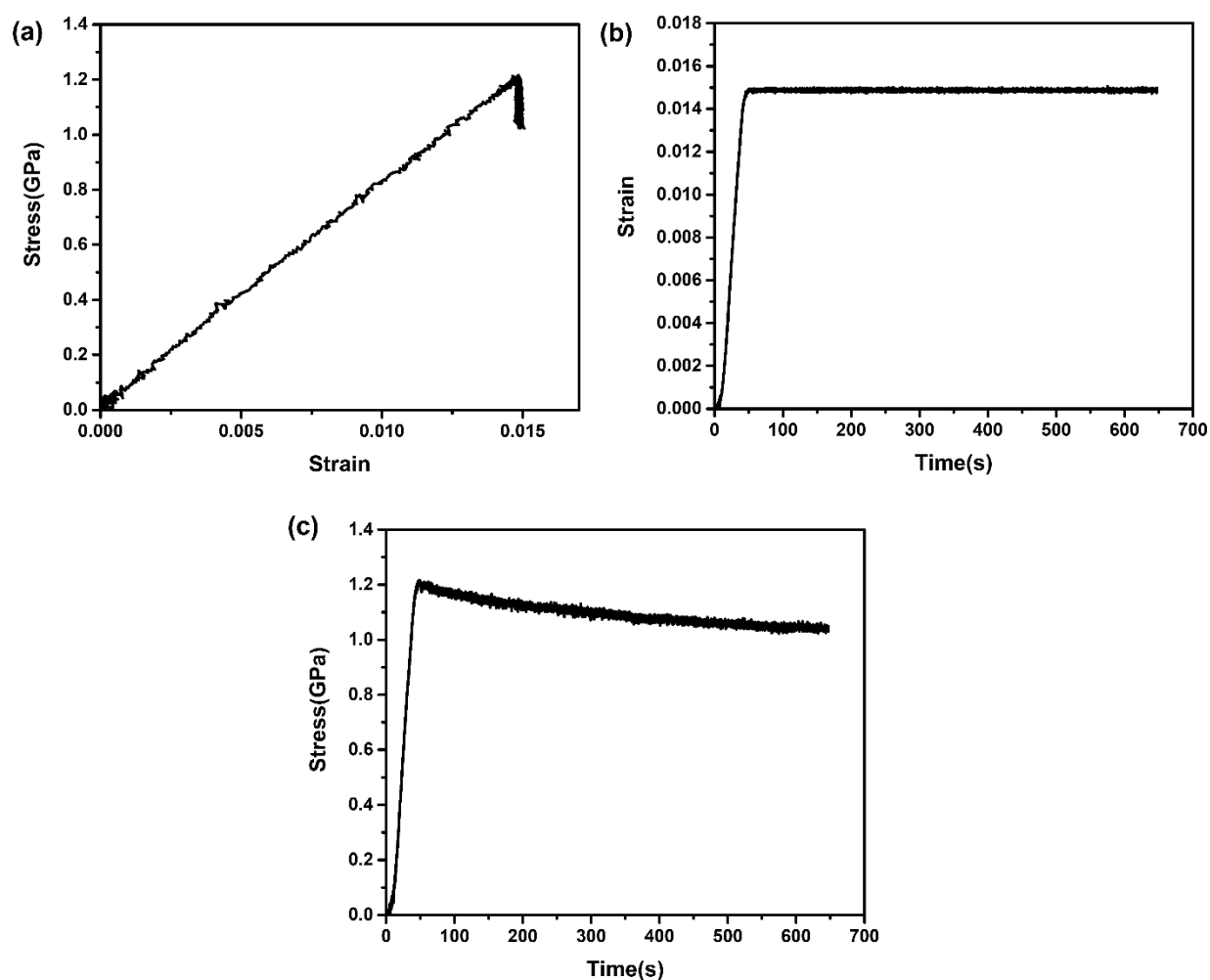


Figure 2.10. Stress relaxation of penta-twinned Ag nanowire. (a) Stress vs Strain. (b) Strain vs Time. (c) Stress vs Time.

Another test result is also able to prove the effectiveness of this displacement controlled platform. In this test, the platform is used to stretch an Au nanowire until fracture, the desired displacement was set to be linearly increasing with time. Figure 2.11 shows the stress-strain, strain-time, stress-time curve for this test. As can be seen in Figure 2.11(a), the stress initially increased linearly with strain until strain reached 1.75% which is the proportional limit, young's modulus of 83.5GPa was obtained based on the gradient in this region. After 1.75% strain, the stress-strain curve showed a tendency of levelling off indicating plastic deformation or strain hardening began to occur. At strain 2.15%, a drastic stress drop was captured following which stress increased again until fracture. The stress drop is probably due to sudden nucleation and propagation of multiple leading partial dislocations from the surface which has been reported in previous MD simulations of FCC metal nanowires^{66, 85-87}. From Figure 2.11(b)(c), when the stress drop happened, the strain or displacement kept following the displacement setpoint which proves this platform is able to carry out displacement controlled tensile testing.

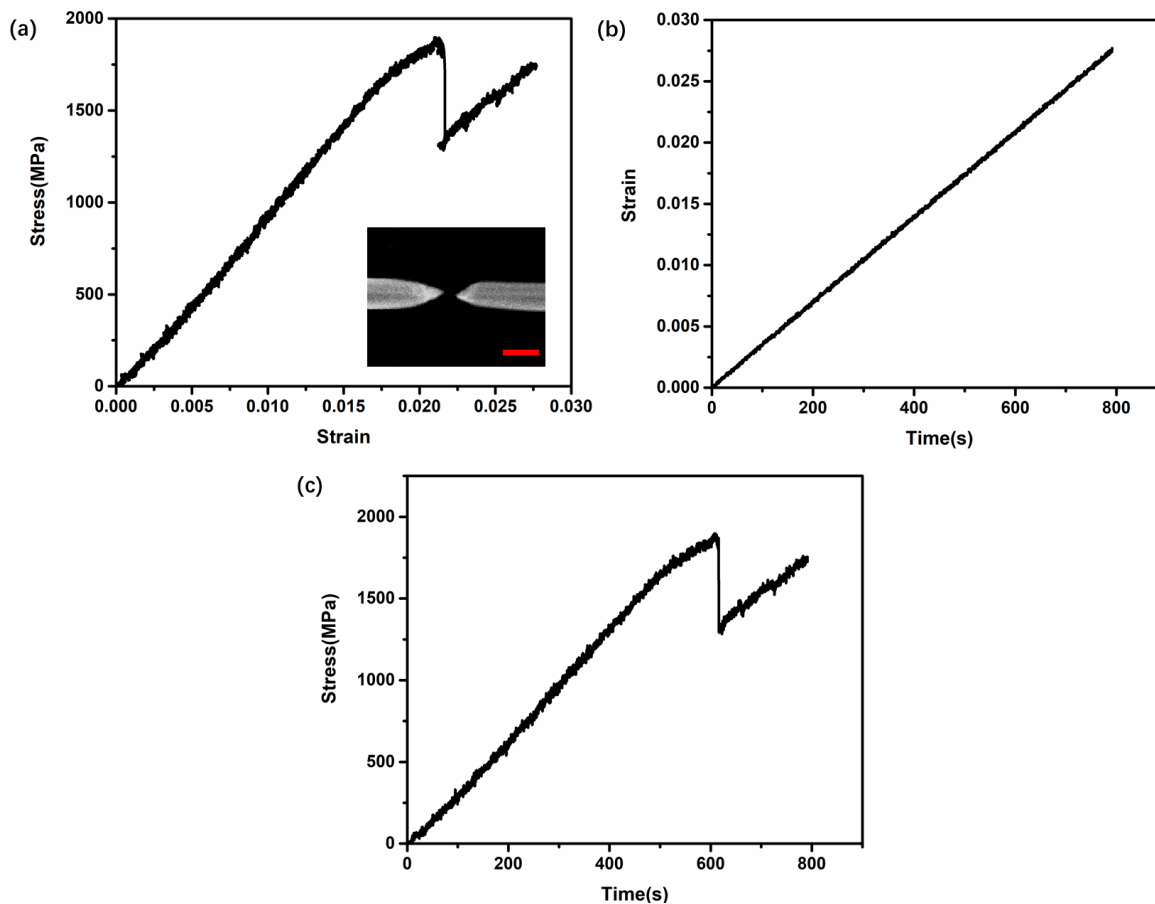


Figure 2.11. Displacement-controlled stretching an Au nanowire until fracture. (a) Stress-strain curve. Insert is fracture surface, scale bar is 150nm. (b) Strain vs Time. (c) Stress vs Time.

To test the device's capability on force control, a creep test was carried out where force was kept constant after loading the specimen to certain stress level. The nanowire we used for the test was penta-twinned Ag nanowire again. Relationships between stress and strain, strain and time, stress and time are shown in Figure 2.12. It was found that during the hold period strain gradually increased while stress of the specimen remained constant indicating the MEMS device is able to conduct force controlled tensile test.

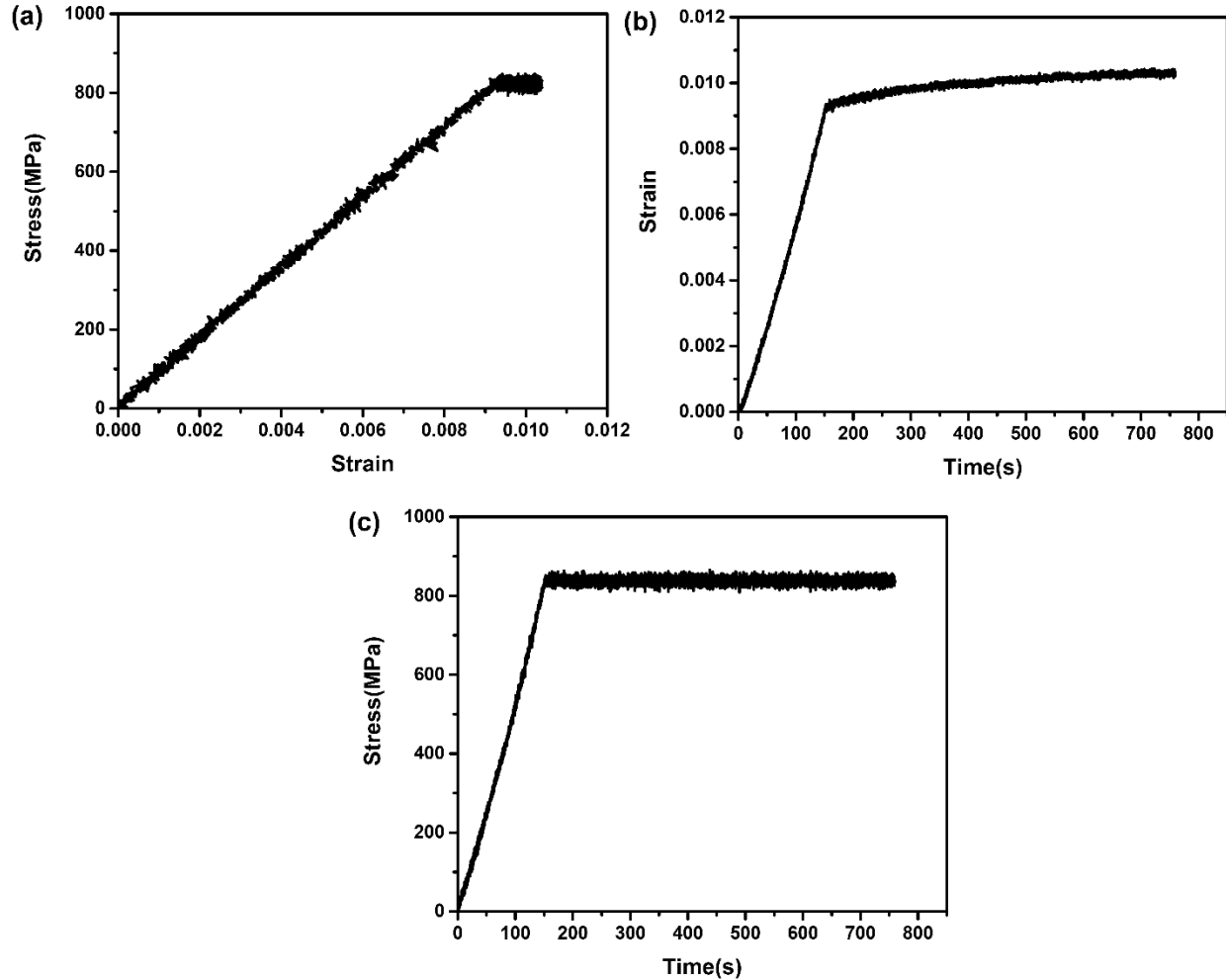


Figure 2.12. Creep of penta-twinned Ag nanowire. (a) Stress vs Strain. (b) Strain vs Time. (c) Stress vs Time.

2.4. Conclusions and future developments

In summary, we reported a MEMS device for tensile testing nanomaterials which consists of an electrostatic actuator and two capacitive displacement sensors with a load cell in between. Combining the device with the sensing electronics, real time measurement of elongation and force of a specimen can be obtained. The advantage of this device is both displacement control and force control can be achieved with the implementation of a PID controller after calibration of the sensors.

Tensile testing of Ag and Au nanowires was conducted. Three representative results, i.e. stress-relaxation of penta-twinned Ag nanowire, stress-drop of Au nanowire and creep of penta-twinned Ag nanowire, were presented which prove the device's capability of doing displacement-controlled or force-controlled tensile testing of nanomaterials. In future, fatigue test of different nanowires can be carried out based on the capabilities demonstrated here. Fatigue of nanowires remains a large research area unexplored but is necessary since many applications of nanomaterials involves cyclic loading. Dynamic characterization the device can also be conducted which will help us explore the device's capability on high-strain rate testing of nanomaterials.

CHAPTER 3:

An on-chip nanomechanical testing device: dynamic response and application for high strain-rate testing

3.1. Introduction

For the past decades, many different MEMS-based tensile testing platforms have been developed as introduced in chapter 1, however most of these platforms are only able to carry out nanomechanical testing quasi-statically, dynamic testing especially high strain-rate testing of nanowires remains an area largely unexplored. It is in great need to conduct high strain-rate testing since nanowires especially metal nanowires can behave differently at high strain-rate^{66, 88, 89}, which is of relevance to applications where these 1D nanomaterials are subject to high-rate loadings.

It is challenging to conduct high strain-rate nanomechanical testing since the apparatus must have an actuator with fast actuation speed and sensors with short response time. Naraghi et al.⁹⁰ reported testing polymer nanofibers with strain rate up to 200 s^{-1} using a MEMS-based on-chip load sensor and an external piezoelectric actuator. The external actuator provided the fast actuation, while force and displacement were measured from high-speed optical images using digital image correlation (DIC). However, this off-chip actuation method adds complexity for in-situ scanning or transmission electron microscope (SEM/TEM) testing and might be challenging in handling smaller samples such as nanowires (with diameters generally less than 100 nm).

As for the on-chip method, the strain-rate attained so far has been quite limited, typically less than 10^{-1} s^{-1} ^{88, 89}. Ramachandramoorthy et al.⁶⁶ reported the strain rate to 2 s^{-1} with an on-chip MEMS thermal actuator. Fast-response capacitive sensor was used to measure force and displacement. However, the thermal actuator limited the actuation speed due to the relatively slow heat transfer process. Nevertheless 2 s^{-1} is the largest strain rate that has been reported in tensile

testing of nanowires. It is important to further increase the strain rate. A potential solution is to employ other types of MEMS actuators that can respond faster.

In this chapter, we systematically investigated the dynamic response of the MEMS-based nanomechanical testing device introduced in last chapter which has an on-chip electrostatic actuator in air and inside SEM (near vacuum environment) to explore the maximum actuation speed or maximum strain rate it can attain. Analytical dynamic model is built to delineate the device's frequency response and response to ramping force. Dynamic responses of the device are measured in air and in vacuum and compared with the modeling results. The maximum strain rate that the device can attain is then discussed based on the modeling and experiment results. It is found that this device is able to achieve strain rate around 200 s^{-1} ; however, the capacitive readout can only measure strain rate up to 22 s^{-1} due to its limit in bandwidth. Finally, two gold nanowires are tested at strain rates of 10^{-5} s^{-1} and 10 s^{-1} in SEM to demonstrate the general capability of the device for high strain-rate nanomechanical testing.

3.2. Device Description

The MEMS-based device is the same one as introduced in last chapter, however the device working principle is a little bit different under dynamic testing versus under static testing due to the existence of damper. A revised lumped mechanical model of the device considering damping effect is shown in Figure 3.1. Elongation of a specimen can still be measured from the displacement of sensor B. Force measurement is a little bit different. For quasi-static tensile testing, then force in the specimen is simply equal to force in the load cell which is product of stiffness of the load cell and elongation of the load cell that can be measured from the readout output voltages as introduced in last chapter. For dynamic tensile testing, the force in a specimen equals force in

the load cell minus the damping force and inertia force. The force measurement under this situation will be discussed later. Stress and strain of the specimen can further be calculated given the specimen's gauge length and cross-sectional area.

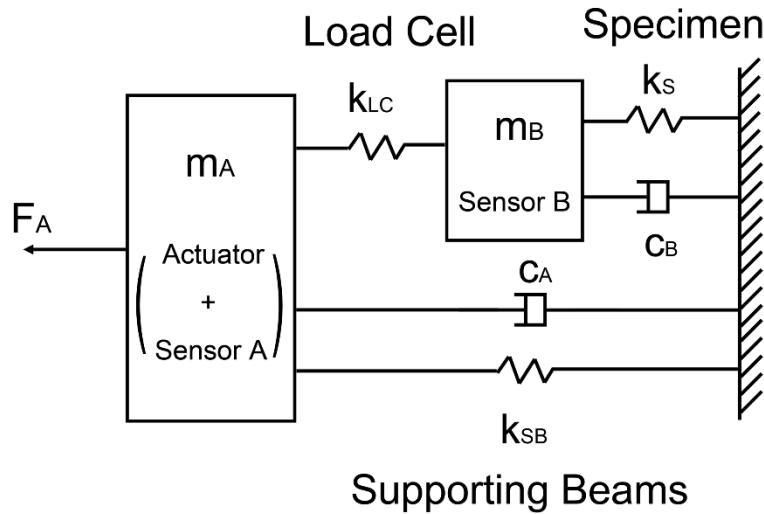


Figure 3.1. Schematic of lumped mechanical model of the device under dynamic testing.

Since displacement of Sensor B is the elongation of specimen, strain rate of the specimen can simply be defined by

$$\dot{\epsilon} = \frac{1}{l_0} \frac{\partial d_B}{\partial t} \quad (3-1)$$

where d_B is the displacement of Sensor B, $\frac{\partial d_B}{\partial t}$ is the velocity of Sensor B, and l_0 is the gauge length of the specimen.

3.3. Modeling

Based on the lumped mechanical model shown in Figure 3.1, equations of motion of the device can be written as

$$m_A \ddot{d}_A + c_A \dot{d}_A + k_{SB} d_A + k_{LC} (d_A - d_B) = F_A \quad (3-2)$$

$$m_B \ddot{d}_B + c_B \dot{d}_B + k_S d_B - k_{LC} (d_A - d_B) = 0 \quad (3-3)$$

where m_A is the total mass of the moving portion of Sensor A and the actuator, m_B is the mass of the moving portion of Sensor B, d_A and d_B are the displacements of m_A and m_B , respectively, k_{SB} , k_{LC} and k_S are the stiffness of the supporting beams, load cell and specimen, respectively, and c_A and c_B are the damping coefficients with respect to m_A and m_B , respectively.

3.3.1 Frequency response: vacuum and air

For a linear system, frequency response of the system can be characterized by its transfer function. In order to find out transfer function of this MEMS device, a state-space model was constructed based on the aforementioned equations of motion, viz.,

$$\dot{\mathbf{X}} = \mathbf{A}\mathbf{X} + \mathbf{B}u \quad (3-4)$$

$$y = \mathbf{C}\mathbf{X} \quad (3-5)$$

where state vector $\mathbf{X} = \begin{bmatrix} d_B \\ \dot{d}_B \\ d_A \\ \dot{d}_A \end{bmatrix}$, state matrix $\mathbf{A} = \begin{bmatrix} 0 & 1 & 0 & 0 \\ -\frac{k_{LC}+k_S}{m_B} & -\frac{c_B}{m_B} & \frac{k_{LC}}{m_B} & 0 \\ 0 & 0 & 0 & 1 \\ \frac{k_{LC}}{m_A} & 0 & -\frac{k_{LC}+k_{SB}}{m_A} & -\frac{c_A}{m_A} \end{bmatrix}$, input matrix

$\mathbf{B} = \begin{bmatrix} 0 \\ 0 \\ 0 \\ \frac{1}{m_A} \end{bmatrix}$, and input $u = F_A$. Here only the displacement of Sensor B is chosen as the output since

it is directly related to the specimen elongation, hence output $y = d_B$ and output matrix $\mathbf{C} = [1 \ 0 \ 0 \ 0]$. The system transfer function is then written as

$$G(s) = C(sI - A)^{-1}B$$

$$= \frac{k_{LC}}{m_A m_B s^4 + (c_A m_B + c_B m_A) s^3 + (c_A c_B + k_{SB} m_B + k_S m_A + k_{LC} (m_A + m_B)) s^2 + c_B (k_{LC} + k_{SB}) s + c_A (k_{LC} + k_S) s + k_S k_{SB} + k_{LC} k_S + k_{LC} k_{SB}}$$
(3-6)

where $s = j\omega$ with ω as the angular frequency, and I is the identity matrix. In Eq. (3-6), $m_A = 1.68 \times 10^{-8}$ kg and $m_B = 5.99 \times 10^{-9}$ kg, $k_{SB} = 107$ N/m, and $k_{LC} = 850$ N/m. Supporting beam stiffness and load cell stiffness were estimated by finite element analysis based on the measured dimensions using SEM. k_S is zero when there is no specimen mounted.

In vacuum, the damping coefficients c_A and c_B are zeros. With all the system parameters known, transfer function of the device in vacuum can be calculated using Eq. (3-6). Figure 3.2 plots the bode magnitude plot of the system, which characterizes the relationship between radial frequency ω of the input actuation force F_A and the magnitude of the output displacement d_B with respect to displacement at $\omega = 0$. Since the system has two degrees of freedom, two peaks can be found corresponding to two undamped natural frequencies, $\omega_1 = 72,193$ rad/s and $\omega_2 = 440,997$ rad/s (correspondingly $f_1 = 11,490$ Hz and $f_2 = 70,187$ Hz). Note that without damping, the magnitude approaches infinite at the natural frequencies. Mode analysis was conducted using finite element analysis software Ansys, it was found that the first two in-plane resonance happens at frequencies 11493 Hz and 67006 Hz which is similar to the analytical prediction. The mode shapes for the resonance are shown in Figure 3.3.

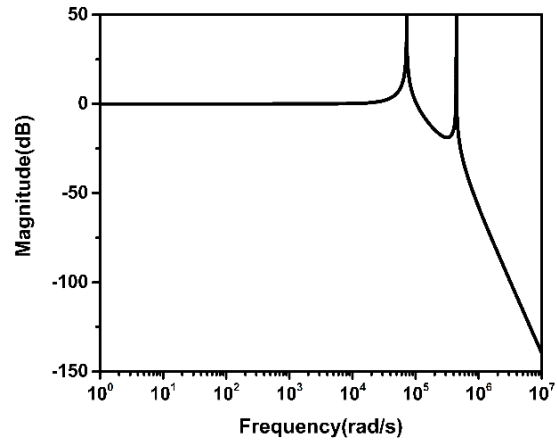


Figure 3.2. Bode magnitude plot of the device obtained from Eq. (3-6).

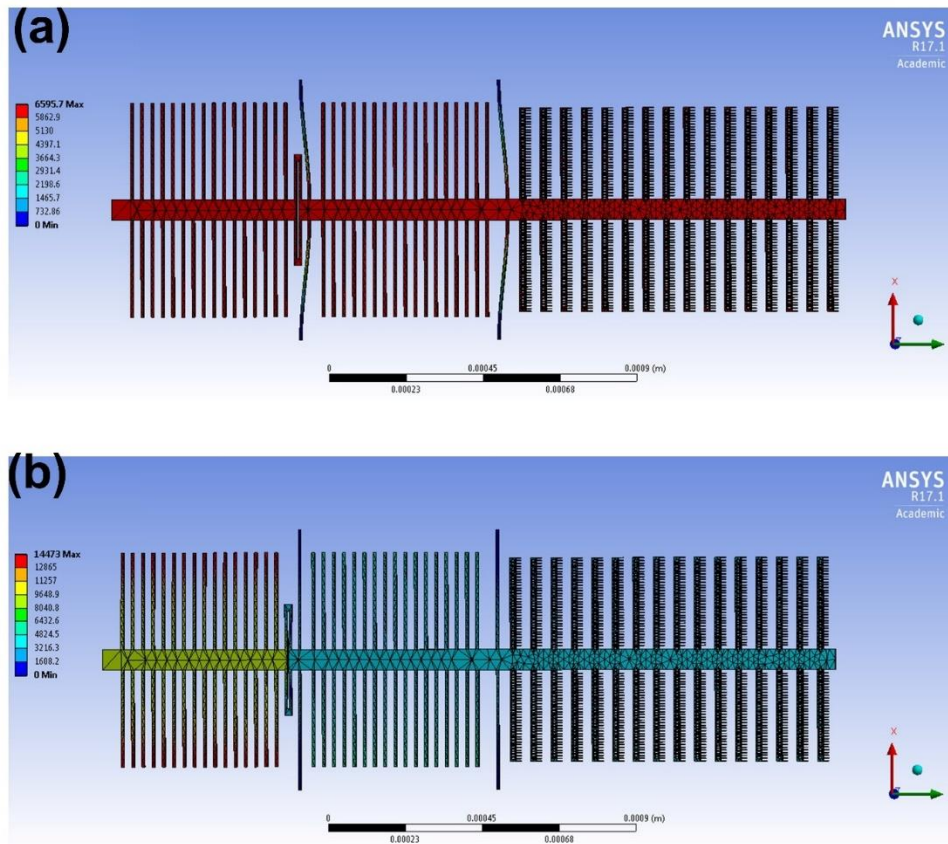


Figure 3.3 The mode shapes for the first two in-plane resonance.

In air, the damping effect needs to be considered. The damping coefficients c_A and c_B must be known in order to characterize the dynamic response of the device under AC actuation force.

The two natural frequencies in air, ω_3 and ω_4 , are expected to be smaller than their counterparts in vacuum if the device is underdamped in air. The damping coefficients of the device in air will be determined through experiments as described in Section 4.2.

3.3.2 Dynamic response under ramping actuation force: vacuum and air

To attain a constant strain rate in the specimen, i.e., constant velocity of Sensor B, a ramping force $F_A = pt$ is chosen as the input to the device, where p is a constant.

In vacuum, the damping coefficients are zeros, hence the device model is simplified to a two-coupled-mass-spring system. The system transient output $d_B(t)$ has the following form

$$d_B(t) = \frac{pt}{k_{SB}} - a_1 p \sin(\omega_1 t) + a_2 p \sin(\omega_2 t) \quad (3-7)$$

where a_1 and a_2 are constants that can be calculated with the known system parameters (e.g., m_A , m_B , k_{SB} , k_{LC}) (both independent of p), and ω_1 and ω_2 are the two natural frequencies of the system in vacuum as identified in Section 3.1. The output form of this two-coupled-mass-spring system is similar to that of a single-mass-spring system (see Appendix). As shown in Eq. (3-7), $d_B(t)$ is the superposition of a linear displacement $\frac{pt}{k_{SB}}$ and two sinusoidal displacements, which is schematically shown in Figure 3.4(a). The linear displacement is the ideal displacement of Sensor B to achieve a constant strain rate in the specimen. The two sinusoidal displacements can be considered as deviation from the ideal linear displacement. Magnitude of the deviation is proportional to p . When p is small, the deviation is negligible, which is the case for quasi-static loading. However, this does not hold if p becomes large.

In air, considering the damping effect, the device model becomes a two-coupled-mass-spring-damper system. The system transient output $d_B(t)$ has the following form

$$d_B(t) = \frac{pt}{k_{SB}} - a_3p - a_4pe^{-a_5t}\sin(\omega_3t + a_6) + a_7pe^{-a_8t}\sin(\omega_4t + a_9) \quad (3-8)$$

where a_3 to a_9 are constants (a_5 and a_8 are positive) that can be calculated with the known system parameters (e.g., m_A , m_B , k_{SB} , k_{LC} , c_A , c_B) (all independent of s), and ω_3 and ω_4 are the two resonance frequencies of the system in air. The form is again similar to that of a single-mass-spring-damper system (see Appendix). Displacement d_B contains a linear term $\frac{pt}{k_{SB}}$ (the ideal displacement), a constant offset term a_3p , and two attenuated sinusoidal terms. Here the sum of the last three terms is the deviation with a magnitude also proportional to p . Figure 3.4(b) shows schematically the displacement $d_B(t)$ in this case.

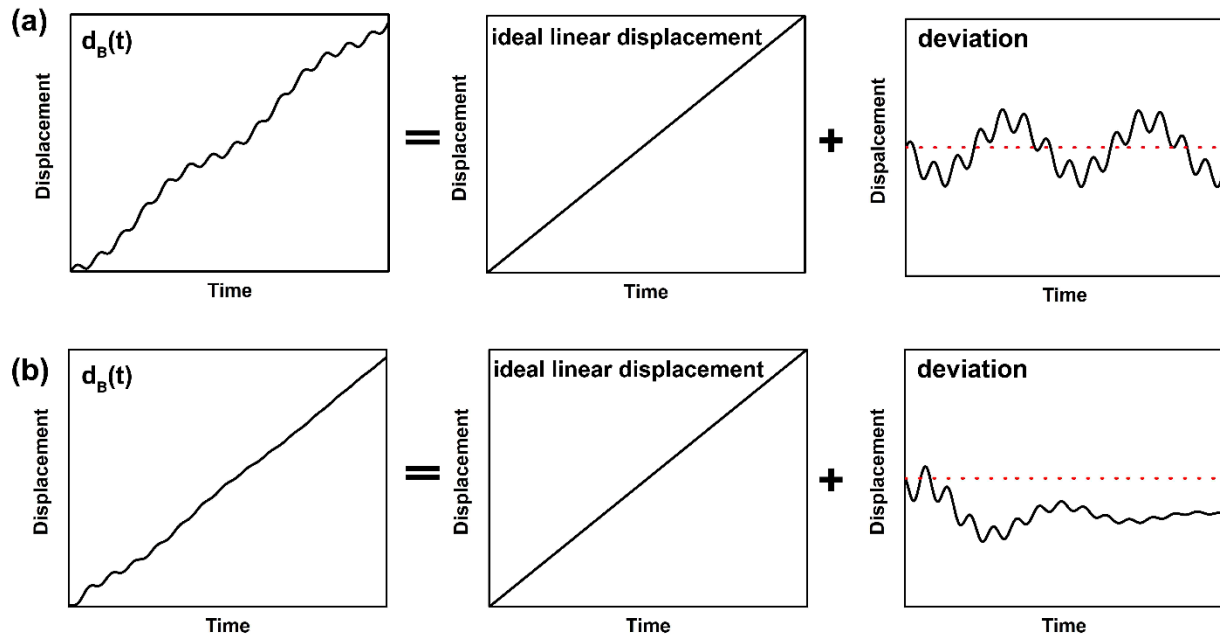


Figure 3.4. Illustration of Sensor B displacement when device is actuated by a ramping force (a) in vacuum, (b) in air. For both cases, Sensor B displacement is the superposition of an ideal linear displacement (constant velocity and correspondingly constant strain rate) and deviation. Horizontal dashed line marks zero deviation.

3.4. Experiments

3.4.1 Displacement measurements

Dynamic response of the device was also measured experimentally. Two methods were employed to measure displacement – optical imaging and capacitance readout. To image the displacement under dynamic testing, a high-speed camera (Phantom v4.3 with maximum frame rate 95,000 fps) was integrated to a Nikon LV150 microscope, as shown in Figure 3.5. A light source (SOLA SE II 365) was used to provide strong white light needed for the high-speed imaging.

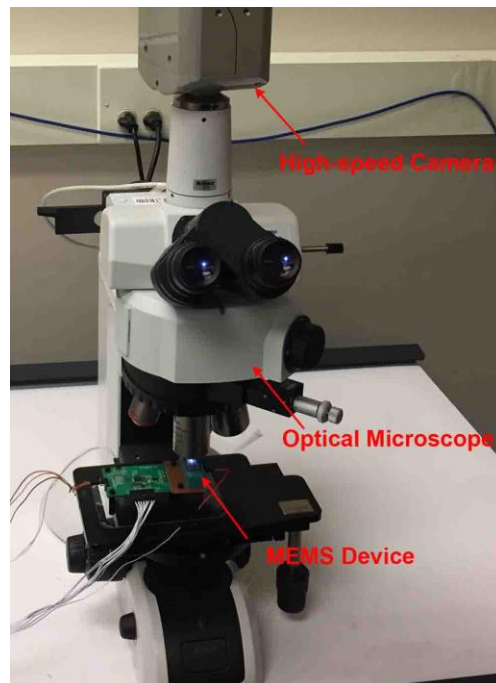


Figure 3.5. Experiment setup (high speed camera and optical microscope) to measure the dynamic displacement of the device

Recorded images were then processed using an image correlation method to obtain displacement. The method used here is based on the shift theorem of discrete Fourier transformation (DFT)⁹¹. First, a series of optical images were taken recording the motion of Sensor B or position of Sensor B at different moments (Figure 3.6(a)). Subsequently the images were cropped to the same region of interest – some parallel beams connected to the shuttle which is a

periodic pattern as marked by red rectangle in Figure 3.6(a). For each cropped image, the gray value of pixels in each column was averaged to produce a 1D periodic pixel intensity profile (Figure 3.6(b)), which was then analyzed using DFT (Figure 3.6(c)). Since displacement in spatial domain (Figure 3.6(b)) corresponds to phase shift in frequency domain (Figure 3.6(c)), the phase of the fundamental frequency which is the spatial frequency of the periodic pattern was recorded for each image and phase shift between images was then converted back to the spatial domain to calculate the displacement. A fixed periodic structure can also be chosen as the region of interest (green rectangle in Figure 3.6(a)) to serve as reference, whose displacement can be subtracted from the displacement of the moving structure to remove common motion induced noises such as vibration.

When compared with other displacement measurement techniques based on image processing, such as the commonly used DIC, this single frequency-based DFT method has the advantage that it is less affected by image noise since only phase of the fundamental frequency is used to retrieve displacement. It has been demonstrated that even blurring and defocusing of optical images have little effect on the precision and accuracy of measurement results using this method^{92, 93} because blurring and defocusing act as low-pass filters hence only the higher order harmonics are degraded, leaving the fundamental frequency mostly untouched. This feature makes this method particularly suitable for dynamic displacement measurement since device is moving during exposure time of an image, leading to certain degree of blurring. One limitation of this displacement measurement method originates from the nature of high-speed camera that high frame rate must be compensated by reduced field of view. The small field of view at high frame rate has two consequences, one is that it can't include both sensors at the same time hence force in a specimen remains unknown which limits this optical method to be used in high strain rate testing

where both stress and strain need to be obtained, the other is it rises the uncertainty in measured displacement as for the single frequency-based DFT method the less the repeated patterns are captured and used in the analysis the worse the measurement accuracy will be⁹¹. Another limitation of this method is that it is not suitable to measure displacement inside electron microscopes.

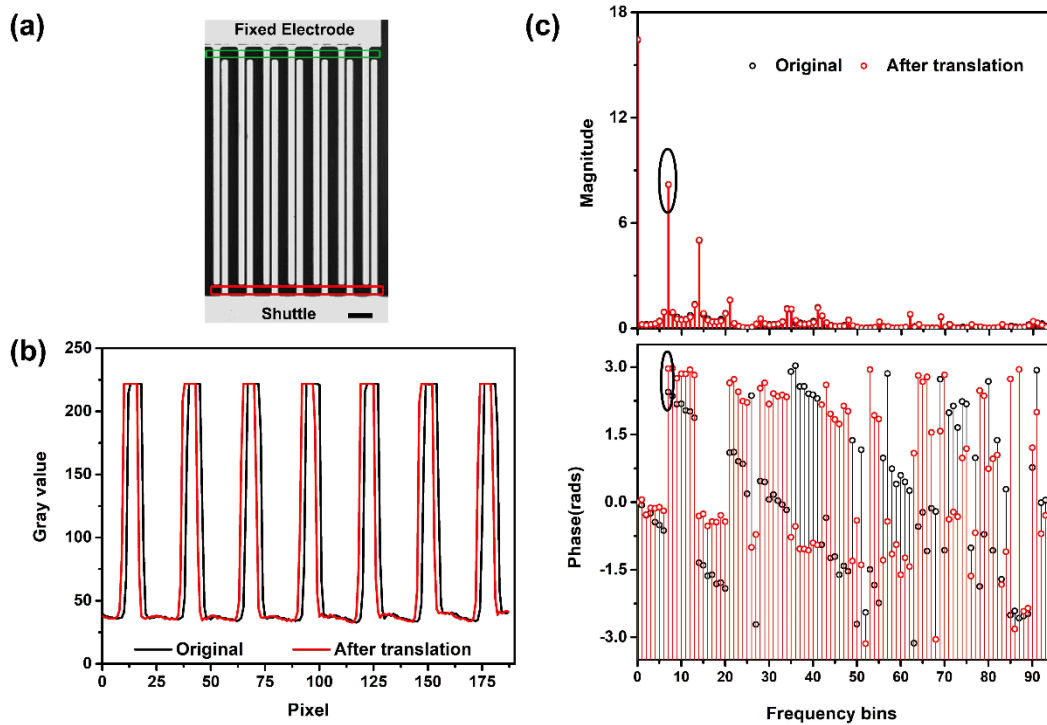


Figure 3.6. (a) One frame of high-speed image taken under microscope. Scale bar 30 μm . (b) 1D line intensity profile of the periodic patterns in region of interest before and after translation. (c) DFT of the line intensity profile before and after translation, upper is magnitude plot, lower is phase plot. Fundamental frequency corresponding to spatial frequency of periodic patterns is circled out. Phase shift of fundamental frequency is used to retrieve translational displacement.

The other method is using the capacitive readout circuit AT1006 mentioned in last chapter. Compared with the optical method, this method has two major advantages: 1) it can be used both in air and in vacuum, and 2) it can measure displacements of both sensors A and B at the same time with which force in a specimen can be calculated hence it can be used to in mechanical testing

of nanowires. Unfortunately the bandwidth of this readout is relatively low ($\sim 1,100$ Hz), to be reported later, which prevents this method from measuring high-frequency signals.

3.4.2. Frequency response

To study frequency response, AC actuation voltage with $V_{pp}=30$ V and different frequencies was applied to the actuator. Function generator Agilent 33250A was used to provide the voltage. Amplitude of the output displacement d_B was measured as a function of the actuation force frequency. Note that there is a factor of 2 between the actuation voltage frequency and the resulting actuation force (or displacement) frequency because of the square relationship as shown in Eq. (2-1).

Since only the electronic method can be used to measure displacement in vacuum but its relatively low bandwidth makes it unable to detect the resonance peaks as predicted in Section 3.1, measurements were focused on the dynamic response under AC actuation force in air using the optical method. For the optical method, in order to improve the measurement accuracy, a larger field of view and more periodic beams are preferred, as discussed in Section 4.1. Hence to accurately measure displacement at high frequency, a low frame rate associated with large field of view was used. This way “aliasing” would occur hence the measured frequency is not the actual displacement oscillation frequency, but amplitude of the oscillation can still be retrieved correctly if the frame rate and exposure time are set properly. For example, a low frame rate of 100 fps with short exposure time can be used for displacement oscillation of 2,002 Hz (the actuation voltage frequency is purposely set as 1,001 Hz). In this case, an image is taken every 20.02 displacement oscillation cycles, these images record different phases of the oscillation waveform, from which the oscillation amplitude can be retrieved. Figure 3.7(a) shows the optically measured

displacement of sensor B in this situation. As can be seen, although the measured frequency is not correct, the displacement amplitude was clearly recorded. Displacement amplitudes at different frequencies were then normalized by the amplitude at 1Hz. Figure 3.7(b) shows the measured relationship between normalized displacement amplitude and actuation force frequency. Only the lower resonance frequency in air was measured which is 10,600 Hz, a little bit smaller than the counterpart in vacuum 11,490Hz calculated by the model in Section 3.1.

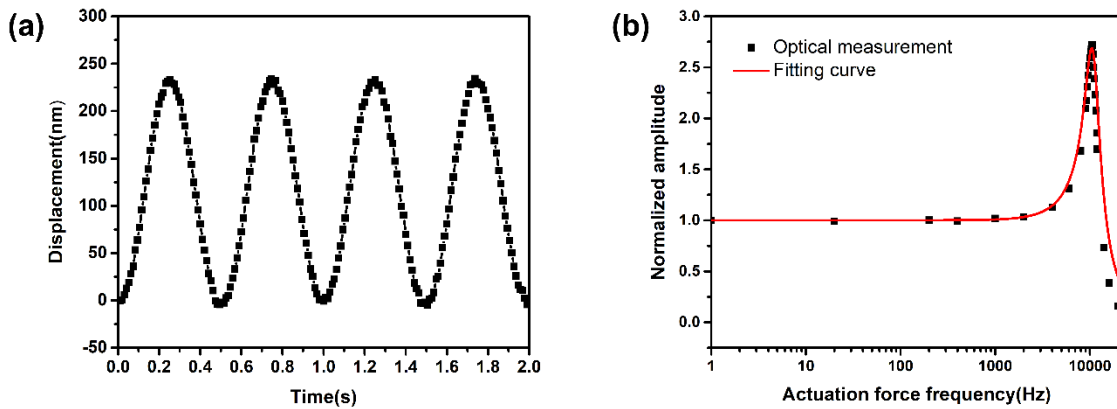


Figure 3.7. (a) Optically measured displacement with frequency 2002 Hz, the frame rate used is 100 fps. (b) Relationship between actuation force frequency and normalized displacement amplitude measured using optical image processing method. The optical measurement result was fitted and damping coefficients in air were obtained.

This measured relationship was then fitted using magnitude of normalized transfer function $\left| \frac{G(j2\pi f)}{G(j2\pi)} \right|$, where the denominator accounts for the normalization at 1 Hz. By fitting the curve in Figure 8, damping coefficient in air $c_A = 3.09 \times 10^{-4}$ kg/s and $c_B = 2.83 \times 10^{-4}$ kg/s were obtained which were used to simulate the device displacement in air under ramping actuation force in the next section.

3.4.3. Dynamic response under ramping actuation force: vacuum and air

In this section, to find out the maximum strain rate this device can attain, a ramping actuation force with gradually increasing loading velocity was applied to the device in both vacuum and air while Sensor B displacement was measured.

To provide a ramping actuation force, a predefined actuation voltage profile $V(t) = qt^{0.5}$ was applied to the comb-drive actuator. A series of testing was conducted, during which the actuation voltage was increased from 0 to 15 V while the time taken to increase from 0 to 15 V, here defined as loading time, was gradually decreased to increase the loading velocity. Figure 3.8 shows the actuation voltage profile when the loading time was 1 s, in which case $q = 15$ in the actuation voltage profile, the corresponding loading velocity is 226 nm/s calculated using the model.

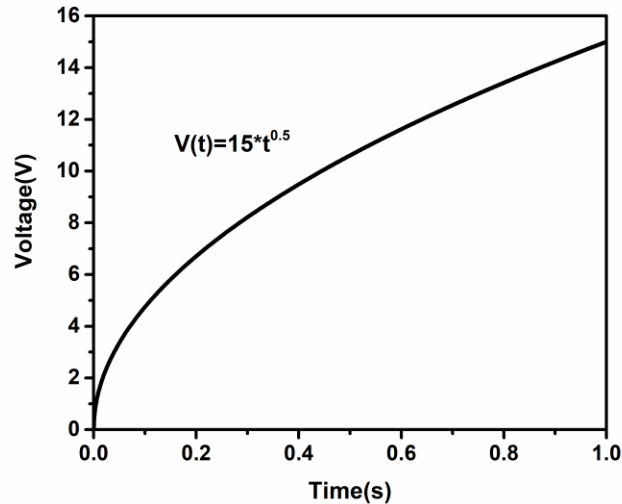


Figure 3.8. Voltage applied to device to achieve ramping actuation force, loading time is 1s.

The vacuum experiments were conducted inside a SEM (FEI Quanta 3D FEG) chamber. Note that here the vacuum was an approximation. The displacement d_B was measured using the capacitive readout and compared with the modeling result according to Eq. (3-7). Figure 3.9 shows

the comparison when the loading velocity was 226 nm/s, 45.2 $\mu\text{m/s}$, 226 $\mu\text{m/s}$ (corresponding loading time of 1 s, 5 ms, 1 ms). When the loading velocity was 226 nm/s (Figure 3.9(a)), the measured and modelled displacements agreed very well both increasing linearly with time. When the loading velocity was increased to 45.2 $\mu\text{m/s}$ (Figure 3.9(b)), the electronically measured displacement started to show a small lag compared to the modelled displacement (about 2% smaller) due to the limitation in bandwidth. The sensor B velocity 45.2 $\mu\text{m/s}$ in this case was thus considered to be the upper bound that can be measured using the capacitive readout AT1006, with the corresponding maximum strain rate of about 22 s^{-1} (assuming the specimen length of 2 μm). When the loading velocity was further increased to 226 $\mu\text{m/s}$ (Figure 3.9(c)), the electronic measurement was further lagged. It should be mentioned that the deviation from the ideally linear displacement, as predicted by Eq. (3-7) and shown in Figure 3.9(c), was not captured by the electronic measurement, again due to the limitation in bandwidth (the smaller sinusoidal deviation frequency predicted is 11,490 Hz which is much larger than the readout bandwidth). The sinusoidal deviation appears to have only one frequency rather than two as predicted by Eq. (3-7). This is because the amplitude of the larger natural frequency is tiny compared that of the smaller natural frequency. For example, when the loading velocity is 226 $\mu\text{m/s}$, the calculated amplitude is 3.2 nm for the lower natural frequency, while 0.01 nm for the larger natural frequency.

The dynamic response under the ramping actuation force was also studied in air. The optical method was used to measure the displacement d_B . Figure 3.9(d) to (f) shows the experimentally measured and analytically predicted displacement d_B with the loading velocity of 226 nm/s, 226 $\mu\text{m/s}$ and 2.26 mm/s. The corresponding loading time was 1 s, 1 ms and 0.1 ms. The high-speed camera frame rate used was 50, 16,000 and 95,000 fps with the corresponding images under these frame rates shown in the inset of Figure 3.9(d) to (f), respectively. As

mentioned earlier, the field of view was reduced to compensate the increasing frame rate. The measured displacement agreed well with analytical model. Figure 3.9(e) shows optically measured displacement still increased linearly with time with no obvious lag when the loading velocity was $226 \mu\text{m/s}$, which on the other hand proved that the significant lag in Figure 3.9(c) is due to the bandwidth limitation. When the loading speed increased to 2.26 mm/s , measured displacement was not linear. Instead it was the combination of linear displacement and deviation as explained in Section 3.3.2. In this case, constant strain rate was not available. In the following Section 3.5.2, the maximum strain rate the device can attain in both vacuum and air will be discussed.

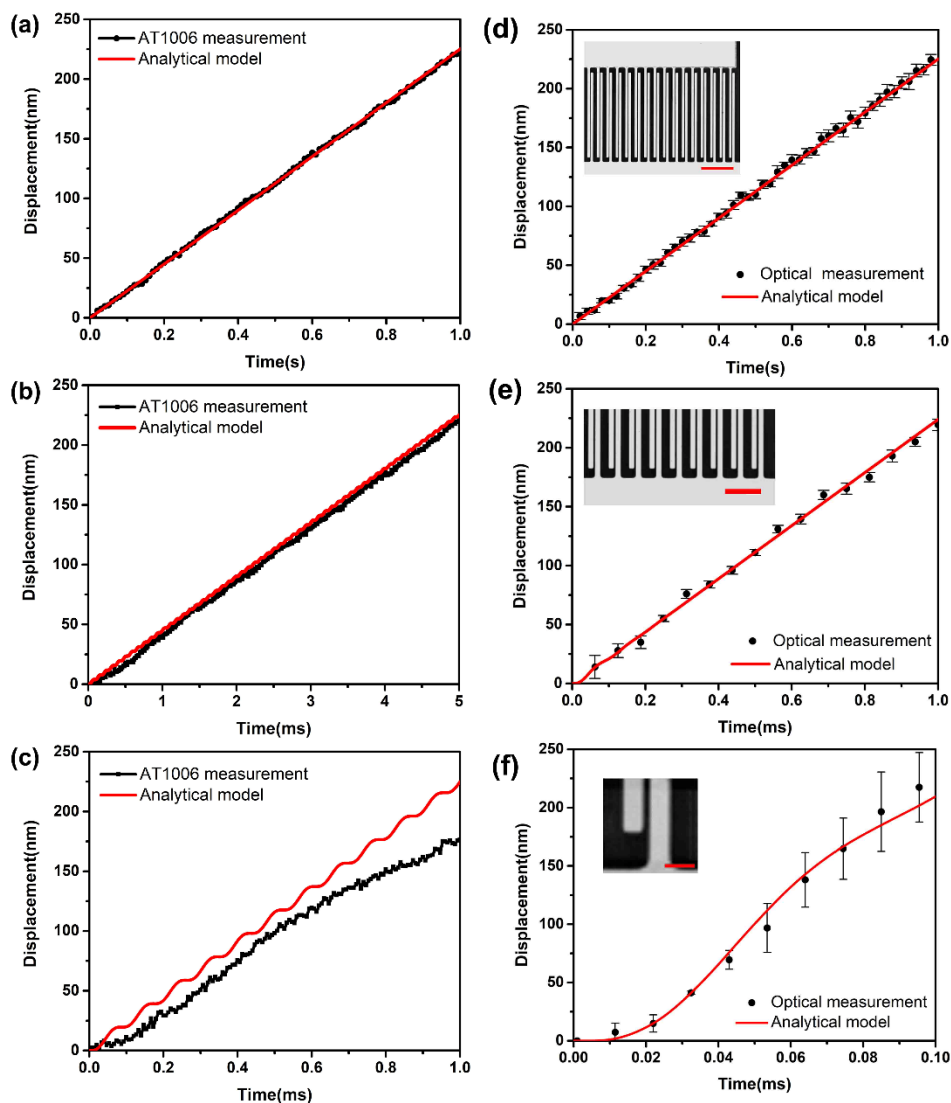


Figure 3.9. Comparison of displacement measured from AT1006 and model in vacuum when loading time is (a) 1s, (b) 5ms and (c) 1ms. Comparison of displacement from dynamic model and optically measured displacement in air when loading time is (d) 1 s, (e) 1 ms and (f) 0.1 ms. The frame rates are 50 fps, 16,000 fps, 95,000 fps, respectively. Insets are the corresponding images which were taken under same microscope magnification. Scale bars are 100 μm , 50 μm and 10 μm respectively. Higher frame rate is associated with low field of view.

3.5. Discussion

3.5.1. Damping coefficients

The damping coefficients obtained through the experiments in Section 3.4.2 are compared with those calculated based on the theoretical models. For this device, the damping force comes from the comb-drive actuator and parallel plates sensors. For the comb-drive actuator, a laterally driven structure, viscous drag of ambient fluid is the dominant damping source; while for the parallel plates sensor, squeeze film damping is the major source of energy dissipation⁹⁴. Both damping mechanisms have been studied extensively and here we will briefly discuss them in the context of our device.

Damping coefficient for a comb-drive actuator can be expressed as⁹⁵

$$c_{cd} = \mu \left(\frac{A_{eff}}{d_s} + \frac{A_{eff}}{\delta} + \frac{A_s}{g} + 10.7L \right) \quad (3-9)$$

where μ is the viscosity of air, A_{eff} is the effective plate area including the areas of the shuttle, fingers and beams, A_s is the side area of the actuator, d_s is the distance between the actuator and substrate, δ is the effective decay distance, and L is the characteristic dimension of the moving structure that can be taken as half the width of the shuttle.

Compared with the comb-drive actuator, it is more complicated to determine damping coefficient of the parallel-plate sensor. Depending on the frequency of oscillation of the plate, the squeeze film damping force can be either elastic force proportional to displacement of the moving plate or viscous force proportional to velocity of the moving plate⁹⁶

$$\omega_c = \frac{\pi^2 g_1^2 p_a}{12 \mu w^2} \quad (3-10)$$

where p_a is the atmosphere pressure and w is the width of the plate. For the device reported here, this cutoff frequency is calculated to be 3.7 MHz. Since the device is operated far below this frequency, the viscous damping force dominates while elastic damping force is negligible. In this

situation, the damping coefficient for parallel plates can be expressed as⁹⁶

$$c_{pp} = \frac{\mu L W^3}{g_1^3} \quad (3-11)$$

where L is length of the plate.

Based on these theoretical models, the calculated damping coefficients in air are $c_A = 3.04 \times 10^{-4}$ kg/s (comb-drive actuator) and $c_B = 2.98 \times 10^{-4}$ kg/s (parallel-plate sensor), close to the experimentally obtained values.

3.5.2. Strain rate

In this section, the maximum strain-rate the present device can attain is discussed. For this microscopic tensile testing device, it can be seen from Eqs. (3-7) and (3-8) that under a ramping actuation force, the strain rate will not be a constant either in vacuum or in air because displacement of Sensor B is not absolutely linear. However, high strain-rate testing does not necessarily require an absolute constant strain rate. For example, commercial macroscopic high rate testing systems usually use hydraulic actuators to reach strain rate up to 1000 s^{-1} . Open-loop control is used since the actuator moves at such a high velocity that real-time close-loop control is not as effective, which leads to displacement that cannot be absolutely linear as noted previously⁹⁷⁻⁹⁹. Therefore it is reasonable to carry out high rate testing with approximately constant strain rate.

For the microscopic tensile testing device presented here, its displacement can be treated to be linear as long as the deviation is negligible. For example, as shown in Figures 3.8(a),(b),(d) and (e), the measured displacement almost increased linearly with time and so did the modelled displacement. To assess the magnitude of the deviation, which should be done with respect to travel range, a normalized term “deviation ratio” is defined as the maximum displacement deviation during the loading process divided by the travel range. The maximum strain-rate the device is able

to attain can then be obtained by setting an upper bound of this deviation ratio (or allowable deviation ratio). Figure 3.10(a) shows the maximum strain rate as a function of the allowable deviation ratio and the travel range in vacuum, calculated based on Eq. (3-7). The larger the travel range and the deviation ratio, the larger the maximum strain rate. An approximate equation of this relationship can be obtained considering that for the current device a_2 in Eq. (3-7) is negligible compared to a_1 . With this approximation, the maximum displacement deviation is $a_1 p$, which is the product of the allowable deviation ratio and the travel range by definition. Given the allowable deviation ratio and the travel range, the maximum strain rate can be expressed as

$$\dot{\epsilon}_{max} = \frac{p_{max}}{l_0 k_{SB}} = \frac{(allowable\ deviation\ ratio) \times (travel\ range)}{a_1 l_0 k_{SB}} \quad (3-12)$$

Figure 3.10(b) shows the maximum strain rate as a function of the allowable deviation ratio and the travel range in air, based on Eq. (3-8). An approximate equation of this relationship can be provided as

$$\dot{\epsilon}_{max} = \frac{p_{max}}{l_0 k_{SB}} = \frac{(allowable\ deviation\ ratio) \times (travel\ range)}{(a_3 + a_4) l_0 k_{SB}} \quad (3-13)$$

For a typical nanowire with gauge length of 2 μm and fracture strain of 3 %, the travel range is 60 nm. If the allowable deviation ratio is 1 %, the maximum strain rate is 23.6 s^{-1} in vacuum. If the allowable deviation ratio is 10 %, then maximum strain rate is 236 s^{-1} as the maximum strain rate is proportional to the allowable deviation ratio. In air, the maximum strain rate is 20.8 s^{-1} and 208 s^{-1} with 1 % and 10% allowable deviation ratio, respectively. For the measured displacement in air as shown in Figure 3.9(f), the deviation ratio is about 15 % (travel range ~ 200 nm). Note that the deviation ratio is defined based on the deviation from the linear displacement in theory (i.e. $\frac{pt}{k_{SB}}$ in Eq. (3-7)), which is an overestimate if compared with a fitting line that would also give a constant strain rate. Hence it is appropriate to conclude that the

attainable strain rate is on the order of 200 s^{-1} both in vacuum and in air.

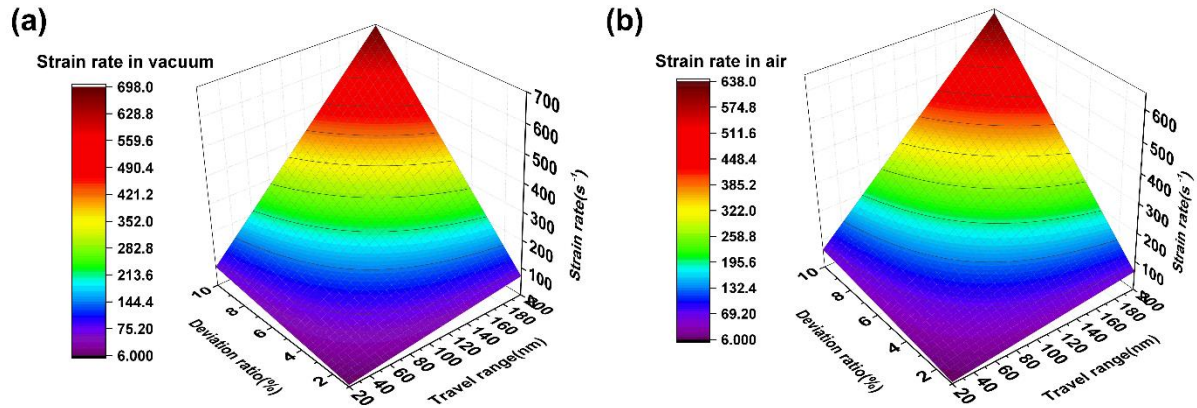


Figure 3.10. (a) Relationship of maximum strain rate the device can attain versus deviation ratio and travel range in vacuum. (b) Relationship of maximum strain rate vs deviation ratio and travel range in air.

3.5.3. Force measurement

The capacitive readout AT1006 will be used to obtain force and elongation of gold nanowires in next section because it is able to measure both sensors' displacements in SEM at the same time. As mentioned in Section 2, when the device is operated for quasi-static testing, force in a specimen equals force in the load cell, which can be calculated given displacements of the two sensors. For high strain rate dynamic testing, force in a specimen equals force in the load cell minus the damping force. The damping force inside SEM environment with a pressure of 5×10^{-6} torr was hence studied. In rarefied air, the squeeze film air damping coefficient can be calculated using Veijola's model¹⁰⁰ that replaces the viscosity in Eq. 13 with an "effective" one μ_{eff} ,

$$\mu_{eff} = \frac{\mu}{1 + 9.658K_n^{1.159}} \quad (3-14)$$

where K_n is Knudsen number that is defined as mean free path of air molecules divided by gap distance of the parallel plate. The damping coefficient calculated in this case is on the order of 10^{-7}

¹² Kg/s. The damping force is on the order of 10^{-15} N, even for the largest velocity (44 $\mu\text{m/s}$) that can be measured by AT1006. Therefore the damping force inside SEM is negligible and force of a specimen can still be calculated based on the load cell force.

In air, the damping coefficient is on the order of 10^{-4} Kg/s. With 100 $\mu\text{m/s}$ velocity or 50 s^{-1} strain rate, the damping force is on the order of 10 nN, which can still be neglected for testing specimens like nanowires and nanotubes.

3.6. High-Strain-Rate Testing of Gold Nanowires

To demonstrate of its capability of high strain-rate nanomechanical tensile testing, the device was used to test two gold nanowires at strain rates of 10^{-5} s^{-1} and 10 s^{-1} . The gold nanowires, $\langle 110 \rangle$ oriented, were synthesized by physical vapor deposition exhibiting high crystalline quality¹⁰¹. The tests were conducted inside SEM and AT1006 was used to measure displacements of the two sensors (A and B), from which the stress and strain were calculated. Nanowires were picked up from a Si substrate using a nanomanipulator and clamped on the device by e-beam induced deposition of Pt. The diameters of the two nanowires were 144 nm and 153 nm, respectively. Both the nanomanipulation and the tensile testing were performed inside a SEM-FIB dual beam (FEI Quanta 3D FEG).

Stress-strain curves for the two tested nanowires are shown in Figure 3.11. Young's moduli measured from both tests are around 75 GPa, which is close to the bulk value. The gold nanowire tested at 10^{-5} s^{-1} exhibited a fracture strength of 2.1 GPa and a fracture strain of 2.8 %, indicating a brittle fracture. By contrast, the one tested at 10 s^{-1} showed a higher yield strength of 3.7 GPa and a large ductility with the fracture strain of 13.5 %. Note a sudden stress drop was also captured during high-speed loading of the nanowire. This softening behavior is attributed to the nucleation

and propagation of leading partial dislocations from the nanowire surface, which has been reported in previous MD simulations of FCC metal nanowires¹⁰². Figure 3.12 shows the two nanowires before and after testing. By comparing the SEM images, we found that the nanowire tested at high strain rate shows a clear decrease in diameter across the gage length while the one tested at low strain rate did not show much variation in diameter. This observation is similar to the results by Ramachandramoorthy⁶⁶ and Tao¹⁰³, where the authors found that the silver nanowires show a brittle-to-ductile transition with increasing strain rate.

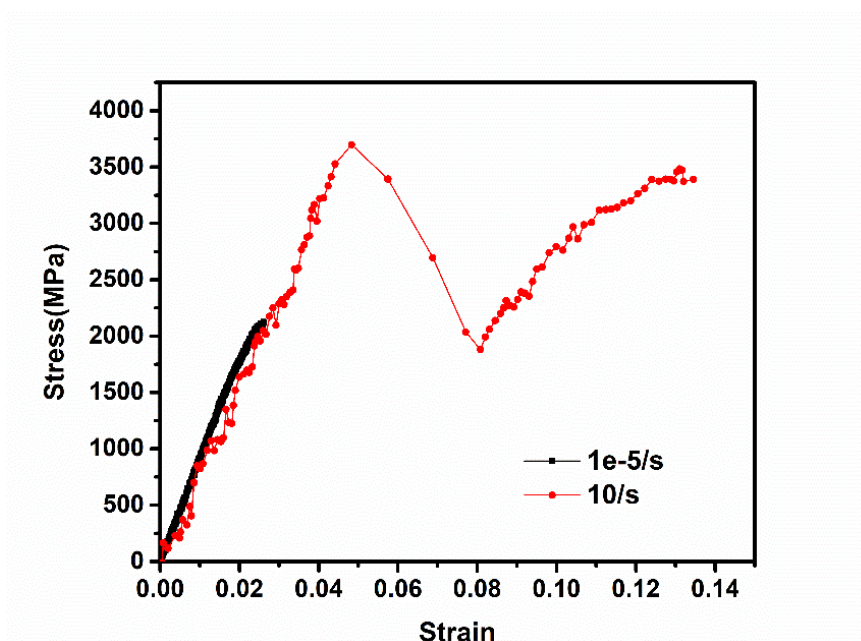


Figure 3.11. Stress-strain curves for two Au nanowires tested at different strain-rates.

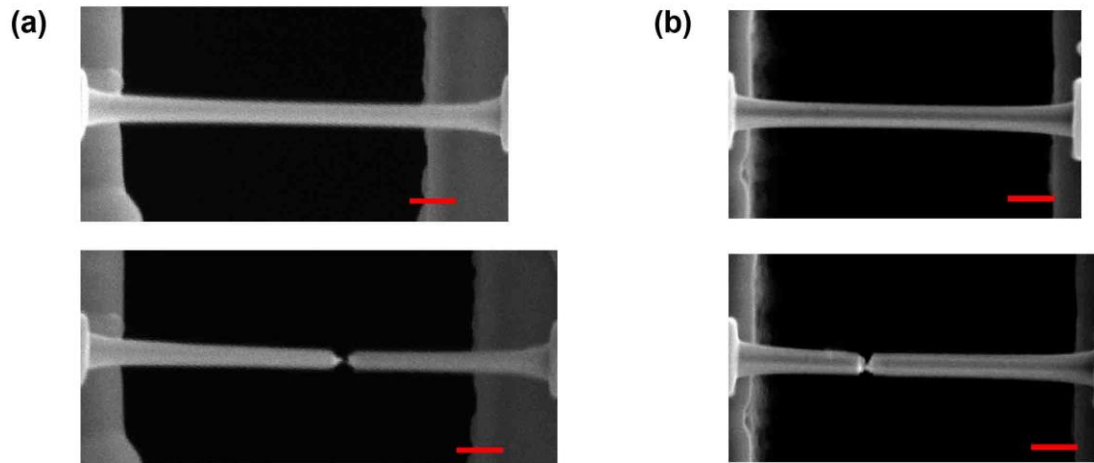


Figure 3.12. SEM images of the tested Au nanowires before and after testing. (a) 10/s. (b) 1×10^{-5} /s. Scale bar: 300 nm.

3.7. Conclusions

In this chapter, we systematically investigated the dynamic response of a MEMS-based nanomechanical testing device in air and in vacuum. A dynamic model of the device was built and device frequency response and dynamic response under ramping actuation force in both air and vacuum were simulated. Both capacitive readout and high-speed optical imaging were used to measure the displacements. The experimental results showed good agreement with the modeling results. The maximum strain rate the device can attain was found to be about 200 s^{-1} . However, the capacitive readout used can only measure strain rate up to 22 s^{-1} (gauge length $2 \text{ }\mu\text{m}$) due to its limited bandwidth, which is nevertheless an order of magnitude higher than the highest strain rate (2 s^{-1}) reported using an electronic sensor. We demonstrated the device's capability by testing gold nanowires at two strain rates of 10^{-5} s^{-1} and 10 s^{-1} . It was found that increasing strain rate leads to higher yield strength and larger ductility.

CHAPTER 4:

A piezoresistive displacement sensor for high frequency sensing in nanomechanical tensile testing applications

4.1. Introduction

As introduced in chapter 1, many different microelectromechanical systems (MEMS) devices have been designed and most of them integrate an on-chip displacement sensor. Displacement sensing is of vital importance for mechanical characterization of nanomaterials which proposes strict requirements on these displacement sensors. The displacement sensors should have a small footprint and should be compatible with existing microfabrication processes to reduce production cost, more importantly, they should satisfy the noise, dynamic range and bandwidth requirements of the device.

Different sensing mechanisms such as capacitive, electrothermal and piezoresistive have been successfully implemented in a variety of MEMS devices. Capacitive sensing is widely used to detect displacement of MEMS devices with a high resolution. Implementation of this technique is often compatible with standard microfabrication processes. However, capacitive sensors occupy a large fraction of the chip and may need complicated readout circuits to detect small capacitance variations. For the differential capacitive sensor used in last two chapters, it is the complicated readout that limits the bandwidth and prevents the sensor to be used in high frequency sensing applications such as high strain rate testing. Electrothermal sensing is an alternative technology for on-chip position measurement in MEMS^{50, 58}. In comparison with the capacitive sensors, electrothermal sensors occupy a small foot print, and require a relatively simple readout circuit. However, they are not suitable to be used in vacuum conditions since they heavily rely on heat

dissipation through air. Piezoresistivity of silicon has also been exploited in a variety of displacement sensing applications such as in AFM^{104, 105} and pressure sensors^{106, 107}, but very few piezoresistive sensors are integrated in MEMS devices for nanomechanical testing.

Piezoresistive sensing is based on the variation of the electrical conductivity of materials such as silicon when mechanically stressed. Wide sensing bandwidth is one of its advantages. Here in this work we explore using a silicon based piezoresistive sensor to measure high frequency displacement in order to compensate the bandwidth limitation of the capacitive displacement measurement mentioned in last chapter. Static behavior of the piezoresistive sensor was first investigate, followed by dynamic characterization. The resolution of the sensor was also discussed.

4.2. Device description

The device is again fabricated using the SOIMUMPS process. Figure 4.1(a) shows the overall structure of the device. The device consists of a piezoresistive displacement sensor and an on-chip comb-drive actuator. The piezoresistive sensor used here is actually a z-shaped thermal actuator as introduced in chapter 1, since the surface of the silicon layer of the whole structure is diffusion doped by depositing a phosphosilicate glass (PSG) layer and annealing at 1050°C for 1 hour in Argon, the structure also exhibits good piezoresistive properties whose resistance changes under deformation, hence it can be used as a sensor at the same time. Ouyang⁵¹ has once conducted a study on using the Z-shaped actuator as a piezoresistive sensor simultaneously where a single Z-shaped piezoresistor was investigated. However, the sensor made of a single piezoresistor requires a very stable environment in order to achieve reliable sensing function. This is because piezoresistive sensor works based on detecting resistance change caused by stress or strain, while resistance may also be changed due to some environmental factors, such as temperature, which

will influence the accuracy of the sensor. Hence in this study, in addition to the single z-shaped actuator acting as a sensor, three identical Z-shaped actuators were added as reference structures constructing a Wheatstone bridge to eliminate the environmental influence and achieve extreme accurate measurement. Figure 4.1(b) shows the electrical schematic of the Wheatstone bridge.

A comb-drive actuator is co-fabricated with the sensor with the purpose of providing in plane force to deform the displacement sensor in order to study its piezoresistive property during the calibration process and on the other side it can be used to stretch a specimen during nanomechanical tensile testing using the sensor in future. Comb-drive actuator is chosen because it operates on electrostatic force with no heat generation which is critical for piezoresistive sensors. Since the sensor and actuator require two voltage sources to provide the excitation voltage separately, in order to avoid electrical interference between the two sources, the sensor and actuator are electrically isolated through a gap in between. This gap also mechanically isolates the actuator and sensor, to provide the necessary mechanical connection, a 3M epoxy adhesive (DP100 Plus Clear) was used to glue the two parts together as shown in the insets of Figure 4.1(a). The gluing process was conducted under an optical microscope (NIKON LV150) with the help of a 3-axis nanopositioning arm (ALESSI). A tungsten probe (Micromanipulator, Model 7X) with tip diameter around 300 nm was mounted on the arm and dipped into epoxy to pick up a small amount of epoxy used to glue the two parts. The epoxy chosen has a high stiffness (1850 psi) which can be considered as a rigid connector. Also it has a large volume resistivity (6.7×10^{11} ohm•cm) which remains the electrical isolation of the actuator and sensor.

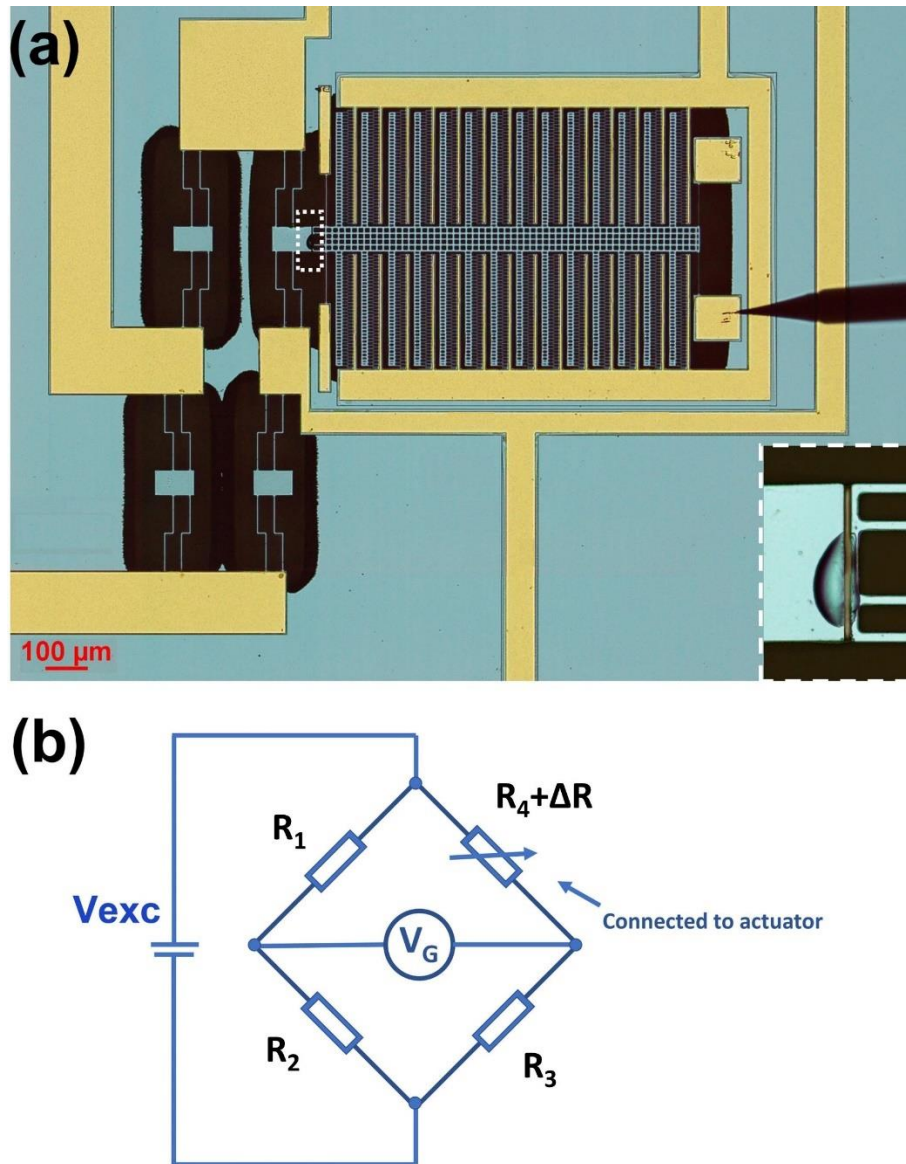


Figure 4.1(a) Optical image of the piezoresistive sensor and comb-drive actuator. (b) Electrical schematic of the wheatstone bridge constructed of the piezoresistor and three reference resistors.

4.3. Displacement Sensor Characterization

4.3.1. Static Calibration

To characterize the displacement sensor, a gradually increasing voltage with step 2V is applied to the comb-drive actuator which deforms the piezoresistor connected to it changing its

resistance, the displacement of the sensor under each actuation voltage step is measured from high magnification images, meantime, the output voltage V_G is recorded using a 16-bit DAQ (NI USB 6211) while an excitation voltage $V_{exc} = 3V$ is applied to the Wheatstone bridge, the output voltage corresponding to each actuation voltage step is then averaged. The characterization result is shown in Figure 4.2. The relationship between actuation voltage and measured displacement is shown in Figure 4.2(a). It follows a quadratic trend which is verified by the linear relationship between displacement and square of actuation voltage as shown in Figure 4.2(b). The quadratic nature matches with our expectation since the actuation force is proportional to the actuation voltage square for comb-drive actuator as indicated in Eq. (2-1). Figure 4.2(c) plots the output voltage versus actuation voltage, as can be seen, output voltage increases with increasing actuation voltage. Based on Figure 4.2(b) and (c), the mapping relationship between displacement and output voltage can be obtain which is shown in Figure 4.4 (d). With this relationship, the sensor's displacement can be induced from output voltage from the Wheatstone bridge. The relationship shows a linear trend with $R^2=0.993$ for the fitted regression line.

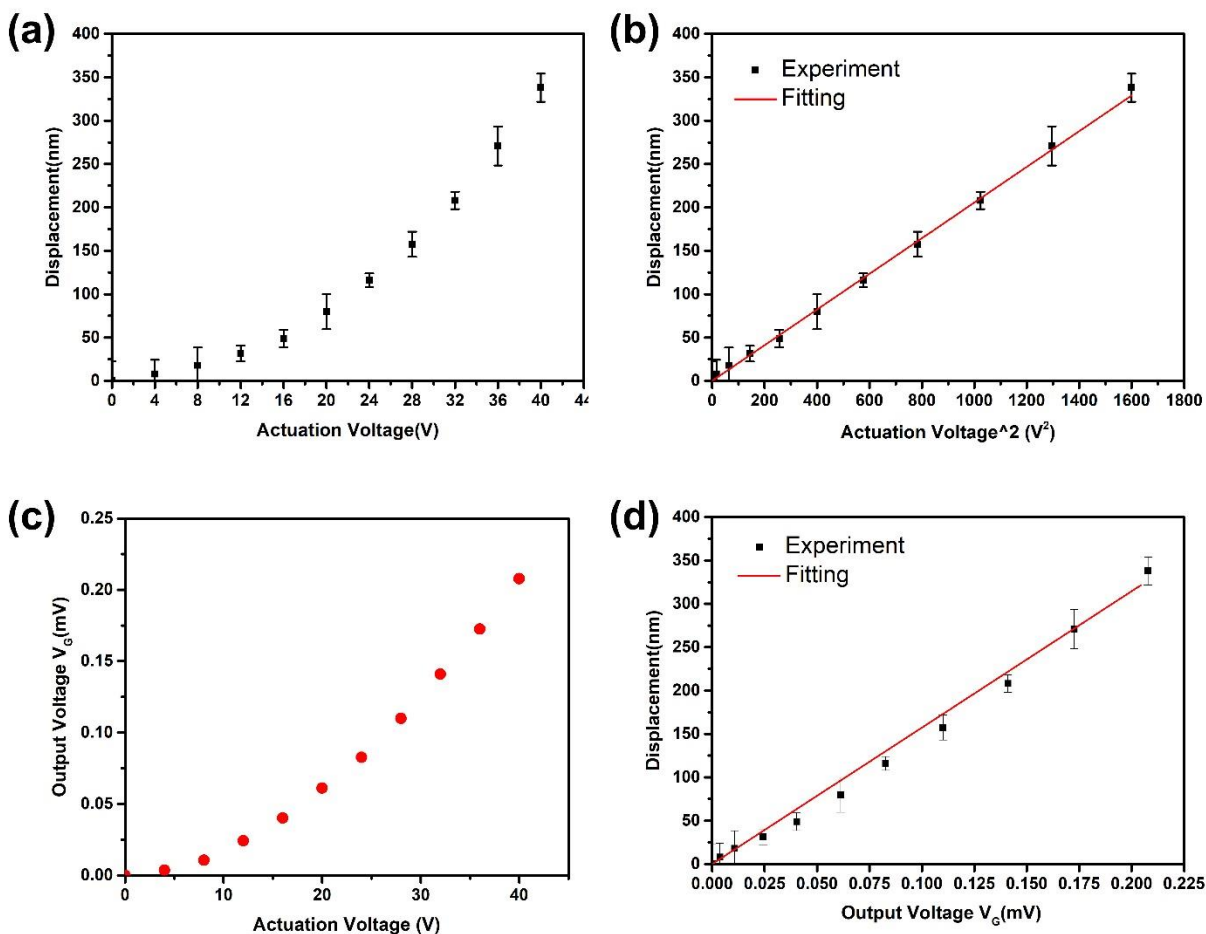


Figure 4.2 Calibrated relationship between (a) displacement vs actuation voltage (b) displacement vs actuation voltage square (c) output voltage vs actuation voltage (d) displacement vs output voltage.

The linear relationship between displacement and output voltage can be explained through two steps. The first step is to prove that there is a linear relationship between displacement and resistance change (ΔR) of the piezoresistor. Typically, piezoresistive sensors are made through selectively doping on a small area whose shape and orientation are specially designed so that the piezoresistor will have a simple stress profile during operation, for example piezoresistive pressure sensor deforms out of plane and undergoes simple tensile stress when pressed, in this case the change in resistance of the sensor can be predicted analytically. However, the sensor in this

work sustains complex stress profile during in-plane deformation which makes calculating stress or strain induced resistance change impossible. Finite element analysis can be used to estimate the resistance change through multiphysics simulation. Ouyang⁵¹ has done such a simulation on a single Z-shaped piezoresistive sensor. The simulation result exhibited a linear relationship between displacement of Z-shaped sensor and its resistance change. Experiment was also conducted whose results match with the simulation. The Z-shaped sensor used in Ouyang's work has the same in-plane dimensions with the one used in this work but different device thicknesses. However, thickness won't influence the linear relationship. This is because for in-plane deformation, silicon along the thickness has the same stress status and the hence same change of resistivity. On the other hand, the total resistance of the silicon device mainly attributes to the more conductive top thin surface layer into which impurity is diffused. Hence it is reasonable to say for the Z-shaped sensor in this work, its resistance change is linear with displacement.

The second step is to prove resistance change has a linear relationship with output voltage of Wheatstone bridge. The output voltage V_G for Wheatstone bridge can be expressed as:

$$V_G = \left(\frac{R_2}{R_1+R_2} - \frac{R_3}{R_3+R_4+\Delta R} \right) V_{exc} \quad (4-1)$$

The derivative of output voltage with resistance change is:

$$\frac{d(V_G)}{d(\Delta R)} = \frac{R_3 V_{exc}}{(R_3+R_4+\Delta R)^2} \quad (4-2)$$

The derivative can be approximated as a constant when resistance change ΔR is small compared with $R_3 + R_4$ which will be verified through the following experimental results. The initial resistance of the four identical resistors can be measured accurately using multimeter, the results shows a small discrepancy between each other with $R_1 = 384$ ohm, $R_2 = 381$ ohm, $R_3 = 384$ ohm, $R_4 = 380$ ohm separately. When the 3V excitation voltage is applied, the resistance will increase due to Joule heating. Since multimeter can't be used to measure resistance when the resistor is

connected to a power supply, the resistance of the piezoresistors within the excited Wheatstone bridge was estimated by measuring the I-V curve of a single Z-shaped piezoresistor fabricated on the same chip with the Wheatstone bridge having the same dimensions. The calculated resistance versus voltage relationship based on I-V curve is shown in Figure 4.3(a). When 3V is applied to the bridge, each resistor within the bridge sustains 1.5V approximately. Hence the estimated resistance of a piezoresistor in a Wheatstone bridge excited by 3V is 394 ohm. Here for simplification the resistance of the four resistors are considered having the same value despite their small discrepancy, then the relationship between output voltage V_G and resistance change ΔR can be estimated by Eq. (4-1) and plotted as shown in Figure 4.3(b). As can be seen, V_G increases linearly with ΔR because resistance change is small. For our experiment result shown in Figure 4.2(c), the maximum output voltage is 0.21 mV which corresponds to an estimated resistance change of 0.11 ohm.

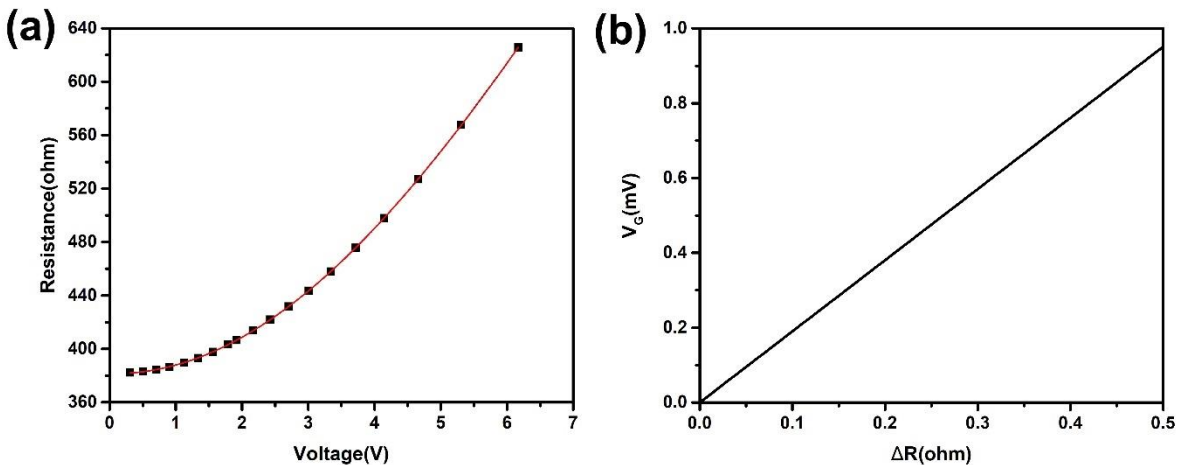


Figure 4.3 (a) Applied voltage to a single Z-shaped resistor and its resistance. (b) Relationship between output voltage V_G and resistance change ΔR calculated based on Eq. (4-1).

With the two linear relationships verified, it is reasonable to linearly fit the displacement – output voltage relationship and calculate the sensitivity of the sensor (S , unit: mV/nm) based on it.

4.3.2. Dynamic characterization

The displacement sensor is expected to be used for high strain rate testing or high frequency sensing, hence dynamic characterization is necessary. The characterization is conducted by studying its frequency response. To study the frequency response, an AC voltage is applied to the comb-drive actuator while the frequency is gradually increased. The output voltage was initially measured using the DAQ. Figure 4.4(a) shows the output voltage when the AC voltage frequency is 50 Hz, the measured output voltage frequency is 100 Hz because force is proportional to the 2nd order power of voltage (Eq. (2-1)). As can be seen, the noise is quite large compared with the signal. In order to obtain the true amplitude of the alternating output voltage signal, a lock-in amplifier (SR830) was used which is able to extract a tiny signal from an extremely noisy environment. A reference signal which must have the same frequency with signal to be detected is needed in order for the lock-in amplifier to work. Since there is a factor of 2 between frequency of output voltage which is the signal to be detected and frequency of the actuation voltage, the actuation voltage can't be directly used as the reference signal. Instead a sinusoidal voltage with 2 times the frequency of actuation voltage is connected to the reference input. The amplitude of output voltage at different frequency measured in this way was normalized and plotted versus frequency. Figure 4.4(b) plots the frequency response of the system. The resonance frequency is around 45 kHz which is similar to the simulation results predicting the first in-plane resonance frequency to be 47 kHz. The frequency response study proves that this displacement sensor is able to measure displacement accurately at frequency up to 80 kHz (for safety concern, the frequency didn't go even further, this is because the comb-drive actuator essentially is a capacitor, at high frequency, the impedance is small and current is large which might burn the actuator), hence it is able to be used in high frequency sensing applications in nanomechanical testing. Compared with capacitive

displacement sensor used in previous chapters, which has a low bandwidth due to the low capacitance to voltage conversion speed of the readout, the high bandwidth of this sensor should attribute to the piezoresistive sensing mechanism which converts displacement (or strain) directly to resistivity change instantly.

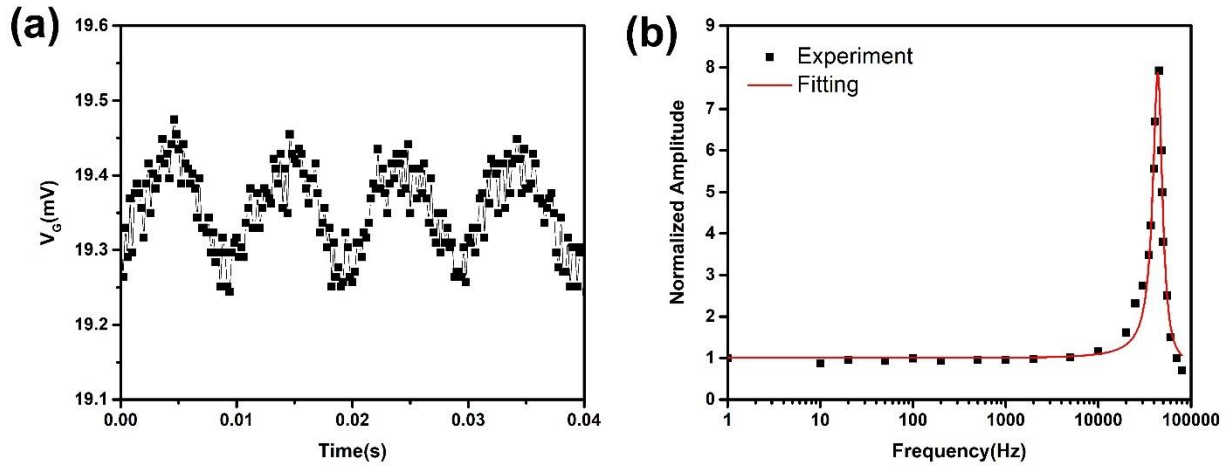


Figure 4.4 (a) Measured output voltage with frequency 100 Hz. (b) Relationship between normalized output voltage amplitude versus frequency, i.e. frequency response.

After studying the frequency response, the next step should be exploring the sensor's response to a ramping input to study its high strain rate testing capability. However, since the noise is large as shown in Figure 4.4(a) which will limit the resolution of the sensor, we will first explore the sensor's resolution before studying the dynamic response under ramping input.

4.3.3. Sensor resolution

Sensor resolution is defined as the smallest signal that can be reliably detected. The minimum detectable signal without averaging multiple trials is determined by noise level. Hence resolution of the displacement sensor can be defined by

$$\text{Resolution} = \frac{V_{\text{noise}}}{S} \quad (4-3)$$

where S is the voltage-referred sensitivity with respect to displacement. V_{noise} is a term to describe the amplitude of the noise voltage, in this work V_{noise} is defined as

$$V_{noise} = 6 \times V_{RMS} \quad (4-4)$$

V_{RMS} is the root mean square of a noise signal. Note that since the mean value of noise signal is zero, the RMS value is equal to the standard deviation (σ) of the noise signal. The factor 6 accounts for the $\pm 3\sigma$ interval in which noise will fall with 99.7% possibility.

As can be seen from Figure 4.4(a), without any signal conditioning circuitry, the measured output voltage is quite noisy which undermines the sensor's resolution. To improve the resolution, either the noise needs to be decreased, or the sensitivity needs to be increased. We will make a discussion of both the methods.

For piezoresistive sensor, noise can result from intrinsic and extrinsic sources. Intrinsic sources depend on the resistor itself and the signal conditioning circuitry. Extrinsic sources are associated with the specific measurement environment, such as inductive or capacitive line pickup, carrier injection due to high intensity light illumination, and variation in the ambient temperature or humidity. The intrinsic noise coming from the resistor itself can't be eliminated and it sets the fundamental lower limit of piezoresistive displacement sensor resolution. The dominant random electrical noise sources of this type are Johnson (thermal) noise and 1/f (flicker) noise. Johnson noise is universal to electrical resistors¹⁰⁸. It is caused by the thermal agitation of charge carriers within a conductor. The main feature of Johnson noise is its power spectrum density is the same for any frequency components. The power spectrum density of and RMS value of Johnson noise can be calculated from

$$P_j = 4kTR \quad (4-5)$$

$$V_{RMS} = \sqrt{4kTR(\Delta f)} \quad (4-6)$$

where k is Boltzmann's constant, T is the average piezoresistor temperature and R is the electrical resistance of the piezoresistor, Δf is the measurement bandwidth. Thus, in order to minimize Johnson noise, the resistance, temperature and measurement bandwidth should be minimized. In this work, we chose to use a low pass filter to reduce the measurement bandwidth as will be introduced later.

1/f noise, as its name implies, has a power spectrum density inversely proportional to frequency. The origins of 1/f noise are still not fully understood and remain an active topic of research¹⁰⁹⁻¹¹¹. Based on fitting of observed data, Hooge¹⁰⁹ proposed an empirical model to predict the power spectrum density,

$$P_{1/f} = \frac{\alpha V_b^2}{Nf} \quad (4-7)$$

where f , N and V_b are frequency, total number of carriers in the resistor volume, and bias voltage across the resistor, respectively. A non-dimensional fitting parameter, α , is ascribed to the "quality of the lattice" and typically ranges from 10^{-3} down to 10^{-7} ¹¹²⁻¹¹⁴.

The noise power spectrum density from the output of Wheatstone bridge can be experimentally measured using the signal conditional circuit shown in Figure 4.5. The output of Wheatstone bridge was first amplified through an instrumentation amplifier, the one we used in this work is AD620. By using proper resistors and capacitors, the amplifier was adjusted to have an anti-aliasing low pass filter with a cutoff frequency of 1500 Hz and the gain G was adjusted to be 100. The amplified signal was then sampled by an analog to digital converter with a sampling rate of 5000Hz (larger than two times the cutoff frequency) which was then analyzed using FFT to obtain the amplitude versus frequency relationship from which the power spectrum density can be calculated.

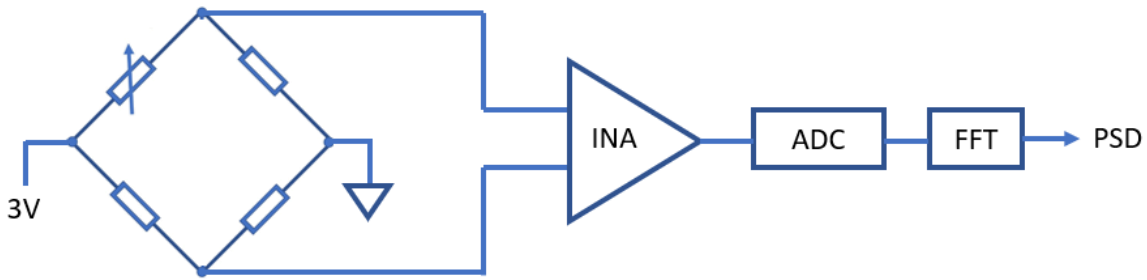


Figure 4.5. Signal conditioning circuit to measure noise spectrum density of Wheatstone bridge.

It is to be noted that the power spectrum density measured using this method is actually the sum of PSD of the Wheatstone bridge output and the amplifier which can be estimated using the equation shown below:

$$P_j = 4kTR + e_{ni}^2 + \left(\frac{e_{no}}{G}\right)^2 + 2\left(\frac{i_n R}{2}\right)^2 \quad (4-8)$$

where e_{ni} , e_{no} , i_n are the input voltage noise, output voltage noise and current noise of the instrumentation amplifier, respectively.

The first term corresponds to the intrinsic Johnson noise of the Wheatstone bridge based on Eq. (4-5). Among the two intrinsic noise sources, the dominant one for high frequency application is Johnson noise since power attenuates rapidly for $1/f$ noise as frequency increase. Hence, we can neglect the $1/f$ noise and consider only Johnson noise to find out the fundamental lower limit of noise. Note that Eq. (4-5) holds for a single resistor, a Wheatstone bridge contains four resistors. Assuming that the bridge is balanced and all four resistors have same resistance R , then the impedance looking out from each output terminal is $R/2$ and the Johnson noise power spectrum density due to the resistors will be $2kTR$ at each terminal. The noise power of uncorrelated sources adds linearly, so the total Johnson noise of the Wheatstone bridge is $4kTR$. The resistance R in the equation can be estimated from Figure 4.3(a), averaged temperature can be

estimated from multiphysics simulation using Ansys. The calculated Johnson power spectrum density for a 394-ohm resistor (z-shaped piezoresistor under 1.5V voltage) is $7.6 \times 10^{-18} \text{ V}^2/\text{Hz}$.

The sum of last three terms in Eq. (4-8) corresponds to noise introduced by the amplifier. For the amplifier we used, AD620, the values of the noise sources are $e_{ni} = 13 \text{ nV}/\sqrt{\text{Hz}}$, $e_{no} = 100 \text{ nV}/\sqrt{\text{Hz}}$, $i_n = 100 \text{ fA}/\sqrt{\text{Hz}}$, which gives us the value of noise PSD caused by amplifier $1.7 \times 10^{-16} \text{ V}^2/\text{Hz}$. It is about two orders large than the Johnson noise of piezoresistor.

The measured actual noise spectrum density is shown in Figure 4.6 with an averaged noise PSD value as $3.81 \times 10^{-11} \text{ V}^2/\text{Hz}$. Note this value is obtained with the gain $G = 100$ considered, the noise power spectrum density without being amplified is $3.81 \times 10^{-15} \text{ V}^2/\text{Hz}$ which is still around 10 times larger than the calculated value using Eq. (4-8). This is probably because in the experiment extrinsic noise source was introduced which was not considered in the analytical equation. An evidence of this assumption is that the power spectrum density shows an obvious peak at 60 Hz as shown in Figure 4.6(b) which is due to the interference of electromagnetic wave around the testing instrument. From Figure 4.6(b) which shows the noise power spectrum density within the range of 0 to 100 Hz, 1/f noise can be clearly identified with 1/f corner frequency around 10 Hz.

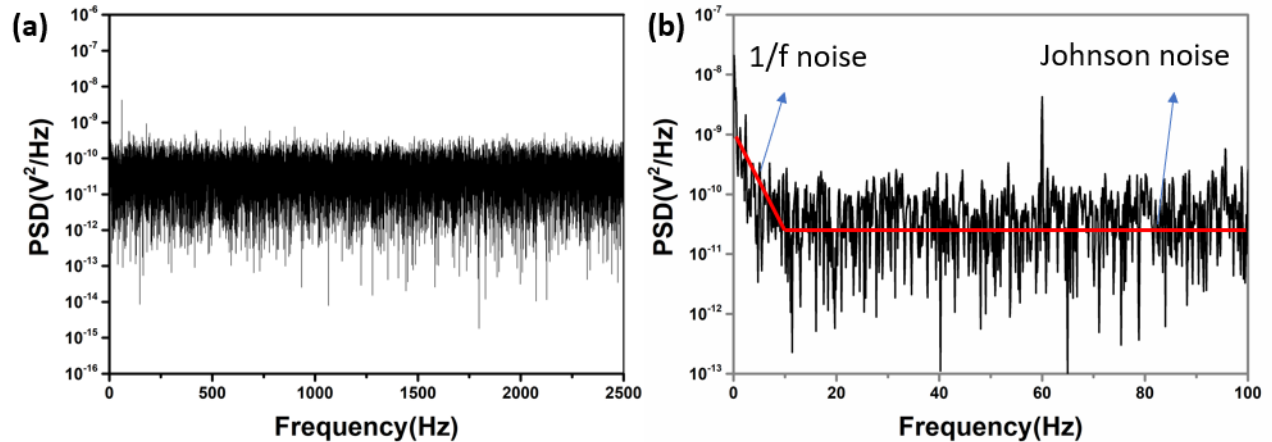


Figure 4.6. (a). Measure noise power spectrum density within range 0 to 2500 Hz. (b) Noise PSD from 0 to 100 Hz from which 1/f noise and Johnson noise can be clearly identified.

Based on the analytical and experimental results, two methods can be proposed to further mitigate the noise in future in addition to reducing the measurement bandwidth used in this work. The first is to use a faraday cage to shield out the extrinsic noise. The second method is to use an ultralow noise instrumentation amplifier to replace the AD620. A good candidate is AD8429 which has a noise input voltage with only $1nV/\sqrt{Hz}$, more than 10 times smaller than AD620. The noise power spectrum density from the amplifier will be comparable with PSD from piezoresistor.

Other than reducing the noise, the other way to improve the sensor resolution is to improve the sensitivity. As indicated by Eq. (4-1), the output voltage is proportional to excitation voltage. Under the same deformation, the larger the excitation voltage the larger the output voltage hence the higher the sensitivity. However, as the excitation voltage increases, larger current passes through the piezoresistors generating more heat which increases both the temperature and resistance of the piezoresistors, hence the Johnson noise level increases which undermines the resolution. Therefore, we conducted an experiment to study the signal-to-noise ratio under different excitation voltages of the Wheatstone bridge. A sine voltage with amplitude 40 V and frequency of 50 Hz was applied to the comb-drive actuator while the Wheatstone bridge is excited

at voltage level 1V, 2V and 3V. Figure 4.7(a) shows the measured output voltage in time domain. As can be seen intuitively, the noise didn't show much difference at each excitation voltage level but the amplitude of signal obviously increased. Frequency domain analysis was also conducted which is shown in Figure 4.7(b), it can be seen that the noise floor was almost the same for all the three excitation voltage levels while the signal at 100 Hz increased with increasing excitation voltage. The reason that the noise floor doesn't change too much is because Johnson noise only occupies a small part comparing with the amplifier noise. This would be different if the ultralow noise instrumentation amplifier is used where noise from the piezoresistor and amplifier will be comparable. In this work with AD620 used, it is reasonable to say that the sensitivity of the sensor increases with the increasing excitation voltage of the Wheatstone bridge.

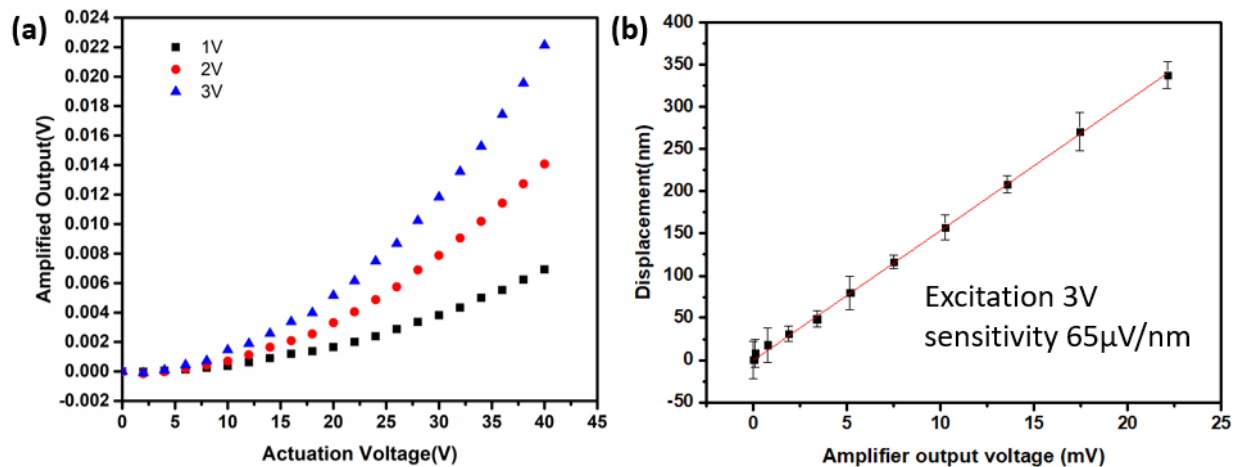


Figure 4.7. (a) The relationship between actuation voltage and amplified output voltage of wheatstone bridge with different excitation voltages. (b) Calibrated relationship between displacement and amplified output voltage when the excitation voltage is 3V.

With the above discussion, to obtain a higher resolution, a larger excitation voltage is preferred. However, there is another factor which needs to be considered, i.e. the temperature effect of a specimen. Higher excitation voltage leads to higher temperature rise in the specimen area which will change the mechanical properties of temperature sensitive material. For the current

work, we used the 3V excitation voltage which will cause a temperature rise to around 50 degree in the specimen area in vacuum based on the simulation result.

Finally, the sensor's response to a ramping input is studied as a demonstration of using the sensor in high strain rate nanomechanical tensile testing. As mentioned, the MEMS platform in last chapter is able to carry out high strain rate nanomechanical tensile testing with strain rate up to 10 s^{-1} , higher strain rate is limited due to the low bandwidth displacement sensor. Here using this piezoresistive sensor, a higher strain rate is expected. To provide the ramping displacement, the same kind of voltage profile as in last chapter $V(t) = 40t^{0.5}$ was applied to the actuator. Output voltage was amplified through the AD620 with an anti-aliasing low pass filter (cutoff frequency = 15000 Hz) and then sampled by DAQ NI USB 6211 (sample frequency 200 kHz). Figure 4.8 shows measured displacement when $t = 0.1 \text{ ms}$. As can be seen, the output voltage increased linearly with time during the ramping period. Different from the capacitive measurement, no lag phenomenon was observed as in this case which again proves this piezoresistive sensor can match the high-speed sensing requirement during high strain rate nanomechanical tensile testing. The corresponding strain rate for this case is 750 s^{-1} . The measured 6σ resolution is 48 nm, the calculated 6σ resolution using Eq. (4-3), (4-4) and (4-8) is 52 nm, they are close to each other. Using an ultralow noise instrumentation amplifier AD8429, the resolution was expected to be increased to within 10 nm. Note that this resolution is for the large 750 s^{-1} strain rate, for a smaller strain rate, a lower bandwidth can be used which will further increase the resolution.

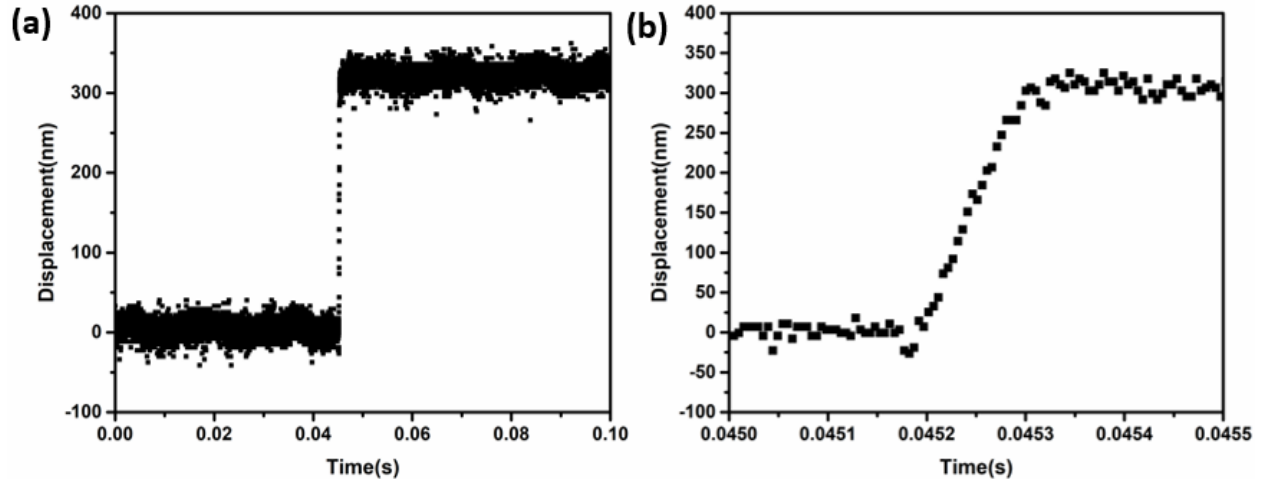


Figure 4.8. (a) Sensor output under a ramping input with 0.1 ms loading time. (b) A closer look of the loading period.

4.4. Conclusion

In this work, a piezoresistive displacement sensor is introduced. The sensor is in a Wheatstone bridge configuration. Static calibration of the sensor was conducted first where an on-chip comb-drive electrostatic actuator is used to deform the sensor. It was found that there is a linear relationship between sensor's displacement and output voltage of the Wheatstone bridge. The linear relationship was explained with previous researcher's simulation results. Dynamic response of the sensor was also characterized, the result of which shows the sensor has a fast response speed and can be used in nanomechanical tensile experiments such as high strain rate testing. Resolution of the sensor was discussed from the sensitivity and noise aspects. It was found that currently the sensor includes a large amount of extrinsic noise which limits the resolution. The source of the extrinsic noise is under investigation. Two methods currently can be used to mitigate the noise issue, by increasing the excitation voltage which increase the sensitivity of the sensor and adding a filter to remove certain noise. It was demonstrated that for a high strain rate testing

with strain rate 75 s^{-1} , a low pass filter with cut off frequency 15000 Hz can be used which lead to a resolution of 53 nm .

REFERENCES

1. Liu, C.-H.; Chang, H.-D.; Li, K.-H.; Lin, C.-H.; Hsu, C.-J.; Lin, T.-Y.; Chou, H.-H.; Huang, H.-C.; Liao, H.-Y. In *Adaptable and integrated packaging platform for MEMS-based combo sensors utilizing innovative wafer-level packaging technologies*, Electronic Components and Technology Conference (ECTC), 2013 IEEE 63rd, 2013; IEEE: pp 1675-1681.
2. Kovacs, G. T.; Maluf, N. I.; Petersen, K. E. *Proceedings of the IEEE* **1998**, 86, (8), 1536-1551.
3. Kang, C. K.; Lee, S. M.; Jung, I. D.; Jung, P. G.; Hwang, S. J.; Ko, J. S. *Journal of Micromechanics and Microengineering*. **2008**, 18, (7), 075007.
4. Lucas, S.; Kis-Sion, K.; Pinel, J.; Bonnaud, O. *Journal of Micromechanics and Microengineering*. **1997**, 7, (3), 159.
5. McAlpine, M. C.; Friedman, R. S.; Jin, S.; Lin, K.-h.; Wang, W. U.; Lieber, C. M. *Nano Letters* **2003**, 3, (11), 1531-1535.
6. Fan, Z.; Ho, J. C.; Takahashi, T.; Yerushalmi, R.; Takei, K.; Ford, A. C.; Chueh, Y. L.; Javey, A. *Advanced Materials* **2009**, 21, (37), 3730-3743.
7. Xu, F.; Lu, W.; Zhu, Y. *Acs Nano*. **2010**, 5, (1), 672-678.
8. Yao, S.; Zhu, Y. *Advanced materials*. **2015**, 27, (9), 1480-1511.
9. Wang, Z. L.; Song, J. *Science* **2006**, 312, (5771), 242-246.
10. Chan, C. K.; Peng, H.; Liu, G.; McIlwrath, K.; Zhang, X. F.; Huggins, R. A.; Cui, Y., High-performance lithium battery anodes using silicon nanowires. In *Materials for Sustainable Energy: A Collection of Peer-Reviewed Research and Review Articles from Nature Publishing Group*, World Scientific: 2011; pp 187-191.
11. Feng, X.; He, R.; Yang, P.; Roukes, M. *Nano Letters*. **2007**, 7, (7), 1953-1959.
12. Loh, O. Y.; Espinosa, H. D. *Nature nanotechnology*. **2012**, 7, (5), 283.
13. Poncharal, P.; Wang, Z.; Ugarte, D.; De Heer, W. A. *science*. **1999**, 283, (5407), 1513-1516.
14. Treacy, M. J.; Ebbesen, T.; Gibson, J. *Nature*. **1996**, 381, (6584), 678.
15. Qin, Q.; Xu, F.; Cao, Y.; Ro, P. I.; Zhu, Y. *Small*. **2012**, 8, (16), 2571-2576.

16. Chen, C.; Shi, Y.; Zhang, Y. S.; Zhu, J.; Yan, Y. *Physical review letters*. **2006**, 96, (7), 075505.
17. Wu, B.; Heidelberg, A.; Boland, J. J. *Nature materials* **2005**, 4, (7), 525.
18. Salvétat, J.-P.; Briggs, G. A. D.; Bonard, J.-M.; Bacsá, R. R.; Kulik, A. J.; Stöckli, T.; Burnham, N. A.; Forró, L. *Physical review letters*. **1999**, 82, (5), 944.
19. Stan, G.; Ciobanu, C.; Parthangal, P. M.; Cook, R. F. J. N. L. **2007**, 7, (12), 3691-3697.
20. Zheng, M.; Ke, C.; Bae, I.-T.; Park, C.; Smith, M. W.; Jordan, K. *Nanotechnology*. **2012**, 23, (9), 095703.
21. Zhu, Y.; Qin, Q.; Xu, F.; Fan, F.; Ding, Y.; Zhang, T.; Wiley, B. J.; Wang, Z. L. *J Physical review B* **2012**, 85, (4), 045443.
22. Richter, G.; Hillerich, K.; Gianola, D. S.; Monig, R.; Kraft, O.; Volkert, C. A. *Nano Letters*. **2009**, 9, (8), 3048-3052.
23. Xu, F.; Qin, Q.; Mishra, A.; Gu, Y.; Zhu, Y. *Nano Research*. **2010**, 3, (4), 271-280.
24. He, M.-R.; Shi, Y.; Zhou, W.; Chen, J.; Yan, Y.; Zhu, J. *Applied Physics Letters* **2009**, 95, (9), 091912.
25. Lin, C. H.; Ni, H.; Wang, X.; Chang, M.; Chao, Y. J.; Deka, J. R.; Li, X. *Small* **2010**, 6, (8), 927-931.
26. Li, X.; Gao, H.; Murphy, C. J.; Caswell, K. *Nano letters*. **2003**, 3, (11), 1495-1498.
27. Feng, G.; Nix, W. D.; Yoon, Y.; Lee, C. J. *Journal of Applied Physics*. **2006**, 99, (7), 074304.
28. Corigliano, A.; Domenella, L.; Espinosa, H. D.; Zhu, Y. *Sensor Letters*. **2007**, 5, (3-4), 592-607.
29. Guan, C.; Zhu, Y. *Journal of Micromechanics and Microengineering*. **2010**, 20, (8), 085014.
30. Abbas, K.; Alaie, S.; Leseman, Z. C. *Journal of Micromechanics and Microengineering* **2012**, 22, (12), 125027.
31. Zhu, Y.; Corigliano, A.; Espinosa, H. D. *Journal of micromechanics and microengineering* **2006**, 16, (2), 242.
32. Qin, Q.; Zhu, Y. J. A. P. L. **2013**, 102, (1), 013101.

33. de Boer, M. P.; Luck, D. L.; Ashurst, W. R.; Maboudian, R.; Corwin, A. D.; Walraven, J. A.; Redmond, J. M. *Journal of Microelectromechanical Systems*. **2004**, 13, (1), 63-74.
34. Naraghi, M.; Chasiotis, I.; Kahn, H.; Wen, Y.; Dzenis, Y. *J. R. o. s. i.* **2007**, 78, (8), 085108.
35. Haque, M.; Saif, M. *Proceedings of the National Academy of Sciences* **2004**, 101, (17), 6335-6340.
36. Han, J. H.; Saif, M. T. A. *Review of Scientific Instruments* **2006**, 77, (4), 045102.
37. Jin, W.; Mote Jr, C. *Sensors and Actuators A: Physical*. **1998**, 65, (2-3), 109-115.
38. Kang, W.; Han, J. H.; Saif, M. T. A. *Journal of Microelectromechanical Systems* **2010**, 19, (6), 1322-1330.
39. Zhu, Y.; Moldovan, N.; Espinosa, H. D. *J. A. p. l.* **2005**, 86, (1), 013506.
40. Messenger, R. K.; Aten, Q. T.; McLain, T. W.; Howell, L. L. **2009**.
41. Samuel, B.; Haque, M.; Yi, B.; Rajagopalan, R.; Foley, H. *Nanotechnology* **2007**, 18, (11), 115704.
42. Ya'akovovitz, A.; Krylov, S.; Hanein, Y. *Sensors and Actuators A: Physical* **2010**, 162, (1), 1-7.
43. Naraghi, M.; Ozkan, T.; Chasiotis, I.; Hazra, S.; De Boer, M. J. *J. o. M.; Microengineering*. **2010**, 20, (12), 125022.
44. Zhu, Y.; Espinosa, H. D. *J. P. o. t. N. A. o. S.* **2005**, 102, (41), 14503-14508.
45. Gupta, S.; Pierron, O. N. *Journal of Microelectromechanical Systems*. **2017**, 26, (5), 1082-1092.
46. Zhang, D.; Drissen, W.; Breguet, J.-M.; Clavel, R.; Michler, J. *Journal of Micromechanics and Microengineering*. **2009**, 19, (7), 075003.
47. Kuehnel, W.; Sherman, S. *Sensors and Actuators A: Physical*. **1994**, 45, (1), 7-16.
48. Espinosa, H. D.; Zhu, Y.; Moldovan, N. *Journal of Microelectromechanical Systems* **2007**, 16, (5), 1219-1231.
49. Hosseinian, E.; Gupta, S.; Pierron, O. N.; Legros, M. *Acta Materialia*. **2018**, 143, 77-87.
50. Lantz, M. A.; Binnig, G. K.; Despont, M.; Drechsler, U. *Nanotechnology* **2005**, 16, (8), 1089.

51. Ouyang, J.; Zhu, Y. *Journal of Microelectromechanical Systems* **2012**, 21, (3), 596-604.
52. Guo, H.; Chen, K.; Oh, Y.; Wang, K.; Dejoie, C.; Syed Asif, S.; Warren, O.; Shan, Z.; Wu, J.; Minor, A. *Nano letters* **2011**, 11, (8), 3207-3213.
53. Chisholm, C.; Bei, H.; Lowry, M.; Oh, J.; Asif, S. S.; Warren, O.; Shan, Z.; George, E. P.; Minor, A. M. *Acta Materialia*. **2012**, 60, (5), 2258-2264.
54. Lu, Y.; Ganesan, Y.; Lou, J. *Experimental mechanics* **2010**, 50, (1), 47-54.
55. Zhang, D.; Breguet, J.-M.; Clavel, R.; Philippe, L.; Utke, I.; Michler, J. *Nanotechnology* **2009**, 20, (36), 365706.
56. Gupta, S.; Pierron, O. N. *Extreme Mechanics Letters*. **2016**, 8, 167-176.
57. Pantano, M. F.; Bernal, R. A.; Pagnotta, L.; Espinosa, H. D. *Meccanica*. **2015**, 50, (2), 549-560.
58. Zhu, Y.; Bazaei, A.; Moheimani, S. R.; Yuce, M. R. *Journal of Microelectromechanical Systems*. **2011**, 20, (3), 711-719.
59. Chang, T.-H.; Zhu, Y. *Applied Physics Letters*. **2013**, 103, (26), 263114.
60. Kang, W.; Saif, M. T. A. *Journal of Micromechanics and Microengineering*. **2011**, 21, (10), 105017.
61. Bernal, R. A.; Filleter, T.; Connell, J. G.; Sohn, K.; Huang, J.; Lauhon, L. J.; Espinosa, H. D. *small*. **2014**, 10, (4), 725-733.
62. Cheng, G.; Chang, T.-H.; Qin, Q.; Huang, H.; Zhu, Y. *Nano letters*. **2014**, 14, (2), 754-758.
63. Hosseinian, E.; Legros, M.; Pierron, O. N. *Nanoscale*. **2016**, 8, (17), 9234-9244.
64. Qin, Q.; Yin, S.; Cheng, G.; Li, X.; Chang, T.-H.; Richter, G.; Zhu, Y.; Gao, H. *Nature communications* **2015**, 6, 5983.
65. Naraghi, M.; Chasiotis, I.; Kahn, H.; Wen, Y.; Dzenis, Y. *Applied Physics Letters* **2007**, 91, (15), 151901.
66. Ramachandramoorthy, R.; Gao, W.; Bernal, R.; Espinosa, H. J. N. I. **2015**, 16, (1), 255-263.
67. He, R.; Yang, P. *Nature nanotechnology* **2006**, 1, (1), 42.
68. Zhu, T.; Li, J. *Progress in Materials Science*. **2010**, 55, (7), 710-757.

69. Wei, D.; Liu, Y.; Wang, Y.; Zhang, H.; Huang, L.; Yu, G. *Nano letters*. **2009**, 9, (5), 1752-1758.
70. Dai, H.; Wong, E. W.; Lieber, C. M. *Science* **1996**, 272, (5261), 523-526.
71. Ray, P. C. *Chemical reviews* **2010**, 110, (9), 5332-5365.
72. Lee, N.; Chung, D.; Han, I.; Kang, J.; Choi, Y.; Kim, H.; Park, S.; Jin, Y.; Yi, W.; Yun, M. *Diamond and related materials*. **2001**, 10, (2), 265-270.
73. Saito, Y.; Uemura, S. *Carbon* **2000**, 38, (2), 169-182.
74. Bachtold, A.; Hadley, P.; Nakanishi, T.; Dekker, C. *Science*. **2001**, 294, (5545), 1317-1320.
75. Fuhrer, M.; Nygård, J.; Shih, L.; Forero, M.; Yoon, Y.-G.; Choi, H. J.; Ihm, J.; Louie, S. G.; Zettl, A.; McEuen, P. L. *Science*. **2000**, 288, (5465), 494-497.
76. Rueckes, T.; Kim, K.; Joselevich, E.; Tseng, G. Y.; Cheung, C.-L.; Lieber, C. M. *science* **2000**, 289, (5476), 94-97.
77. Wong, S. S.; Joselevich, E.; Woolley, A. T.; Cheung, C. L.; Lieber, C. *Nature* **1998**, 394, (6688), 52.
78. Kim, P.; Lieber, C. M. *Science* **1999**, 286, (5447), 2148-2150.
79. Yao, S.; Zhu, Y. *Nanoscale* **2014**, 6, (4), 2345-2352.
80. Amjadi, M.; Pichitpajongkit, A.; Lee, S.; Ryu, S.; Park, I. *ACS nano*. **2014**, 8, (5), 5154-5163.
81. Myers, A. C.; Huang, H.; Zhu, Y. *RSC Advances* **2015**, 5, (15), 11627-11632.
82. Naraghi, M.; Chasiotis, I. *Journal of Microelectromechanical Systems* **2009**, 18, (5), 1032-1046.
83. Sun, Y.; Fry, S. N.; Potasek, D.; Bell, D. J.; Nelson, B. *Journal of microelectromechanical systems*. **2005**, 14, (1), 4-11.
84. Tsuchiya, T.; Hemmi, T.; Suzuki, J.-y.; Hirai, Y.; Tabata, O. *Applied Sciences*. **2018**, 8, (6), 880.
85. Hyde, B.; Espinosa, H. D.; Farkas, D. *Jom*. **2005**, 57, (9), 62-66.
86. Gall, K.; Diao, J.; Dunn, M. L. *Nano Letters*. **2004**, 4, (12), 2431-2436.

87. Ju, S.-P.; Lin, J.-S.; Lee, W.-J. *Nanotechnology*. **2004**, 15, (9), 1221.
88. Chen, L. Y.; He, M.-r.; Shin, J.; Richter, G.; Gianola, D. S. J. N. m. **2015**, 14, (7), 707.
89. Peng, C.; Zhong, Y.; Lu, Y.; Narayanan, S.; Zhu, T.; Lou, J. *Applied Physics Letters* **2013**, 102, (8), 083102.
90. Naraghi, M.; Kolluru, P. V.; Chasiotis, I. *Journal of the Mechanics and Physics of Solids* **2014**, 62, 257-275.
91. Yamahata, C.; Sarajlic, E.; Krijnen, G. J.; Gijs, M. A. *Journal of Microelectromechanical Systems*. **2010**, 19, (5), 1273-1275.
92. King, H.; Warnat, S.; Hubbard, T. In *Effect of image degradation on nm-scale MEMS FFT optical displacement measurements*, Electrical and Computer Engineering (CCECE), 2015 IEEE 28th Canadian Conference on, 2015; IEEE: pp 1387-1392.
93. Ellerington, N.; Bscheiden, B.; Hubbard, T.; Kujath, M. *Journal of Micromechanics and Microengineering*. **2012**, 22, (3), 035019.
94. Zhang, X.; Tang, W. C. In *Viscous air damping in laterally driven microresonators*, Micro Electro Mechanical Systems, 1994, MEMS'94, Proceedings, IEEE Workshop on, 1994; IEEE: pp 199-204.
95. Bao, M., *Analysis and design principles of MEMS devices*. Elsevier: 2005.
96. Bao, M.; Yang, H. *Sensors and Actuators A: Physical*. **2007**, 136, (1), 3-27.
97. Boyce, B. L.; Crenshaw, T. B. *Sandia National Laboratories Report, SAND-2005*, 1-16.
98. Zhu, D.; Rajan, S.; Mobasher, B.; Peled, A.; Mignolet, M. *Experimental Mechanics* **2011**, 51, (8), 1347-1363.
99. de Andrade Silva, F.; Zhu, D.; Mobasher, B.; Soranakom, C.; Toledo Filho, R. D. *Materials Science and Engineering: A*. **2010**, 527, (3), 544-552.
100. Veijola, T.; Kuisma, H.; Lahdenperä, J.; Ryhänen, T. *Sensors and Actuators A: Physical* **1995**, 48, (3), 239-248.
101. Sedlmayr, A.; Bitzek, E.; Gianola, D. S.; Richter, G.; Mönig, R.; Kraft, O. *Acta Materialia* **2012**, 60, (9), 3985-3993.
102. Park, H. S.; Zimmerman, J. A. *Physical Review B*. **2005**, 72, (5), 054106.
103. Tao, W.; Cao, P.; Park, H. S. *Nano letters* **2018**, 18, (2), 1296-1304.

104. Guliyev, E.; Volland, B.; Sarov, Y.; Ivanov, T.; Klukowski, M.; Manske, E.; Rangelow, I. *Measurement Science Technology*. **2012**, 23, (7), 074012.
105. Chui, B. W.; Stowe, T. D.; Ju, Y. S.; Goodson, K. E.; Kenny, T. W.; Mamin, H. J.; Terris, B. D.; Ried, R. P.; Rugar, D. *Journal of Microelectromechanical Systems* **1998**, 7, (1), 69-78.
106. Mosser, V.; Suski, J.; Goss, J.; Obermeier, E. *Sensors and Actuators A: Physical* **1991**, 28, (2), 113-132.
107. Zhu, S.-E.; Krishna Ghatkesar, M.; Zhang, C.; Janssen, G. *Applied Physics Letters* **2013**, 102, (16), 161904.
108. Gray, P. R.; Hurst, P.; Meyer, R. G.; Lewis, S., *Analysis and design of analog integrated circuits*. Wiley: 2001.
109. Hooge, F. *IEEE Transactions on Electron Devices* **1994**, 41, (11), 1926-1935.
110. Van der Ziel, A. *Proceedings of the IEEE* **1988**, 76, (3), 233-258.
111. Vandamme, L. K. *IEEE Transactions on Electron Devices*. **1989**, 36, (5), 987-992.
112. Yu, X.; Thaysen, J.; Hansen, O.; Boisen, A. *Journal of Applied Physics* **2002**, 92, (10), 6296-6301.
113. Harkey, J.; Kenny, T. W. *Journal of microelectromechanical systems*. **2000**, 9, (2), 226-235.
114. Mallon Jr, J.; Rastegar, A.; Barlian, A.; Meyer, M.; Fung, T.; Pruitt, B. *Applied Physics Letters* **2008**, 92, (3), 033508.